Charles University

Faculty of Science

Study program: Physical chemistry

Mgr. Yuyan Zhang

Metal nanoparticles in zeolites

Dissertation

Supervisor: Prof. Ing. Jiří Čejka, DrSc.

Prague, May 2021

Univerzita Karlova

Přírodovědecká fakulta

Studijní program: Fyzikální chemie

Mgr. Yuyan Zhang

Kovové nanočástice v zeolitech

Disertační práce

Školitel: Prof. Ing. Jiří Čejka, DrSc.

Praha, Květen 2021

Prohlášení

Disertační práce byla vypracována v oddělení Syntézy a katalýzy Ústavu fyzikální chemie J. Heyrovského AV ČR v období 15. 09. 2017 – 31. 12. 2018 a na Katedře fyzikální a makromolekulární chemie Přírodovědecké fakulty Univerzity Karlovy od 1.1.2019.

Prohlašuji, že jsem závěrečnou práci zpracoval samostatně a že jsem uvedl všechny použité informační zdroje a literaturu. Tato práce ani její podstatná část nebyla předložena k získání jiného nebo stejného akademického titulu.

V Praze, 31.05.2021

……
Podpis

Acknowledgement

I would like to express sincere thanks to my supervisor, prof. Jiří Čejka, for giving me the opportunity to become a member of his research group and to complete my PhD thesis. I am deeply grateful for his advices and support given to me.

I would like to express my appreciation to my advisor Dr. Martin Kubů for his advice, discussions, and physisorption measurement. I would like to thank my advisor Dr. Mariya Shamzhy for her guidance and FTIR measurement. Many thanks to Dr. Michal Mazur and Ang Li help me with STEM measurement. I would like to thank Dr. Valeryia Kasneryk and Qiudi Yue for SEM measurement and Dr. Zdeněk Tošner for solid-state NMR measurement. I would like to thank all my colleagues in Charles University: Dr. Maksym Opanasenko, Dr. Jan Přech, Dr. Roman Barakov, Dr. Kinga Gołąbek, Milan Eliáš, Ondrej Vesely, Jin Zhang, and Sarra Abdi.

I would like to extend my thanks to prof. Roman Bulanek and Sajad Mehran in Faculty of Chemical Technology, University of Pardubice, for the catalytic measurement and to prof. Milan Hronec and Dr. Katarína Fulajtárová in Department of Inorganic Technolgy, Slovak University of Technology, for helping me with the catalytic testing.

I would like to thank my husband Jianwei Li for his support during all my Ph.D. studies.

I would like to thank my family and friends for their support during all my Ph.D. studies.

Contents

List of abbreviations

^{1}H NMR	- Proton nuclear magnetic resonance
2D zeolite	- Two-dimensional zeolite
3D zeolite	- Three-dimensional zeolite
ADOR	- Assembly, disassembly, organization, reassembly
BET	- Surface area according to Brunauer–Emmett–Teller isotherm
d_{TEM}	- Surface-weighted mean nanoparticle diameters
D4R	- Double four ring
GC	- Gas chromatography
GC-MS	- Gas chromatograph coupled with a mass spectrometer
IZA	- International Zeolite Association
MAS NMR	- Magic angle spinning nuclear magnetic resonance
OA	- Octylamine
Pt-DMF	- Pt nanoparticles in DMF solution
Pt@MFI_ImILs	- Pt nanoparticles encapsulated into **MFI** assisted with ImILs
Pd@MFI_ImILs	- Pd nanoparticles encapsulated into **MFI** assisted with ImILs
Pt@MFI	- Pt nanoparticles supported on **MFI** zeolite
Pd@MFI	- Pt nanoparticles supported on **MFI** zeolite
Pt@MFI_Imp	- Pt nanoparticles impregnated on **MFI** zeolite
Pd@MFI_Imp	- Pd nanoparticles impregnated on **MFI** zeolite
Pt@MCM-22	- Pt nanoparticles encapsulated into MCM-22 zeolite
Pd@MCM-22	- Pd nanoparticles encapsulated into MCM-22 zeolite
Pd/C	- Commercial Pd/C catalyst
Pt@IPC-2	- Pt nanoparticles encapsulated into IPC-2 zeolite
Pt@IPC-4	- Pt nanoparticles encapsulated into IPC-4 zeolite
Pd@IPC-2	- Pd nanoparticles encapsulated into IPC-2 zeolite

Pd@IPC-4	- Pd nanoparticles encapsulated into IPC-4 zeolite
SDA	- Structure directing agent (= organic template)
SEM	- Scanning electron microscopy
STEM	- Transmission electron microscopy
S4R	- Single four ring
SAC	- Steam-assisted crystallization
TEM	- Transmission electron microscopy
TEOS	- Tetraethyl orthosilicate
TPAOH	- Tetrapropyl ammonium hydroxide
TOF	- Turnover frequency
TON	- Turnover number
TOS	- Time-on-stream
V_{meso}	- Mesopore volume
V_{mic}	- Micropore volume
V_{tot}	- Total adsorbed volume
XRD	- X-ray diffraction

List of publications

The dissertation thesis is based on following publications:

1. **Yuyan Zhang**, Ang Li, Mehran Sajad, Katarína Fulajtárová, Michal Mazur, Martin Kubů, Mariya Shamzhy, Milan Hronec, Roman Bulánek, and Jiří Čejka *. Imidazolium-type ionic liquid-assisted formation of the MFI zeolite loaded with metal nanoparticles for hydrogenation reactions*, Chem. Eng. J.*, **2021**, 412, 128599. (**IF** = 10.652)

2. **Yuyan Zhang**, Martin Kubů *, Michal Mazur, Jiří Čejka. Synthesis of Pt-MWW with Controllable Nanoparticle Size, *Catal. Today*, **2019**, 324,135. (**IF** = 5.825)

3. **Yuyan Zhang**, Katarína Fulajtárová, Martin Kubů, Michal Mazur *, Mariya Shamzhy, Milan Hronec, and Jiří Čejka *. Controlling dispersion and accessibility of Pd nanoparticles via 2D-to-3D zeolite transformation for shape-selective catalysis: Pd@MWW case, *Materials Today Nano*, **2019**, 8, 100056. (Forecast **IF** = 7.9)

4. **Yuyan Zhang**, Martin Kubů, Michal Mazur, Jiří Čejka *. Encapsulation of Pt nanoparticles into IPC-2 and IPC-4 zeolites using the ADOR approach, *Microporous Mesoporous Mater*., **2019**, 279, 364. (**IF** = 4.551)

Further publications:

1. **Yuyan Zhang**, Katarína Fulajtárová, Martin Kubů, Michal Mazur *, Milan Hronec, Jiří Čejka. Electronic/steric effects in hydrogenation of nitroarenes over the heterogeneous Pd@BEA and Pd@MWW catalysts, *Catal. Today*, **2020**, 345, 39. (IF=5.825)

Abstract

Zeolites with encapsulated metal nanoparticles have attracted a wide attention in heterogeneous catalysis due to their high catalytic activity, selectivity, and stability. The PhD thesis was focused on design and synthesis of metal@zeolite catalysts with small and uniformly distributed metal nanoparticles. The main interests were encapsulation of metal nanoparticles into zeolites by co-crystallization strategy and 2-dimensional to 3-dimensional zeolite transformation approach. The PhD work was performed at the Department of Synthesis and Catalysis at J. Heyrovský Institute of Physical Chemistry and Department of Physical and Macromolecular Chemistry, Faculty of Science at Charles University under the supervision of prof. Jiří Čejka.

Zeolites are inorganic crystalline aluminosilicates with microporous framework structures. The micropores of zeolites provide the ideal microenvironment to accommodate metal nanoparticles. During metal nanoparticles formation in zeolite micropores, they can be limited by a rigid framework, preventing the aggregation and leaching of metal during the reaction process. Furthermore, the diameters of zeolite micropores are usually in the range of 0.3-1.5 nm, which can be used to discriminate molecules depending on their size and shape, thus endowing the metal@zeolite catalysts with shape-selectivity. In addition, encapsulation of metal nanoparticles into zeolites can adjust the distribution of metal and acid sites, creating high-efficiency bi-functional catalysts.

Pt and Pd nanoparticles encapsulated in **MFI** zeolite were prepared by co-crystallization strategy with the assistance of imidazolium-type ionic liquid (ImILs). The imidazolium groups interact with metal precursors ($PtCl_4^{2-}$, $PdCl_4^{2-}$ *etc.*), while the alkoxysilane groups take part in zeolite crystallization. The resulting Pt@MFI_ImILs and Pd@MFI_ImIls had average diameters of Pt or Pd nanoparticles approximately 1.0 nm and 1.7 nm, respectively. The Pt@MFI_ImILs exhibited excellent shape-selectivity in hydrogenation of different size nitroarenes. The conversion of the small 4-nitrotoluene was >99%, while the bulky 1,3-dimethyl-5-nitrobenzene exhibited only 5.8% conversion. Owing to the small size of Pd nanoparticles, the Pd@MFI_ImILs showed a higher reaction rate (25 mmol/s/g_{Me}) than the impregnated Pd@MFI_Imp catalyst (9 mmol/s/g_{Me}) in propene hydrogenation.

Encapsulation of metal nanoparticles into zeolites *via* 2-dimensional to 3-dimensional zeolite transformation approach was also investigated. Pt@MCM-22 catalysts with tunable sizes of Pt nanoparticles were synthesized using surfactants with different alkyl chain lengths in swelling procedure of layered MCM-22P. The average diameters of Pt nanoparticles increased from 0.85 nm, 1.00 nm, 1.55nm to 2.04 nm with the prolongation of hydrocarbon chain of surfactants. Subsequently, Pd nanoparticles were encapsulated into MCM-22 zeolite by adding of $Pd(en)_2(Ac)_2$ during the swelling of MCM-22P layered zeolite. After calcination and reduction, the Pd@MCM-22 catalyst showed a uniform distribution of Pd nanoparticles with average diameter at 1.8 nm. Lastly, this 2-dimensional to 3-dimensional zeolite transformation strategy was expanded to IPC-1P and combined with the ADOR (Assembly, Disassembly, Organization, and Reassembly) approach. Metal@IPC-2 and metal@IPC-4 (metal = Pt or Pd) with uniform distribution of metal nanoparticles were prepared.

Abstrakt

Zeolity se zapouzdřenými kovovými nanočásticemi vzbudily v heterogenní katalýze velkou pozornost díky své vysoké katalytické aktivitě, selektivitě a stabilitě. Tato diplomová práce byla zaměřena na syntézu zeolitových katalyzátorů s malými a rovnoměrně distribuovanými kovovými nanočásticemi. Hlavními cíly bylo zapouzdření kovových nanočástic do zeolitu pomocí kokrystalizační strategie a 2D-3D transformce zeolitu. Doktorská práce byla provedena na oddělení syntézy a katalýzy J. Heyrovského Ústav fyzikální chemie a Katedře fyzikální a makromolekulární chemie na Přírodovědecké fakultě Univerzity Karlovy pod dohledem Prof. Jiřího Čejky.

Zeolity jsou anorganické krystalické hlinitokřemičitany s mikroporézní strukturou. Mikropóry zeolitů poskytují ideální prostředí pro umístění kovových nanočástic. Kovových nanočástice vznikající v mikropórech zeolitu mohou být omezeny jeho krystalickou mříží, zabraňující agregaci a vyplavování kovu během reakčního procesu. Průměry mikropórů zeolitu se obvykle pohybují v rozmezí 0,3-1,5 nm, což může sloužit k oddělení molekul v závislosti na jejich velikosti a tvaru, čímž se katalyzátory zeolite s kovovými nanočásticemi obohatí o tvarovou selektivitu. Zapouzdření kovových nanočástic do zeolitů může navíc ovlivnit distribuci kovových a kyselých center a vytvořit tak bifunkční katalyzátory s vysokou účinností.

Nanočástice Pt a Pd zapouzdřené v zeolitu MFI byly připraveny kokrystalizační strategií s pomocí iontové kapaliny imidazolového typu (ImIL). Skupiny imidazolia interagují s prekurzory kovů ($PtCl_4^{2-}$, $PdCl_4^{2-}$ atd.), zatímco alkoxysilanové skupiny se podílejí na krystalizaci zeolitu. Výsledné Pt@MFI_ImILs měly průměrné velikosti kovových nanočástic přibližně 1,0 nm a 1,7 nm. Pt@MFI_ImILs vykazoval vynikající tvarovou selektivitu při hydrogenaci nitroarénů různých velikostí. Konverze méně objemného 4-nitrotoluenu byla >99%, zatímco objemný 1,3-dimethyl-5-nitrobenzen vykazoval pouze konverzi 5,8%. Vzhledem k malé velikosti Pd nanočástic vykazovaly Pd@MFI_ImILs vyšší rychlost reakce (25 mmol/s/gMe) než impregnovaný katalyzátor Pd@MFI_Imp (9 mmol/s/gMe) při hydrogenaci propenu.

Rovněž bylo zkoumáno zapouzdření kovových nanočástic do zeolitů pomocí 2D-3D transformace zeolitu. Katalyzátory Pt@MCM-22 s laditelnou velikostí Pt nanočástic byly

syntetizovány za použití povrchově aktivních látek s různými délkami alkylových řetězců v procesu interkalace vrstevnatého MCM-22P. Průměrné velikosti Pt nanočástic vzrostly z 0,85 nm, 1,00 nm, 1,55 nm až na 2,04 nm v závislosti na délce uhlovodíkového řetězce povrchově aktivních látek. Následně jsme zapouzdřili Pd nanočástice do MCM-22 zeolitu přidáním Pd(en)2(Ac)2 během interkalace vrstevnatého zeolitu MCM-22P. Po kalcinaci a redukci vykázal katalyzátor Pd@MCM-22 rovnoměrnou distribuci Pd nanočástic o průměrném průměru 1,8 nm. Nakonec jsme tuto metodu 2D-3D transformace zeolitu rozšířili na vrstevnatý materiál IPC-1P v kombinaci s metodou ADOR (Assembly, rozložení Organizace, a Reassembly). Byly připraveny zeolity IPC-2 a IPC-4 se zapouzdřenými nanočásticemi kovu (Pt nebo Pd) s rovnoměrnou distribucí kovových nanočástic.

1 Aim of study

This thesis was focused on design and encapsulation of metal nanoparticles into zeolites to stabilize metal nanoparticles and to investigate them as catalysts in hydrogenation reactions.

The main goals are summarized as follows:

1) Encapsulation of metal nanoparticles into **MFI** zeolite by means of direct hydrothermal synthesis with the assistant of imidazolium-type ionic liquid.

To stabilize metal precursors during **MFI** zeolite crystallization process;

To design metal@MFI (metal = Pt, Pd, Au) catalysts;

2) Encapsulation of metal nanoparticles into zeolites by means of 2-dimensional to 3-dimensional zeolites transformation approach.

To design Pt@MCM-22 with different diameters of Pt nanoparticles;

To encapsulate Pd nanoparticles into MCM-22 zeolite;

To design the synthesis of metal@IPC-4 and metal@IPC-2 (metal = Pt, Pd) combined with ADOR approach;

3) To characterize prepared metal@zeolite materials by XRD, nitrogen physisorption, SEM, TEM, STEM, ICP-OES elemental analysis and FTIR measurement by CO adsorption.

4) To investigate the catalytic performance of metal@zeolite in hydrogenation of nitroarenes and propene.

2 Introduction

2.1 Zeolites

Zeolites are crystalline aluminosilicates with three-dimensional frameworks consisting of channels and cavities with molecular dimension (0.3-1.5 nm) and providing large surface areas and high porosity [1-3]. Conventional zeolites are built from silicate frameworks, in which replacement of Si for Al (or other tri-valent metals) induces a negative charge of the framework, with cations (Na^+ or other alkaline or alkaline earth metals) in the pore systems to balance the negative charge [4,5]. Structurally, the zeolite frameworks are composed of TO_4 tetrahedra. T represents the tetrahedrally coordinated atoms (Si, Al or other heteroatoms, such B, Ge, Ti, Ga, *etc.*), while O stands for the oxygen ions. The different ways of TO_4 tetrahedra connections result in various zeolite microporous structures. The pore size of zeolite is principally determined by the number of T-atoms on the ring which forms the window [1-5]. Commonly, zeolites with 8-rings possessing pore dimensions up to 0.4 nm are named as small-pore zeolites (*e.g.,* **LTA**). The pore dimensions up to 0.55 nm in 10-rings zeolites are referred to medium-pore zeolites (*e.g.,* **MFI**, **MWW**). 12-rings zeolites with pore size up to 0.75 nm are named as large-pore zeolites (*e.g.,* **BEA**, **FAU**). Zeolites with more than 12-rings are called as extra-large-pore zeolites (*e.g.,* **UTL**). In addition, zeolites with non-intersecting channels have a one-dimensional channel system (*e.g.,* **MTW**, **TON**). Zeolites with two-dimensional and three-dimensional channel systems have intersecting channels in two or three dimensions (*e.g.,* **MWW** has two-dimensional systems and **MFI** have three-dimensional systems) [6,7]. All existing zeolite structures have a unique three capital letters code assigned by the Structure Commission of the International Zeolite Association (IZA). Up to 2021, totally 253 zeolite framework types have been collected.

The pore sizes of zeolites are in the range of 0.3-1.5 nm, so only molecules with kinetic diameters not exceeding the (uniform) pore size of a zeolite can access the pores and channels. Due to such ability, zeolites are important materials called molecular sieves allowing molecules with different sizes to be separated. This is so called shape-selectivity, which has been introduced in the 1950s [8]. The shape selectivity in zeolites depends on the diffusion limitation or the size of transition states [9,10]. Three types of shape selectivity have

been described (Figure 2.1) [11]. *Reactant shape selectivity* occurs when bulky molecules are prevented to diffuse into the channels of a zeolite. Only molecules with smaller sizes than the pore openings of a zeolite are able to reach the active sites [11]. *Restricted transition state selectivity* is observed when chemical reactions involve transition states, which are too bulky to be formed in the pore system of a zeolite. Products are generated only from the reactions with small size transition states, which can fit in the micropores of zeolites. In this case, reactants and potential products can diffuse in or out of a zeolite [11]. *Product shape selectivity* is among all the formed products, only those with proper size can diffuse from the interior pore system of a zeolite. Some zeolites possess cavities inside the crystals which have enough space to form small and bulky products. However, the bulky products are unable to leave the cages due to their small apertures [11].

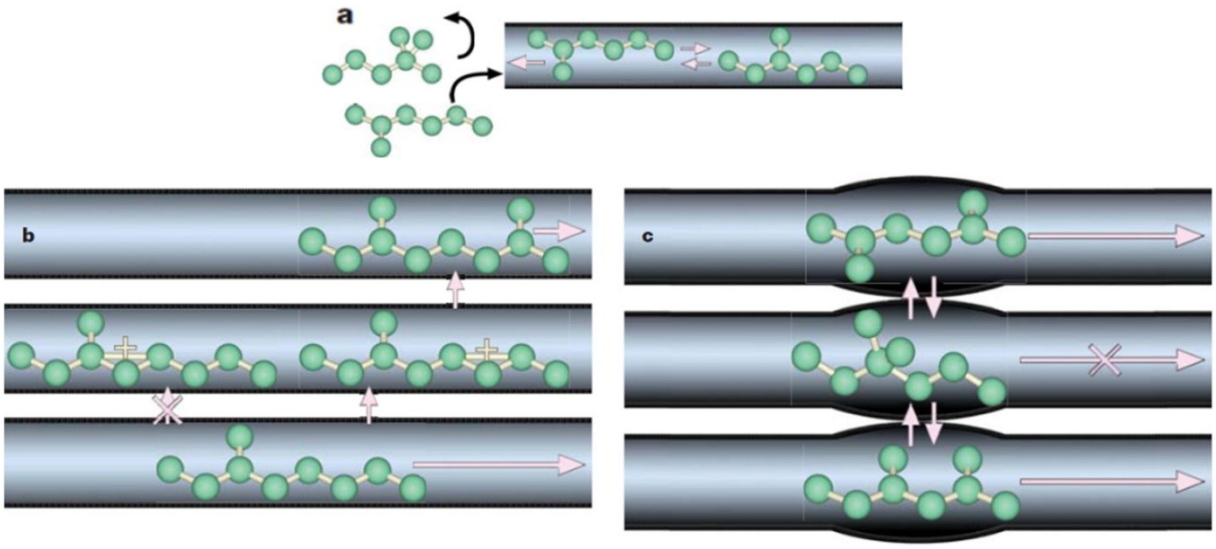

Figure 2.1 Three types of shape selectivity: *Reactant shape selectivity* (a), *Restricted transition state selectivity* (b) and *Product shape selectivity* (c) [10].

Zeolites are usually synthesized under hydrothermal conditions, from framework-building sources (*e.g.,* Si, Al, B, Ga, Ti, *etc.*) dissolved into an aqueous solution of a structure directing agent (SDA) and alkali hydroxide [12,13]. The hydrothermal synthesis of zeolites is carried out in an autoclave at elevated temperature (50-200 °C) and autogenous pressure [1]. Zeolite crystallization from appropriate synthesis gels or from clear solutions occurs through several sequential steps: (1) nucleation of discrete particles of a new phase, and (2) growth of zeolite crystals [6,14,15]. Zeolite crystallization depends on various parameters such as: solubility of silicon or framework-building sources, the structure of SDA, the pH of the synthesis gel,

ageing time of the synthesis gel, the agitation, temperature, and time of the synthesis.

However, some zeolites form two-dimensional (2D) layered zeolites, showing sheet-like morphology of zeolite crystals with the thickness of only a few unit cells [7,16,17]. Thus, 2D layered zeolites are propagated only in two dimensions, which combine the important features of 3D zeolites and the advantages of lamellas (overcoming the diffusion limitation) [18-20]. Moreover, 2D zeolites have more possibilities to be modified by post-synthetic strategies than 3D zeolites due to the flexible structure (hydrogen bonds - instead of covalent interlayer bonds). A zeolite precursor for a given framework can be used to prepare other new structures [7,16,18-20]. So far, 2D zeolites have been utilized to synthesize many new materials through stabilization, detemplation, and delamination methods [21-23]. To date, over 20 different 2D zeolites have been discovered [7]. Many of them are prepared by direct hydrothermal synthesis, but some of 2D zeolites can also be obtained by post-synthesis modification [16].

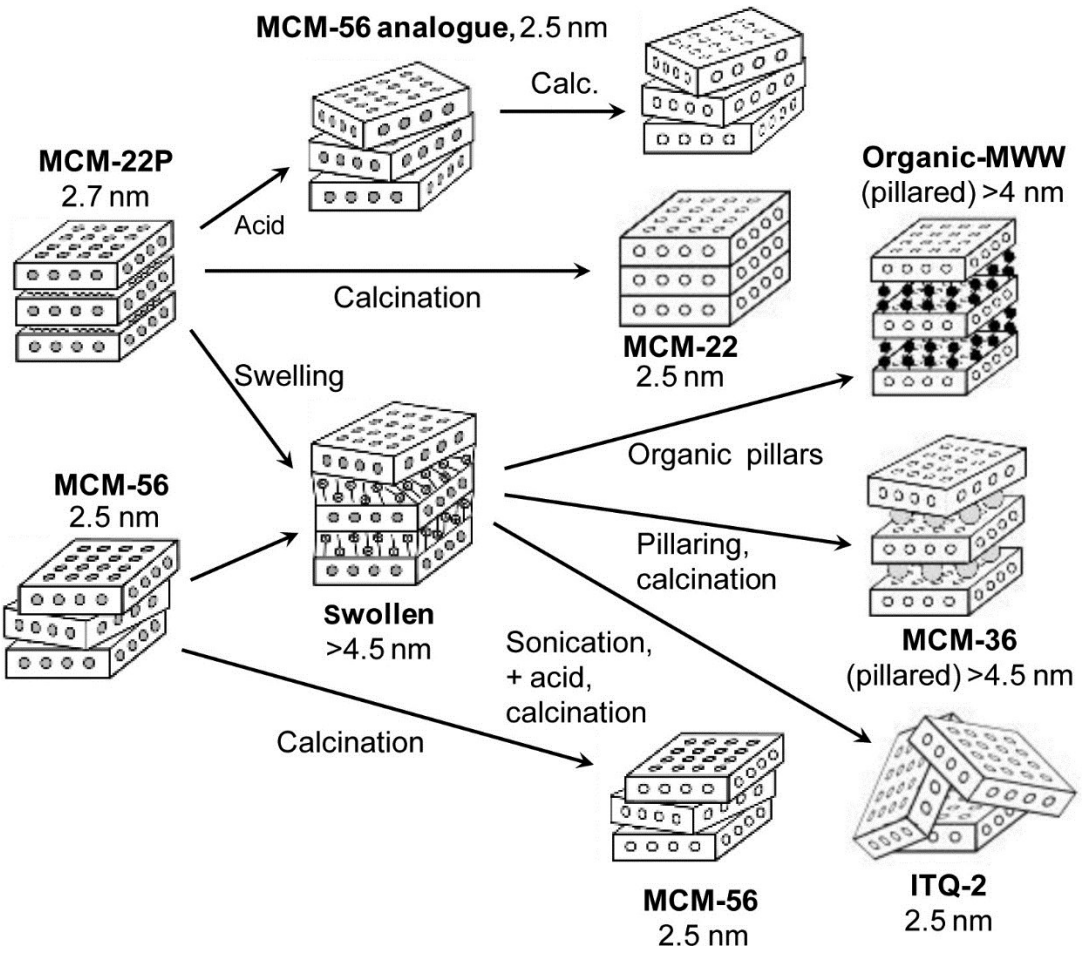

Figure 2.2 The transformations of MCM-22P and MCM-56 with interlayer d_{001} spacing distances from XRD [24].

The first recognized 2D layered zeolite was MCM-22P with **MWW** topology, which can be prepared by direct hydrothermal synthesis using hexamethyleneimine as SDA (Figure 2.2). Via condensation by calcination, MCM-22P forms 3D MCM-22 zeolite [7,25]. Moreover, the standard 3D **MWW** zeolite can be also prepared by direct hydrothermal synthesis (MCM-49) [26]. MCM-22P consists of nanosheets having thickness of 2.5 nm stacked vertically. The layers interact through hydrogen bonds between the silanol groups instead of covalent bonds. The hexamethylenimine template molecules are inserted between the layers [25]. This layered zeolite structure provides the possibility to manipulate the layers to different materials before calcination. Figure 2.2 summarizes different forms of zeolite structures in the **MWW** family [24]. MCM-56 analogue was synthesized by the treatment of MCM-22P with acid to remove the template molecules from the interlayer space [27]. Moreover, the interlayer distance of MCM-22P can be expanded by swelling with cationic surfactant, which the organic chains are intercalated between the layers and keep the layers separated [24]. However, the organic species are easily removed by calcination and the layers can condense together. In order to achieve permanent separation of the layers, the swollen MCM-22P is subsequently pillared by the inorganic pillars from amorphous silica, which derived MCM-36 zeolitic sample [28]. The prepared materials with inorganic pillars show high thermal resistance up to 500 °C [29]. In some cases, the swollen precursors MCM-22P can be pillared by organic pillars, which combine the advantages of inorganic zeolitic layers and organic pillars (*e.g.,* functionalization) [27]. In addition, the swollen MCM-22P precursors can be delaminated to ITQ-2 and colloidal suspension [30]. The main purpose of post-synthesis modifications is to produce zeolitic materials, which can shorten the diffusion path length compared with the standard 3D zeolites [7]. Layered MCM-22P has produced more than 10 different structures generating a family of zeolitic architectures (Figure 2.2) [24].

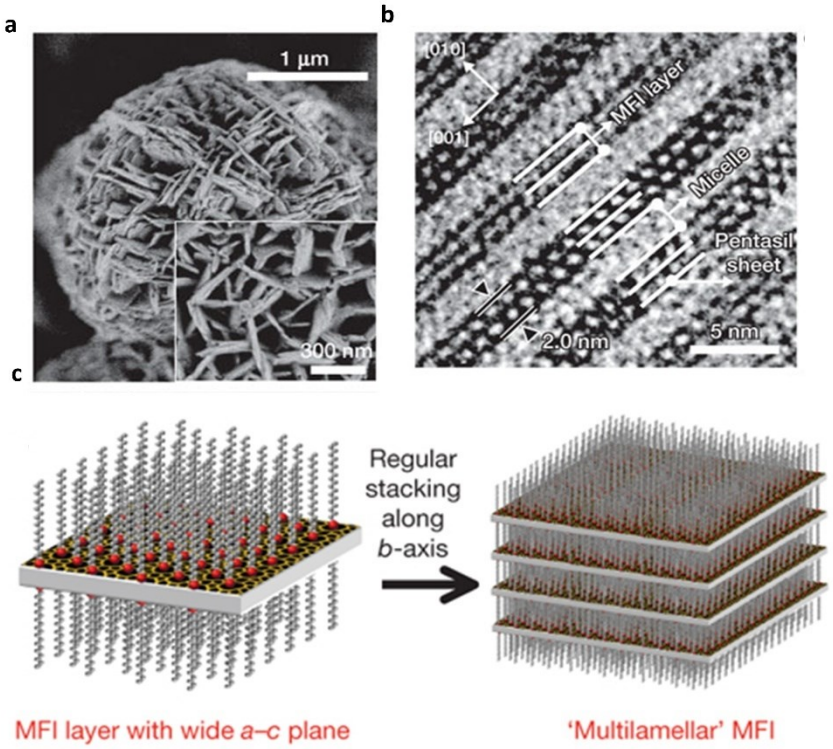

Figure 2.3 SEM image of nanosheets **MFI** with a plate-like morphology that is composed of three dimensionally intergrown nanosheets (a), TEM image of nanosheets **MFI** on the wide plane of the plate ([010] incidence of **MFI**) (b), many **MFI** nanosheets form multilamellar stacking along the b-axis (c) [31].

Ryoo and co-workers synthesized lamellar forms of zeolites **MFI** and **MTW** by surfactant-assisted synthesis strategy [31-34]. The special organic structure directing agent (SDA) has two parts: a hydrophilic headgroup and a hydrophobic tail [35]. The fundamental idea is that the head group could act as zeolite synthesis template and the tail part does not allow zeolite growth along the 3rd direction, which potentially leads to 2D zeolites. In their original work, a di-quaternary ammonium surfactant $C_{22}H_{45}–N^{+}(–CH_3)_2–C_6H_{12}–N^{+}(–CH_3)_2–C_6H_{13}$ (denoted as $C_{22–6–6}$) with a long alkyl chain was utilized to prepare **MFI** in a form of nanosheets of about 2.5 nm thickness (Figure 2.3) [31]. The hydrophilic part with two quaternary ammonium groups assists to form **MFI** zeolite structure, while the hydrophobic group prevents the crystal growth along *b*-axis. As a result, nanosheets **MFI** are formed. The nanosheets **MFI** cannot condense into 3D zeolite after calcination but the layers are randomly stacked from one to another, which result in a material with slit-shaped mesopores.

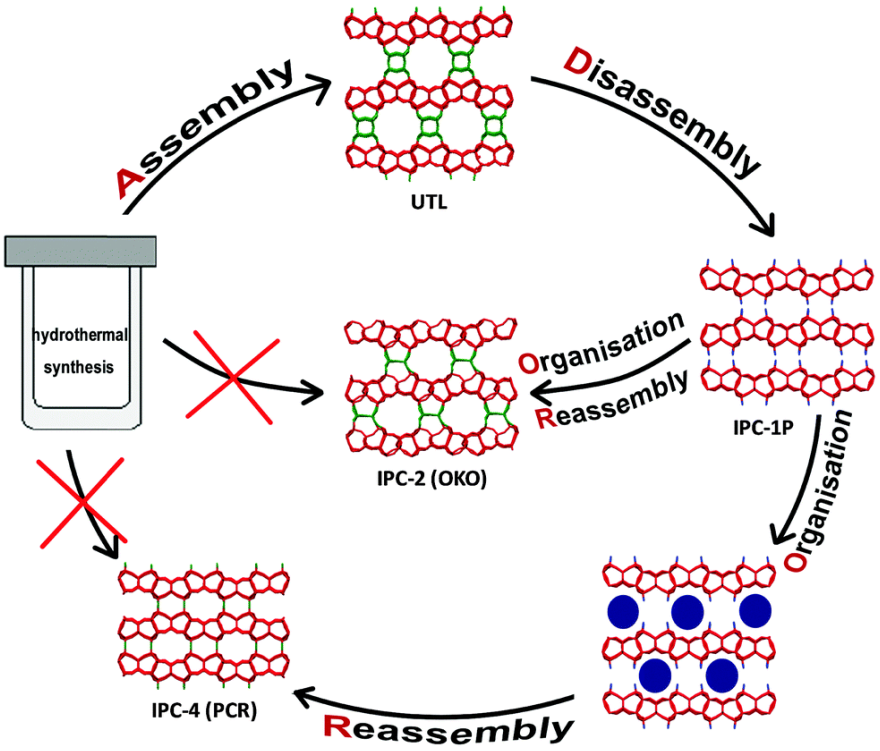

Figure 2.4 The ADOR method scheme [36].

The preparation of 2D layered zeolite described proceeds by bottom-up methods either with conventional or specially designed templates. Zeolite layered precursors can be also obtained by a completely different top-down synthetic protocol: *via* a removal of some structural units from an already synthesized standard 3D zeolite [37]. Recently developed approach to prepare zeolite layers is based on the 3D to 2D zeolite transformation and is a part of the ADOR (Assembly, Disassembly, Organization, Reassembly) mechanism [36,38-40]. Germanosilicate **UTL** has been investigated for the ADOR strategy because of its exceptional structure [41-43]. Generally, germanium atoms are preferentially located at double-four-ring units (D4Rs). The structure of germanosilicate **UTL** is described as silica layers connected with interlayer D4Rs. The Ge-O bonds can be easily hydrolyzed in aqueous solution because of the chemical weakness of Ge-O bonds compared to Si-O bonds. This hydrolysis process results in the selective removal of species from the D4Rs while remaining the siliceous zeolitic layers [36-38,44]. Figure 2.4 shows the scheme of these transformations where the Ge has been chemically selectively removed from the **UTL** structure. The resultant layered material is called IPC-1P. Manipulation with the IPC-1P layers produces a family of zeolites *e.g.,* with **PCR** and **OKO** topologies [38]. Post-synthesis modifications of IPC-1P, likewise in the **MWW** case, were also performed by swelling and pillaring [7,21,23,45-48].

2.2 Metal@zeolites

Zeolites contain interconnected network system of pores with nano-size diameter, which provides sufficient environment to accommodate metal nanoparticles. Encapsulation of metal nanoparticles into zeolites offers the possibility to control the size and shape of the resulting metal nanoparticles [49,50]. Two types of zeolite supported metal nanoparticles can be recognized: (a) metal nanoparticles situated on the outer surface of zeolite matrixes, and (b) metal nanoparticles located in the internal pore systems of zeolite matrixes, as shown in Figure 2.5. The metal nanoparticles in type (a) can easily migrate and aggregate into large particles during the calcination and reduction processes, which are referred to as metal/zeolite. In contrast, the metal nanoparticles in type (b) are well encapsulated in the channels and cavities of zeolites, which are denoted as metal@zeolite. In metal@zeolite catalysts, the uniform channels and pores can limit the mobility of metal nanoparticles, thus endowing the metal@zeolite catalyst with the anti-sintering and anti-leaching properties [51]. In addition, owing to the molecular sieving effect of zeolite support, the metal@zeolite catalysts provide shape selectivity [52]. Furthermore, encapsulation of metal nanoparticles into zeolite matrices enables to manipulate the distribution of metal and acid active sites to design bi-functional catalysts. The confinement of metal nanoparticles and their interaction with zeolite frameworks make that both active sites generate strong metal–acid synergistic effect [53]. Finally, high thermal stability of zeolites allows the performance of metal@zeolite catalysts under harsh condition [54]. Thus, these metal@zeolite materials have received considerable attention during the last decades [51-57].

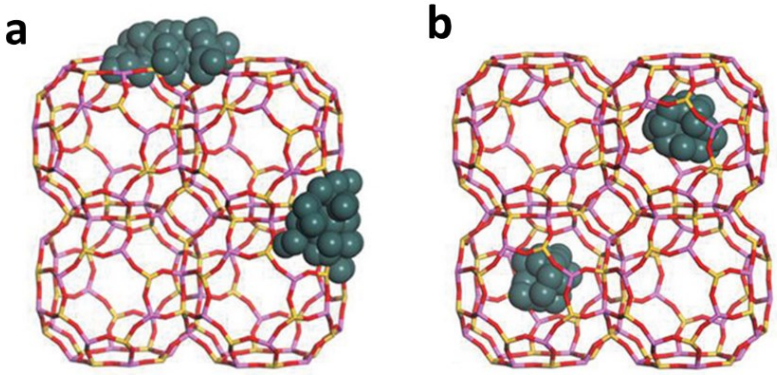

Figure 2.5 Two types of supported metal nanoparticles on zeolites: metal nanoparticles located on zeolite surface, devoted as metal/zeolite (a), metal nanoparticles confined in zeolite micropores, devoted as metal@zeolite (b) [54].

2.3 Synthesis strategies to encapsulate metal nanoparticles into zeolites

The emerged efficient strategies to encapsulate metal nanoparticles into zeolites conditioned recent progress achieved in the field of metal-catalyzed reactions, see Section 2.4. [54,58]. Recent studies have reported numerous methods to confine metal nanoparticles into the pore systems of zeolites to improve the catalytic performance and avoid aggregation/leaching [50,51,53,54,57,58]. When metal nanoparticles are small enough and encapsulated in the cavities/channels/cages of zeolite frameworks, the metal@zeolite catalysts are the most stable and effective. The encapsulation of metal nanoparticles into zeolite matrixes can be classified into several strategies: post-synthetic methods [57], co-crystallization method [50,53], and 2D to 3D zeolite transformation method [59].

2.3.1 Post-synthetic methods

Metal nanoparticles can be introduced into zeolite matrixes by post-synthetic methods such as ion exchange or impregnation followed by reduction [60-62]. Ion exchange-reduction method is the most frequently used approach to introduce metal nanoparticles into zeolites. Generally, in zeolites with heteroatoms in the silicon framework, the negatively charges require to be balanced by alkaline or alkaline earth metals [63]. These charge-balancing cations like Na^+, K^+, can move freely in the channels to ensure the exchange with metal precursors in solutions (Figure 2.6a). After exchange with metal cations, the solid catalysts are collected by filtration or centrifugation. In the case of monovalent cations, the maximum metal loading is equal to the amount of framework heteroatoms. For divalent cations, two Al with close proximity are required. In some cases, probably it will form some *oxo*-species of divalent cations on isolated Al. For trivalent cations, three Al with close proximity are required. The metal precursors need to have the cations form and exhibit smaller size than the pore size of zeolites. The ion-exchanged zeolite catalysts are generally reduced by H_2 to generate metal nanoparticles. In order to minimize the sintering of metal precursors, the reduction temperatures need to be kept as low as possible.

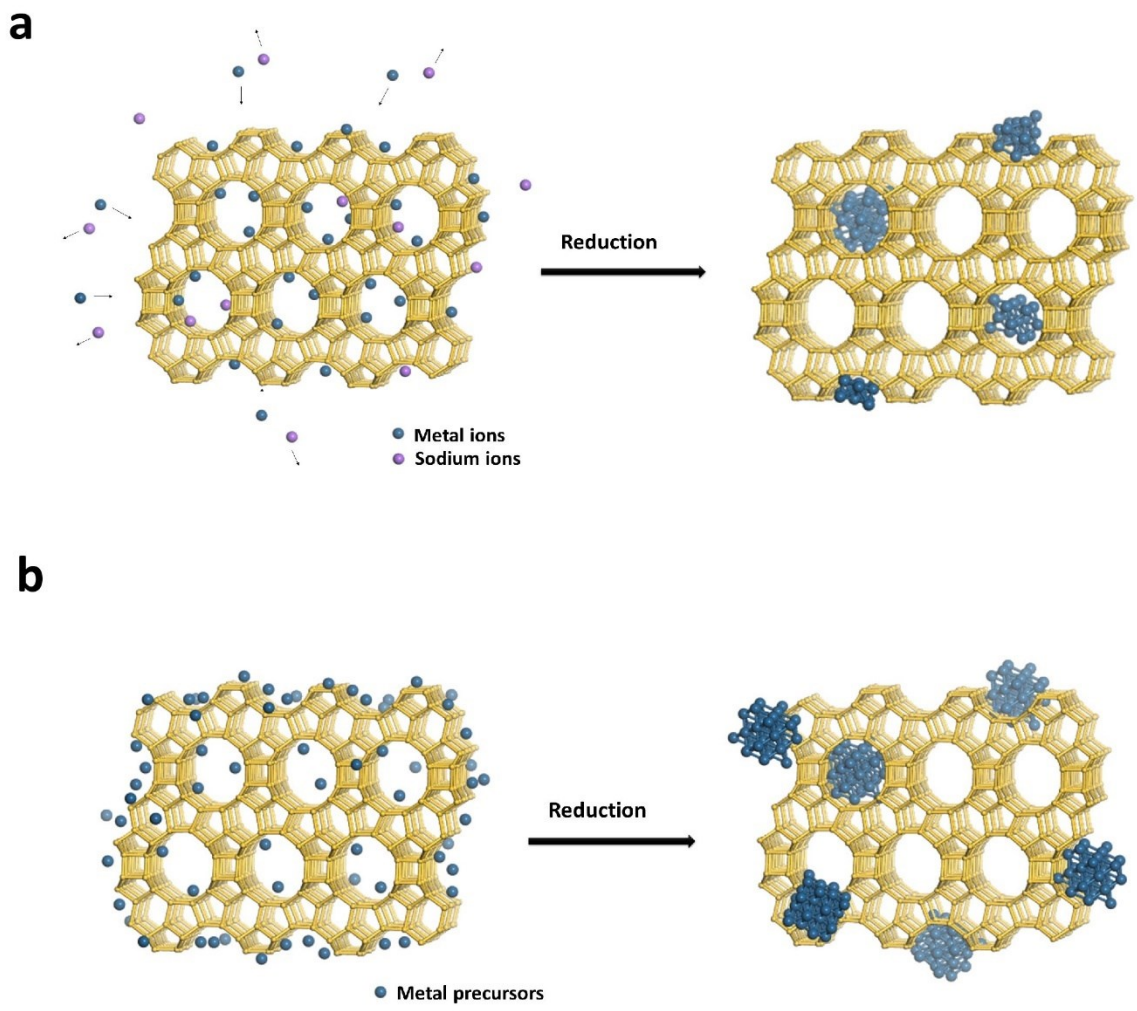

Figure 2.6 Scheme of ion exchange-reduction method (a) and impregnation-reduction method (b).

However, ion exchange-reduction approach is restricted to zeolite frameworks which contain trivalent elements such as Al, B, Ga, *etc.* [50,53]. Moreover, the loading of metal species is limited by the exchange capacity of zeolites. For a higher metal loading, impregnation-reduction method can be employed [64-66]. In this procedure, the loading of metal is not limited by zeolite composition. The scheme of the preparation procedure is shown in Figure 2.6b [67,68]. Impregnation-reduction method includes two steps. Firstly, the zeolites are immersed in a solution containing metal precursors. After removal of the solvent, the overall samples are dried and reduced by H_2 to obtain the metal nanoparticles in the second step.

In the incipient wetness impregnation method, the solution containing the metal species should fill the pores of zeolites homogeneously and bring the metal precursors evenly

distributed uniformly in the solid [69]. The impregnated solid is subsequently dried, calcined and reduced by hydrogen. The metal solutions like nitrate, chloride and carboxylate salts are usually used. However, some gas molecules are still residence in the pores of zeolite, the solution containing metal precursors cannot fill the whole pore volume of zeolites. The metal precursors are frequently concentrated near the external surface of zeolites. After drying, calcination, and reduction, large metal nanoparticles located on the external surface of zeolites are formed [51,56,57]. Generally, this impregnation method is not easy to achieve a homogeneous metal dispersion. However, in some cases, uniform metal dispersion can be obtained by an impregnation technique at very low metal loadings. Therefore, metal nanoparticles encapsulated with zeolite crystals obtained by this impregnation-reduction method have been found with nonuniform particle size distribution depending on the concentration of metal precursors and the topology of zeolites [64-71].

2.3.2 Co-crystallization strategy

The post-synthetic protocols are more effective for large-pore zeolites because metal precursors can more easily access the intracrystalline spaces through large pores. The apertures in small- and medium-pore zeolites may preclude the migration of metal precursors [50,52]. For these zeolites, the most attractive method to encapsulate metal nanoparticles into zeolite matrixes is co-crystallization strategy. This method is not restricted by the pore size of zeolites because the crystallization of zeolites proceeds simultaneously with encapsulating procedure [72,73]. However, most metal cations are easily precipitated as bulk hydroxides in the alkaline synthetic gels. As a result, during the hydrothermal synthesis, commonly metal precursors cannot be encapsulated into zeolites successfully due to the formed large colloidal metal hydroxides, preventing their encapsulation. Therefore, the effective strategy has been developed to encapsulate metal nanoparticles into zeolites by stabilization of metal precursors against precipitation during hydrothermal synthesis process. Thus, the application of different protective methods, such as -N or -S organic ligands, polymer protection agents, have been reported in the co-crystallization method [50,51,53-56,58].

NH_3 and organic amine ligands form metal complexes to encapsulate them into the interior pore system of zeolites. The formed metal complexes are stable in aluminosilicate gel and zeolite can crystallize around these metal complexes during the hydrothermal synthesis.

After calcination, metal precursors merged into nanoparticles, which accommodate in the micropores or fix in zeolites. Iglesia et al. [73] encapsulated noble metal nanoparticles (Pt, Pd, Ru and Rh) into **SOD** (Sodalite, 0.28 nm × 0.28 nm), **GIS** (Gismondine, 0.45 nm × 0.31 nm) through direct hydrothermal synthesis using metal precursors (Pt, Pd, Ru and Rh) stabilized by NH_3 or ethylenediamine (Figure 2.7a). However, the encapsulation of metal nanoparticles within **ANA** zeolite (Analcime, 0.42 nm × 0.16 nm) using the same protocol was unsuccessful due to a higher zeolite crystallization temperature, which results in the precipitation of metal precursors even stabilized by NH_3 or ethylenediamine. Nevertheless, encapsulation of Pt and Ru nanoparticles into **ANA** zeolites was finally achieved by a novel interzeolite transformation strategy from Pt and Ru-containing **GIS** zeolites to **ANA** zeolites. During this process, the metal nanoparticles were occluded within the **ANA** voids. The confinement of metal nanoparticles in zeolite was further confirmed by the hydrogenation of ethylene in the presence of poisoning thiophene, which cannot diffuse into these zeolite pores. The hydrogenation rate decreased in Pt-containing **GIS** and **ANA** zeolites from 2.9 to 2.46 mol-($mol_{surf-metal}^{-1}$–s^{-1}) in Pt-containing **GIS** and from 2.0 to 1.4 mol-($mol_{surf-metal}^{-1}$–s^{-1}) in Pt-containing **ANA**, whereas the impregnated Pt/SiO_2 catalyst became totally inactive.

The metal nanoparticles confined in **MFI** zeolite were also prepared by co-crystallization method in the presence of $[Pd(NH_2CH_2CH_2NH_2)_2]Cl_2$ (Figure 2.7b). Yu and co-workers [74] proved that Pd nanoparticles were located in the intersecting channels of **MFI** zeolite. After the treatment under air and H_2 at 400 °C, the average sizes of Pd nanoparticles were 1.6 nm (Pd loading 0.47 wt%) and 2.2 nm (Pd loading 1.08 wt%), respectively. Finally, the resulting Pd@S-1 catalyst exhibited an outstanding catalytic activity and highly selectivity in H_2 generation by the complete decomposition of formic acid under mild reaction conditions. Furthermore, the catalysts possessed high thermal stabilities and excellent recycling stabilities during formic acid decomposition process because of the small size of Pd nanoparticles within zeolite framework and the basicity caused by the addition of alkali cations.

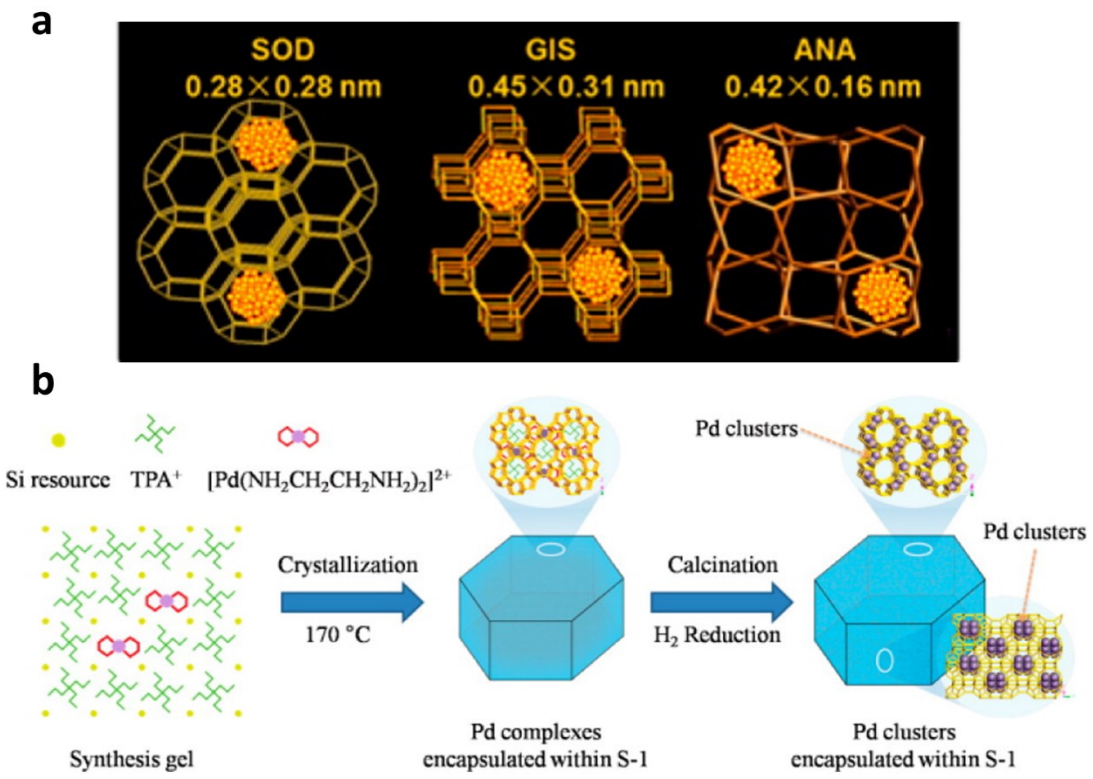

Figure 2.7 Metal nanoparticles encapsulated in **SOD**, **GIS**, and **ANA** zeolites (a) [73]. The synthesis procedure for encapsulation of Pd nanoparticles in nanosized silicalite-1 zeolite (b) [74].

Mercaptosilane can also prevent precipitation, reduction, and coalescence of the metals in the course of zeolite crystallization. The mercapto part binds strongly with the metal cations to form stable metal–sulfur structures, which could prevent the formation of metal hydroxides in the alkaline medium used for zeolite synthesis. The alkoxysilane moiety participates in zeolite crystallization process by formation of Si–O–Si and/or Si–O–Al bonds, which could help to form zeolite framework around metal–sulfur precursors. Various noble metal nanoparticles (Pt, Pd, Ir, Rh, Au, and Ag) have been confined in zeolite frameworks *via* mercaptosilane-assisted synthesis method. For example, Iglesia et al. [72] successfully encapsulated Pt clusters into the small channels of NaA zeolite using bifunctional (3-mercaptopropyl)trimethoxysilane ligands as an assistant agent to stabilize metal precursors against precipitation and to promote the formation of NaA zeolite structures (Figure 2.8a). High-resolution TEM images showed the Pt nanoparticles in NaA zeolite with diameters approximately 1.0 nm after the thermal treatment in O_2/H_2. The XANES and EXAFS results revealed the Pt(II)-S4 complexes were formed after the synthesis. Subsequently calcination

in O_2 and reduction in H_2 at 623 K, the Pt-S features vanished, and the Pt-Pt features were appeared, which further confirmed the formation of Pt clusters in NaA zeolite. The mercaptosilane-assisted confinement strategy has been utilized with different aluminosilicate zeolites with different metal precursors [75-77].

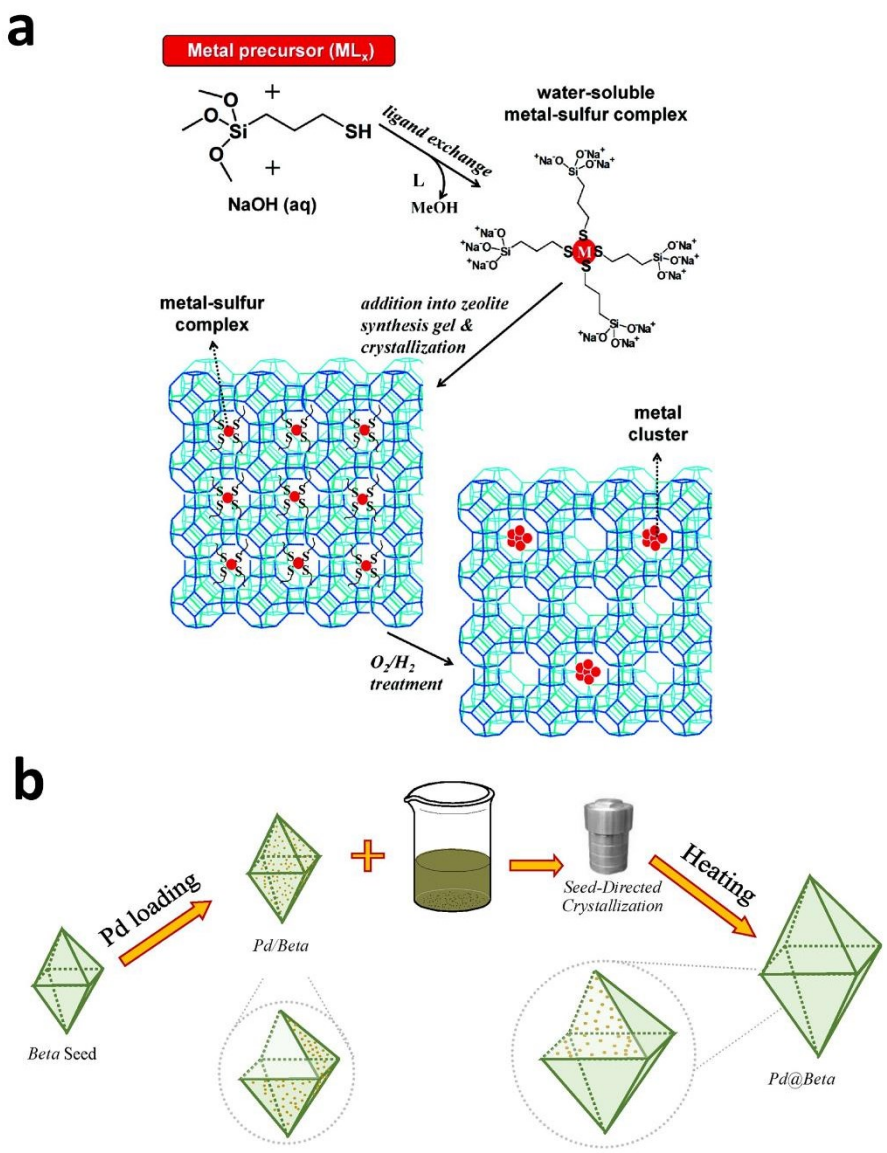

Figure 2.8 Illustration of the synthesis procedure for encapsulation of metal nanoparticles into zeolites using mercaptosilane-assisted approach (a) [72]. The proposed synthesis approach to encapsulate Pd nanoparticles into Beta zeolite (b) [78].

To prevent metal precursors against precipitation in aluminosilicate gel, the seed-directed crystallization route relying on the interaction between metals and zeolites has also been extensively utilized [78-80]. Before the synthesis, metal precursors were introduced on the surface of zeolites by forming metal oxide or metal hydroxide nanoparticles. During zeolite

hydrothermal crystallization, the new formed zeolite can grow from the zeolite seeds containing metal oxide or metal hydroxide nanoparticles. As a consequence, metal nanoparticles can be fixed in zeolites. Figure 2.8b showed the synthesis procedure to encapsulate Pd nanoparticles into Beta zeolite by a seed-directed crystallization route [78]. In addition, polymers can be also employed to prevent metal nanoparticles aggregation during zeolite crystallization process. Poly(N-vinylpyrrolidone) (PVP) is one of the frequently used polymers for stabilizing metal nanoparticles [81]. Chen et al. [82] encapsulated Pd nanoparticles into the mesoporous silicalite-1 zeolite through direct synthesis approach. The PVP was added to keep the formed palladium oxide against aggregation. Subsequently, a modified Kirkendall growth process was employed to encapsulate Pd nanoparticles into the mesoporous silicalite-1 zeolite. After the oxygen and hydrogen atmospheres treatment of as-synthesized sample, uniform Pd nanoparticles with size around 2-5 nm encapsulated in silicalite-1 were obtained. After calcination Pd@mnc-S1 material at 550 °C for 6 h, the diameter of Pd nanoparticles kept almost the same, confirming the high thermal stability, which further indicated that Pd nanoparticles were effectively encapsulated into the silicalite-1 zeolite.

2.3.3 2D to 3D zeolites transformation approach

2D to 3D zeolite transformation method provides an alternative way to encapsulate and stabilize metal nanoparticles into zeolites [59,83-85]. The possibility of layered zeolites modification with preservation of the layer integrity (increase in the interlayer space) provides a chance to insert metal precursors between the layers. The expansion of interlamellar distance by breaking the interlayer hydrogen bonds is a vital process to enable the successive modifications of layered zeolites [17,19]. Swelling the layered zeolites by quaternary ammonium surfactants in basic environment is one of the ways to transform the layered zeolites to hierarchical structures [24]. After the swelling, the interlayer distance of the layered zeolites increases and the layers are complete separated [22]. Recently, Corma et al. [59,83] incorporated subnanometric Pt species during the swelling of MCM-22P (Figure 2.9). Calcination at 540 °C in air removed the organic surfactants between the layers and Pt nanoclusters were formed in MCM-22 zeolite. STEM images proved the subnanometric Pt species around 0.2 – 0.7 nm were trapped in the cups and at the connecting walls between the cups. A few large Pt nanoclusters with size around 0.7-1.0 nm can fill up the supercages

of MCM-22. In addition, the EXAFS spectra showed the coordination number of Pt nanoclusters in Pt@MCM-22 sample is ~4.7, indicating the diameters of most of Pt nanoclusters are less than 0.7 nm. After five cycles of propane dehydrogenation reaction, there is no obvious loss of Pt content in the Pt@MCM-22 catalyst also indicated the Pt nanoclusters are stabilized and trapped into the MCM-22 zeolite structure. The extreme thermal treatment under air and H_2 at 650 °C revealed the high stability of encapsulated Pt nanoclusters in Pt@MCM-22 zeolites compared with Pt/MCM-22-imp obtained by impregnation method.

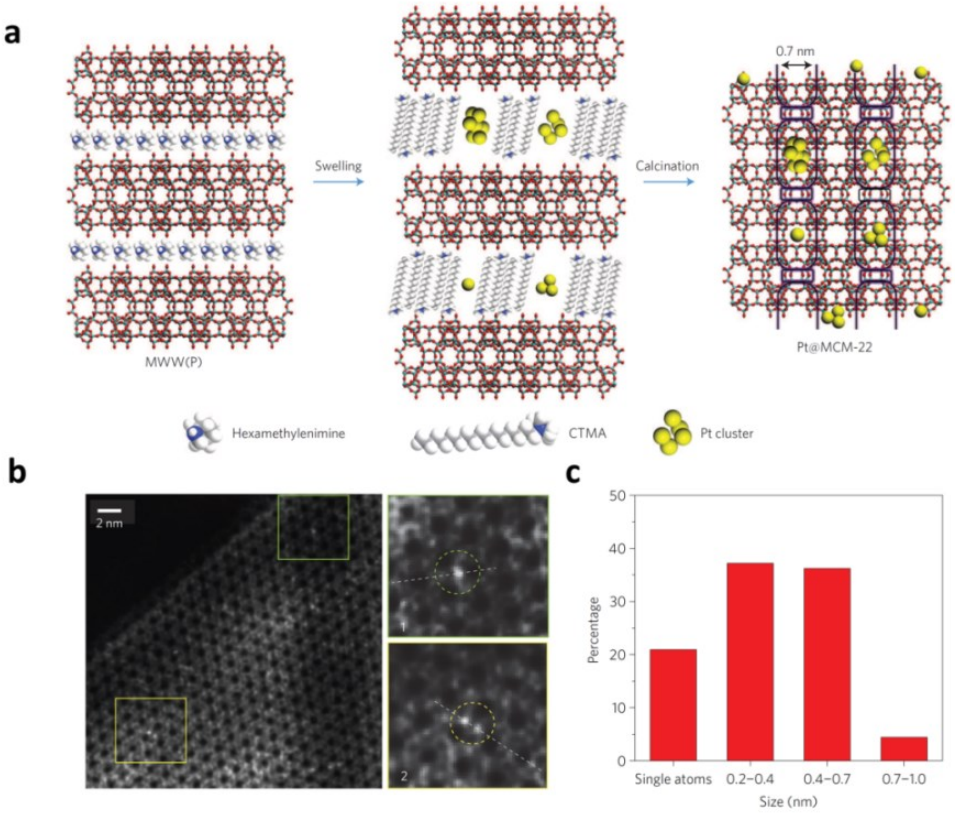

Figure 2.9 Illustration of the 2D to 3D zeolite transformation method for the preparation of Pt@MCM-22 (a), STEM image of Pt@MCM-22 (b), the size distribution of Pt nanoclusters in Pt@MCM-22 catalyst (c) [59].

2.4 Application of metal@zeolite catalysts

2.4.1 Metal nanoparticles catalyzed reactions

Metal@zeolite catalysts have been extensively utilized to catalyze a plenty of reactions including hydrogenation reaction, oxidation reaction, hydrodeoxygenation *etc* [86-89]. If

zeolites without acidity are used as a support, the nature of metal nanoparticles determines the catalytic performance of metal@zeolite catalysts.

Hydrogenation reaction is generally used to saturate molecules through adding pairs of hydrogen atoms to unsaturated groups (-C=C, -NO_2, -C≡N, -C≡C) [90]. The hydrogenation sources include gaseous hydrogen, formic acid, hydrazine, $NaBH_4$, isopropyl alcohol, dihydronaphthalene, *etc* [91]. It is necessary to employ metal species in hydrogenation reaction to increase the selectivity and reaction rate. Noble metals (Pd, Pt, Rh, Ru and Ir) and non-noble metals (Ni, Cu, and Fe) are active components of hydrogenation reaction catalysts [87,89,91]. Encapsulation of metal nanoparticles into zeolites results in small metal nanoparticles due to the confinement of rigid zeolite structures. Small size metal nanoparticles possess more exposed active sites, thus effectively increase the hydrogenation reaction rate [92-94]. Compared with metal nanoparticles supported on nonporous supports, confinement of metal species into zeolites influences the selectivity of hydrogenation reactions due to the defined pore size. This substrate selectivity is provided by the pore systems of zeolite, which are able to prevent bulky molecules to diffuse into the pore and access the catalytic metal active sites.

Hydrogenation of nitroarenes is a typical example concerning the size or shape selectivity over metal nanoparticles encapsulated in zeolite pores. Lida et al. [62] reported an efficient strategy to encapsulate bimetallic nanoparticles into the pores of zeolite. First, Zn-MFI was synthesized under hydrothermal condition. After calcination, Pt precursors were introduced into Zn-MFI by ion exchange method. Finally, sequential thermal treatments under air and H_2 were employed for demetallation of Zn atoms in zeolite frameworks and alloying $PtZn_x$ nanoparticles in **MFI** zeolite pores (PtZn@MFI), as shown in Figure 2.10a. The confined bimetallic $PtZn_x$ nanoparticles exhibited a high selectivity in hydrogenation of *p*-chloronitrobenzene (ClNB) and 1,3-dimethyl-5-nitrobenzene (DMNB) (Figure 2.10b). The C-Cl bond in *p*-chloronitrobenzene (ClNB) was prevented to react and only product was *p*-chloroaniline (ClA). Moreover, in the presence of bulkier 1,3-dimethyl-5-nitrobenzene (DMNB), the PtZn@MFI catalyst was able to hydrogenate the nitro groups in *p*-chloronitrobenzene, indicating the substrate selectivity.

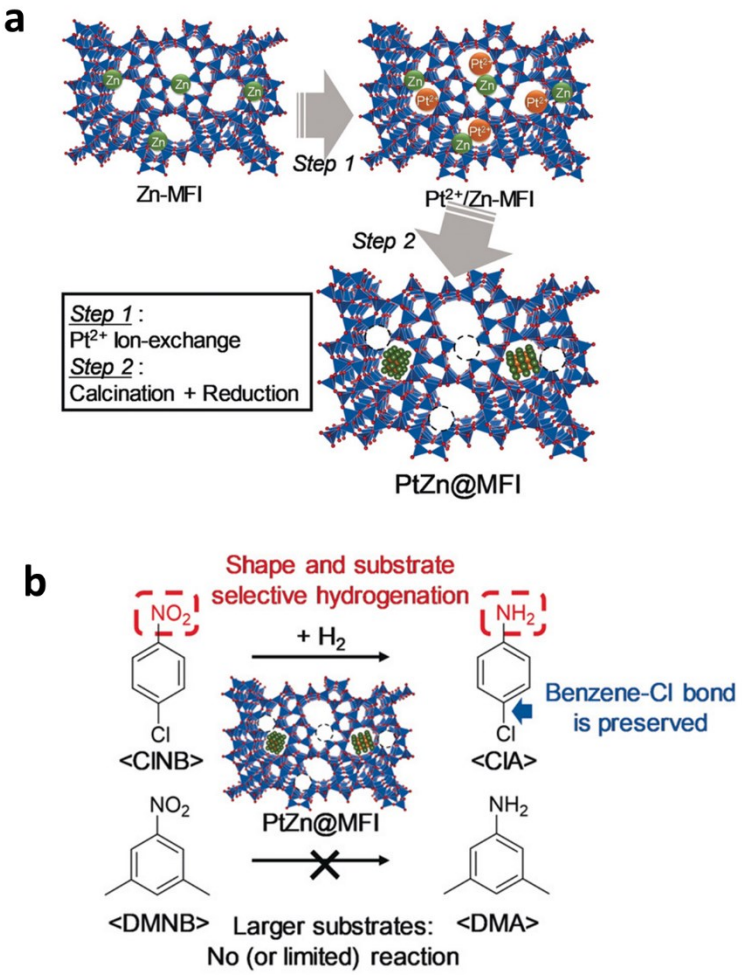

Figure 2. 10 Illustration of the synthesis procedure of PtZn@MFI catalyst (a), the substrate shape selectivity during the hydrogenation of nitroarenes (b) [62].

In some cases, if the reactants have two or more unsaturated functional groups, the desired products can be obtained through the hydrogenation of one group and kept other groups, which is called chemoselectivity [90]. Encapsulation of metal nanoparticles into zeolites is an effective way to control the adsorption of target functional group on metal active sites and govern the chemoselective hydrogenation reactions. Xiao et al. [78] encapsulated Pd nanoparticles into Beta zeolite *via* a seed-directed route. The resultant Pd@Beta catalyst showed the uniformly distributed Pd nanoparticles. In hydrogenation of nitroarenes with multiple reducible groups (4-nitrochlorobenzene and 4-nitrobenzaldehyde), the Pd@Beta catalyst exhibited higher selectivity for the reduction of nitro groups than Pd nanoparticles on Beta zeolite surface prepared by conventional impregnation-reduction method and commercial Pd/C catalyst. The zeolite micropores can sterically control the selective

adsorption of the nitroarenes on the Pd nanoparticles in Pd@Beta catalyst, leading to extraordinary selectivity reduction of nitro groups.

2.4.2 Bifunctional Catalysis

Metal nanoparticles encapsulated in the acidic zeolites can be regarded as the classical bi-functional catalysts [95-98]. These catalysts associate the dehydrogenation/hydrogenation function and zeolites acidic properties, attracting exceptional interest in refining and petroleum chemistry, such as hydroisomerization of alkanes [99-101]. Hydroisomerization is a well-known procedure to convert *n*-alkanes compounds into branched *n*-alkanes [99-101]. For example, after transformation of *n*-alkanes (C_4-C_7 hydrocarbons) to their branched isomers, the octane number increase by 50-90 [102]. The reaction pathways of hydroisomerization of n-alkenes are shown in Figure 2.11. In steps (1), (3), (7) and (8), the (de)hydrogenation reactions occur on the metal active sites, while, the steps (2), (4), (5) and (6) are catalyzed by acidic sites through carbenium rearrangement process [100] [103]. Therefore, the metal–acid balance is important parameter to influence the activity, selectivity, and deactivation of the catalysts [104-106]. Moreover, the textural properties of supported zeolites also have distinct influence on the catalytic performance of metal@zeolite catalysts. Kim et al. [99] supported Pt nanoparticles on bulk **MFI** crystal and nanosheet **MFI** zeolite with different thickness (2-10 nm). In the hydroisomerization of *n*-heptane, the selectivity of branched isomers is enhanced when using nanosheet **MFI** as support, which is attributed to the short diffusion path lengths of nanosheet **MFI**.

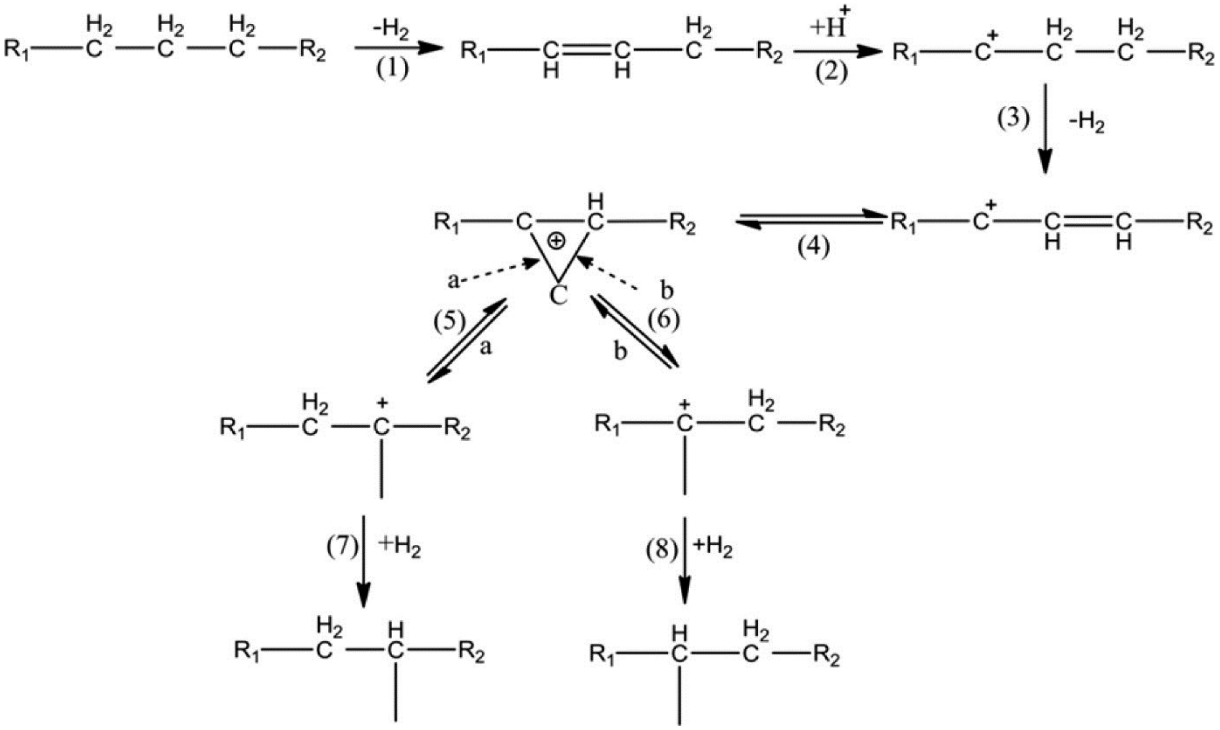

Figure 2.11 Reaction pathways for hydroisomerization of *n*-Alkanes [100].

However, the limited fossil fuels resources have compelled the utilization of renewable sources such as solar energy, wind energy, hydro energy, and biomass. Biomass is an inexpensive, abundant and renewable source of organic matter, which could be used for production of biofuels and other chemical feedstocks [106,107]. The cleavage of C-O and C=O bonds is necessary in their upgrading, which combines the consecutive dehydration, hydrolysis and hydrogenation procedures in the conversion sequence [108]. Therefore, metal@zeolite catalysts with high surface areas, chemical/hydrothermal stability, and acidic properties, have been widely investigated in biomass upgrading [79,109,110].

Lignocellulosic biomass is composed of 40-50 wt% of cellulose, 25-40 wt% of hemicellulose, and 10-25 wt% lignin [111-113]. Among these components, lignin can be converted into liquid oil by two steps. The first stage is depolymerization of lignin to yield bio-oil which contains many reactive oxygenates. The second step is upgrading the bio-oil into transportation fuel by hydrodeoxygenation [114-116]. Lercher et al. [117] studied the depolymerization of organosolv lignin over Ni@HZSM-5, Ni@HBEA, and Ni@SiO_2 catalysts. Lignin has an average molecular weight around 1200 g mol^{-1} that comprises of 7 to 8 monolignol subunits connecting each other by various aryl alkyl ether bonds. After the reductive deconstruction, lignin was converted to alicyclic and aromatic hydrocarbons with yield about 70 wt% at 320 °C, 20 bar

H_2 over Ni@HBEA catalyst. The deconstruction of lignin begins with the cleavage of aryl ether bonds (Figure 2.12). Then the aromatic rings are hydrogenated to cyclic alcohols. Finally, the –OH groups are eliminated *via* dehydration over acid sites of zeolites to cyclic alkenes, which can be further hydrogenated.

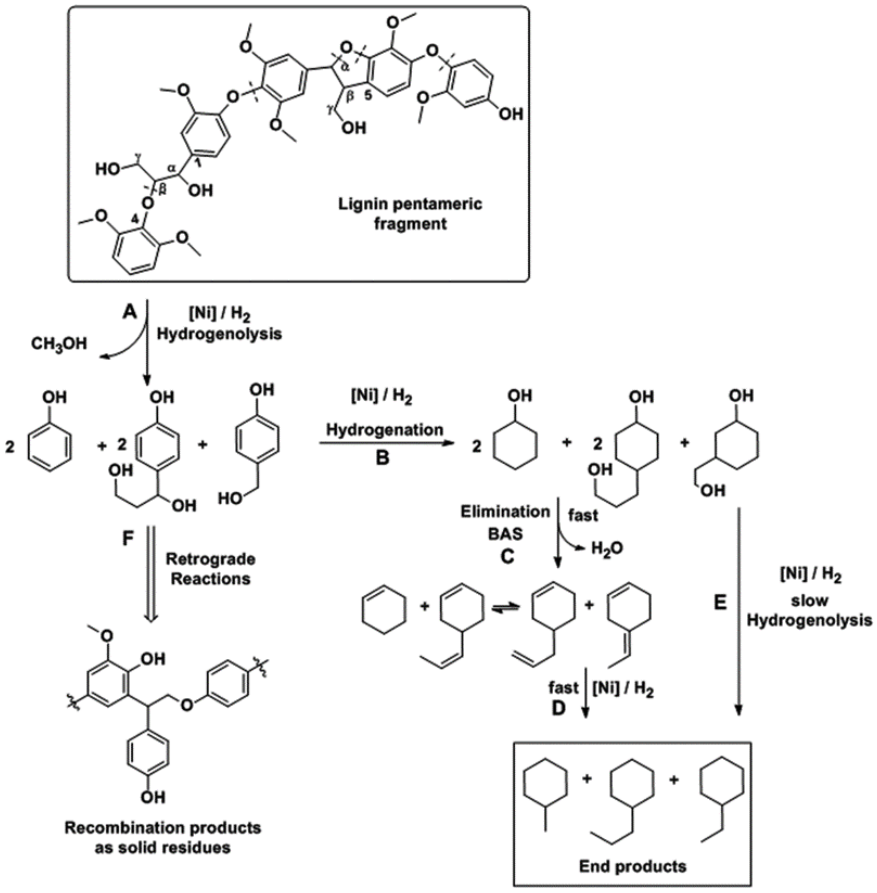

Figure 2.12 Proposed pathways for organosolv lignin deconstruction [117].

In the upgrading step of bio-oil, phenolic species, such as phenol, anisole, and guaiacol have been widely chosen as model compounds to investigate the catalytic activity of various catalysts [106,118]. Owing to the delocalization effect, the $C_{aromatic}$-O bonds are strengthened, causing a higher activation barrier than aliphatic alcohols [98]. For example, the hydrodeoxygenation of phenol over metal@zeolite catalysts could proceed through two pathways [114,119]. The first one is the cleavage of $C_{aromatic}$–OH bond to produce benzene, which can be further hydrogenated to cyclohexane by metal sites. Typically, this reaction pathway is favored at high temperatures [103]. The second reaction pathway is hydrogenation of phenol to cyclohexanone and/or cyclohexanol by metal active sites. Subsequently, cyclohexene can be produced by the dehydration reaction of cyclohexanol. In the last step, cyclohexene is

easily hydrogenated to cyclohexane by metal, which also gives methylcyclopentane by acid-catalyzed isomerization reaction [103]. In hydrodeoxygenation of phenol over metal@zeolite catalysts with large pores, bicyclic products can be also generated by coupling of two phenol-derived species (Figure 2.13) [108,119].

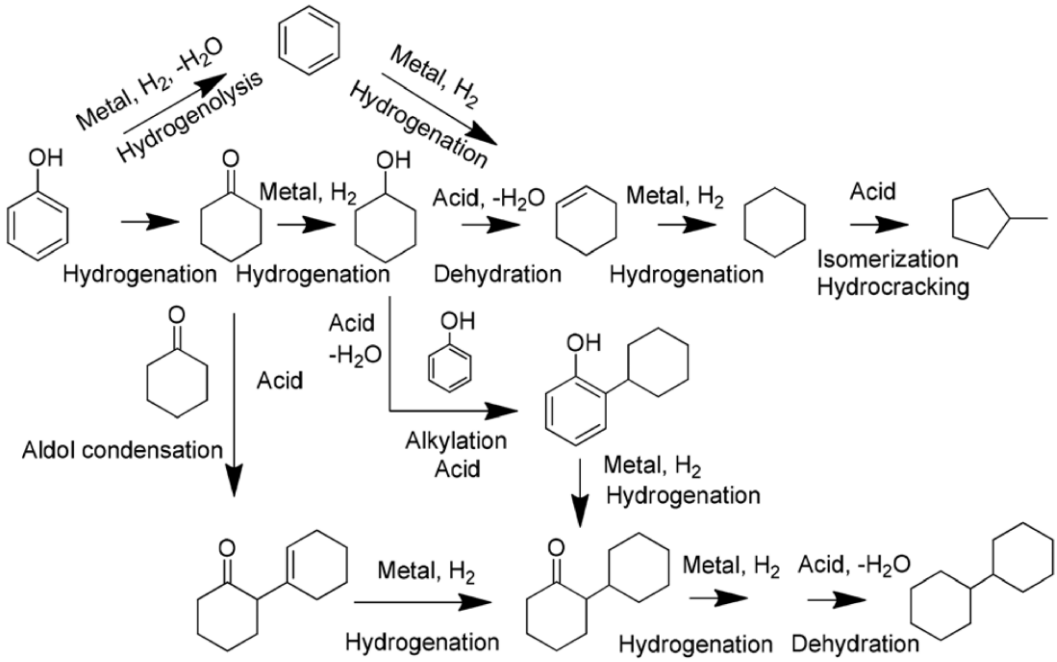

Figure 2.13 Hydrodeoxygenation of phenol over metal@zeolite catalysts [108].

3 Experimental section

3.1 Reagents

Table 3.1 Chemicals used for synthesis and catalytic testing.

Chemicals	Abbreviation	Purity	Origin
1-methylimidazole		99%	Alfa Aesar
1,4-dibromobutane		99%	Sigma Aldrich
(3-chloropropyl)triethoxysilane		95%	Sigma Aldrich
Aluminum nitrate nonahydrate	$Al(NO_3)_3 \cdot 9H_2O$	≥98%	Sigma Aldrich
Ambersep 900 OH			Alfa Aesar
Cab-O-Sil® M-5			Sigma Aldrich
cis-2,6-Dimethylpiperidine		>99%	TCI
Diethoxydimethylsilane	$Si(CH_3)_2(OCH_2CH_3)_2$	≥97%	Sigma Aldrich
Dodecyltrimethylammonium bromide	$C_{12}Br$	≥98%	Sigma Aldrich
Ethylenediamine		≥99%	Sigma Aldrich
Germanium dioxide	GeO_2	≥99.99%	Sigma Aldrich
Hexamethyleneimine	HMI	99%	Sigma Aldrich
Hexadecyltrimethylammonium chloride	$C_{16}Cl$ (CTMA-Cl)	≥98%	Sigma Aldrich
Ludox LS-30			Ludox LS-30
N,N-Dimethylformamide	DMF	99.8%	Sigma Aldrich
n-octane		99.5%	VWR Chemicals
Propene		99.97%	Linde Gas
Platinum(0)-2,4,6,8-tetramethyl-2,4,6,8-tetravinylcyclotetrasiloxane			Sigma Aldrich
Palladium(II) acetate	$Pd(OAc)_2$	99.9%	Sigma Aldrich
Potassium tetrachloroplatinate(II)	K_2PtCl_4	98%	Sigma Aldrich
Platinum(II) acetylacetonate	$Pt(acac)_2$	97%	Sigma Aldrich
Sodium tetrachloropalladate(II)	Na_2PdCl_4	99.99%	Sigma Aldrich
Silicon carbide			Korund Benátky,

			s.r.o.
Sodium aluminate		50–55% Al_2O_3 and 40–45% Na_2O	Riedel-de-Haen
Sodium sulphate anhydrous	Na_2SO_4	100%	VWR CHEMICALS
Sodium hydroxide solution	NaOH	50% solution in water	Merck
Tetradecyltrimethylammonium bromide	$C_{14}Br$	≥98%	Sigma Aldrich
Trimethyloctadecylammonium bromide	$C_{18}Br$	98%	Sigma Aldrich
Tetraethyl orthosilicate	TEOS	98%	Sigma Aldrich
Tetrapropylammonium Hydroxide solution	TPAOH	40% solution in water	Merck
Tetraamminepalladium(II) nitrate solution	$Pd(NH_3)_4(NO_3)_2$	10 wt% in H_2O	Sigma Aldrich

3.2 Synthesis of Pt@MFI_ImILs and Pd@MFI_ImILs

3.2.1 Synthesis of 1-methyl-3-(triethoxysilyl propyl) imidazolium chloride

The imidazolium-type ionic liquid was prepared by stirring 10 mmol (3-chloropropyl)triethoxysilane and 10 mmol 1-methylimidazole in toluene at 70 °C for 18 h under N_2 atmosphere. The ionic liquid was precipitated in diethyl ether, dried in a vacuum oven for 16 h and named as ImILs [120,121].

3.2.2 Synthesis of Pt@MFI_ImILs and Pd@MFI_ImILs

21.3 mg of K_2PtCl_4 or 27.3 mg of Na_2PdCl_4 and 0.33 g ImILs were dissolved in 30 g deionized water, stirred to get the clear solution, named as ImILs-Pt or ImILs-Pd. Pt@MFI_ImILs and Pd@MFI_ImILs were synthesized using the steam-assisted crystallization method. After adding the ImILs-Pt or ImILs-Pd into the synthesis gel with molar composition: SiO_2: 0.0083 Al_2O_3: 0.03 Na_2O: 0.25 TPAOH: 15 H_2O. The synthesis mixture was stirred for 12 h at room

temperature. After that, the gel was dried overnight by lyophilization. Then, the solid was grounded into fine powder. The obtained dry powder was loaded into a glass vial, which was put in an autoclave with 1 mL deionized water at the bottom. The steam-assisted crystallization was performed at 170 °C for 72 h. After collecting the product by centrifugation, calcination under static air was carried out at 550 °C for 6 h to remove the organic species.

3.3 Synthesis of Pt@MCM-22 and Pd@MCM-22

3.3.1 MCM-22P

MCM-22P was synthesized according to the literature from reaction mixture with the molar composition 2.5 Na_2O:Al_2O_3:30 SiO_2:10 HMI:580 H_2O using NaOH, sodium aluminate, Ludox LS-30 and HMI [122]. At the beginning, sodium aluminate and NaOH were dissolved in deionized water. After adding HMI and Ludox LS-30, the synthesis mixture was stirred at room temperature for 2 h. Finally, the synthesis gel was transferred into 1 L Teflon-lined reactor and placed in an oven. The zeolite synthesis was performed at 143 °C for 4 days with rotation rate at 60 rpm. After quenching crystallization by cooling the reactor, the sample was washed with distilled water and dried at 65 °C for 24 h.

3.3.2 Preparation of metal sources

3.3.2.1 Pt-DMF solution

Pt nanoparticles were synthesized by the reduction of $Pt(acac)_2$ in DMF solution [123,124]. 40 mg $Pt(acac)_2$ was dissolved in 80 mL DMF, followed by heating at 140 °C for 16 h. In order to concentrate the Pt-DMF solution, the excess of DMF was removed by evaporation.

3.3.2.2 $Pd(en)_2(Ac)_2$

The $Pd(en)_2(Ac)_2$ complex was prepared by dispersing 80 mg palladium(II) acetate in 4.5 mL ethanol solution containing 0.25 g ethylenediamine, followed by sonication at room temperature for 10 min to get a clear solution [85].

3.3.3 Synthesis of Pt@MCM-22

First, the surfactants ($C_{12}Br$, $C_{14}Br$, $C_{16}Cl$ and $C_{18}Br$) were dissolved in deionized water to get 25 wt% solutions. All the surfactants were exchanged to the OH^- form (C_nOH, n = 12, 14, 16, 18) using Ambersep 900 OH resin. Then, 2 g of MCM-22P, 8 g of deionized water, 40 mL of 25 wt% C_nOH solution and 40 mL of Pt-DMF solution were mixed together and stirred overnight at room temperature. After the reaction, the products were centrifuged and washed with distilled water for 10 times. The products were named as MCM-22P-C_nOH-Pt-DMF (n = 12, 14, 16, 18). The MCM-22-C_nOH-Pt (n = 12, 14, 16, 18) products were obtained by thermal treatment of swollen MCM-22P-C_nOH-Pt-DMF samples under nitrogen and air condition. First, the samples were heated in N_2 atmosphere (at 10 mL min^{-1}) from room temperature to 540 °C (temperature ramp 1 °C min^{-1}). Then, the stream was changed to air and maintained for 5 h.

3.3.4 Synthesis of Pd@MCM-22

The synthesis procedure for Pd@MCM-22 sample was similar as for Pt@MCM-22, although using $Pd(en)_2(ac)_2$ as metal source.

3.4 Synthesis of Pt@IPC-2, Pt@IPC-4, Pd@IPC-2, Pd@IPC-4

3.4.1 Synthesis of UTL zeolite

3.4.1.1 Synthesis of SDA

(6R,10S)-6,10-Dimethyl-5-anizosporo[4.5]decane hydroxide was prepared according to the literature [42,125]. At the beginning, NaOH (17.04 g) was dissolved in distilled water to get a clear solution, followed by adding of 91.98 g 1,4-dibromobutane. The second reagent 2,6-dimethylpiperidine (48.21 g) was added into the mixture dropwise. The mixture was heated at 105 °C overnight, followed by cooling down to 0 °C using the ice bath. Then NaOH was added until the mixture appeared solid to be collected by filtration. After dissolving in $CHCl_3$ and dehydration by $NaSO_4$, the SDA was precipitated in cool diethyl ether. The ^1H NMR spectroscopy was used to confirm the structure of SDA.

3.4.1.2 Synthesis of UTL zeolite

The **UTL** germanosilicate was prepared under hydrothermal conditions. First, the SDA, (6R,10S)-6,10-dimethyl-5-anizosporo[4.5]decane hydroxide, was dissolved in distilled water followed by adding of germanium(IV) oxide. After stirring at room temperature to get a clear solution, silica source (Cab–O–Sil M5) was added and the synthesis gel was further stirred for 1 h. The reaction gel has a molar composition of 0.8 SiO_2: 0.4 GeO_2: 0.5 SDA: 30 H_2O. After that, the synthesis gel was loaded into a 100 mL Teflon-lined autoclave. Then, the zeolite synthesis was performed at 175 °C for 7 days. The product was recovered by filtration and dried at 60 °C for 24 h. Finally, the as-synthesized **UTL** was calcined under static air at 550 °C for 6 h to remove the organic species.

3.4.2 Synthesis of IPC-1P

IPC-1P was obtained by the hydrolysis of calcined **UTL** zeolite. 2 g of **UTL** were dispersed in 300 mL 0.1 M HCl solution and stirred for 16 h at 95 °C. The solid product was recovered by centrifugation and dried at 60 °C for 24 h [37].

3.4.3 Synthesis of Pt@IPC-4

IPC-1P (0.5 g), deionized water (2 g), $C_{12}OH$ (12 g) and Pt-DMF solution (10 mL) were mixed and stirred overnight at room temperature. The swollen IPC-1PSW-$C_{12}OH$-Pt sample was collected by centrifugation and dried overnight. Then, the IPC-1PSW-$C_{12}OH$-Pt was calcined under nitrogen stream from room temperature to 540 °C (1 °C min^{-1}). The temperature was kept for 2 h under air atmosphere. The final Pt@IPC-4 was obtained.

3.4.4 Synthesis of Pt@IPC-2

IPC-1P (0.2 g), 1 M HNO_3 solution (10 mL), platinum(0)-2,4,6,8-tetramethyl-2,4,6,8-tetravinylcyclotetrasiloxane complex solution (0.2 mL) were mixed and reacted at 170 °C for 16 h. The solid was collected, washed with deionized water and dried at 60 °C. Then the obtained solid was calcined under conditions mentioned above to get Pt@IPC-2 sample.

3.4.5 Synthesis of Pd@IPC-4

The Pd@IPC-1P was synthesized by stirring 1 g of IPC-1P in $Pd(en)_2(Ac)_2$ solution overnight at room temperature. Pd@IPC-4 was obtained by calcination of Pd@IPC-1P under static air at 540 °C for 6 h (temperature ramp of 1 °C min^{-1}).

3.4.6 Synthesis of Pd@IPC-2

Pd@IPC-1P (0.5 g), 1 M HNO_3 solution (10 mL) and $Si(CH_3)_2(OCH_2CH_3)_2$ (0.1 g) were loaded in a 15 mL autoclave and heated at 170 °C for 16 h. The solid product was recovered by centrifugation and washed by distilled water. After calcination under static air at 540 °C for 6 h with a temperature ramp of 1 °C min^{-1}, the final product Pd@IPC-2 was obtained.

3.5 Characterization techniques

Powder X-ray diffraction (XRD) measurements were performed on a Bruker AXS D8 Advance diffractometer equipped with a Vantec-1 detector in the Bragg–Brentano geometry using CuKα (λ = 0.154178 nm) radiation with a step size of 0.25 (2θ/min) in 3-40 or 1-40 degree range.

The adsorption isotherms of nitrogen at −196 °C were collected on Micromeritics ASAP 2020 static volumetric apparatus. Before the measurement, the samples were outgassed under turbo molecular pump vacuum at 10 mm Hg. The surface areas (S_{BET}) of samples were calculated in the range of relative pressure p/p_0 = 0.05 - 0.20. The external surface areas (S_{ext}) of samples were evaluated by the *t*-plot method. The total adsorption capacities (V_{tot}) of samples were obtained by the adsorbed amount at relative pressure p/p_0 = 0.99. The micropore volumes (V_{mic}) of samples were obtained by NLDFT algorithm for cylindrical pores.

The metal loading and Si/Al ratio were determined by ICP-OES (ThermoScientific iCAP 7000). Firstly, 50 mg of metal@zeolite samples, 5.4 mL of HCl, 1.8 mL of HF and 1.8 mL of HNO_3 were transferred into the Teflon-lined autoclave and placed in the microwave, then heated to dissolve the metal@zeolite samples. After cooling down, 13.5 mL of H_3BO_3 were added and retreat in the microwave to complex of the surplus HF.

The morphology of samples was obtained by scanning electron microscopy (SEM), using a JEOL JSM-5500LV microscope. Before the measurement, the samples were coated with a thin platinum/gold layer.

The sizes of metal nanoparticles were determined by the analysis of scanning transmission electron microscopy (STEM) micrographs. Zeolite samples were deposited on EMR holey carbon support film on a copper 300 square mesh grid. Imaging was performed using a JEOL NeoARM 200F microscope operated at 200 kV. STEM images were obtained using an annular dark field (ADF) detector. The alignment of the microscope was performed using a standard gold nanoparticle sample. The nanoparticle size distributions were determined using ImageJ software.

^{1}H NMR spectra were recorded on a Varian UNITYINOVA 400 instrument. The chemical shifts are reported in ppm (δ) relative to tetramethylsilane (1H).

Solid-state ^{29}Si and ^{27}Al MAS NMR spectra were recorded on an Avance III HD (Bruker) spectrometer working with a 9.4 T standard-bore superconducting magnet.

The FTIR spectra were measured by a Nicolet iS50 spectrometer with a transmission MCT/B detector. The samples were pressed into self-supporting wafers (the weight of the wafers is in the range 8-12 mg cm^{-2} and the size of the wafers varies from 1.5 to 3 cm^{2}), followed by activation in situ at T = 450 °C and p = 5·10^{-5} Torr for 4 h. The CO adsorption measurements started at room temperature and p = 15 Torr, followed by desorption at T = 25, 50, 100, 150, 200 °C. Then, the spectra were recorded by collecting 128 scans with a resolution of 4 cm^{-1}.

3.6 Catalytic tests

3.6.1 Hydrogenation of nitroarenes

The hydrogenation of nitroarenes was tested in a 50 mL stainless steel reactor connected to a hydrogen supply system. Before the reaction, the metal@zeolite catalyst was reduced under hydrogen at 250 °C for 2 h. The metal@zeolite catalysts (50 mg), *n*-octane (5 mL), and nitroarenes (1.5 mmol) were added into the reactor. After sealing, the reactor was purged with hydrogen to remove air. Then, the reactor was pressurized with hydrogen at 0.3 MPa or

0.6 MPa and started in an oil bath. After reaching the reaction temperature (100 °C), the reaction started by shaking the reactor with a vibrator. After the reaction, the reactor was cooled down using ice water and the remaining gas was released. Finally, the reaction mixture was analyzed by gas chromatography.

The conversion was calculated as: $\text{Conversion} = \frac{N_0 - N_{r(t)}}{N_0} \cdot 100\%$ (1)

The yield was calculated as: $\text{Yield} = \frac{N_{p(t)}}{N_{p(theory)}} \cdot 100\%$ (2)

The selectivity was calculated as: $\text{Selectivity} = \frac{Yield}{Conversion} \cdot 100\%$ (3)

The mass of the active phase of catalysts was calculated as: $m_{metal} = m_{cat} \cdot metal_{content}$ (4)

The initial reaction rate was calculated as: $\text{rate} = \frac{N_0 - N_{r(t)}}{t \cdot m_{metal}}$ (5)

The TOF was calculated as: $\text{TOF} = \frac{N_{p(t)\ at\ \sim 15\ \%\ conversion}}{t \cdot N_{metal}}$ (6)

N_0 – initial amount of reactant, mol;

$N_{r(t)}$ – the amount of reactant, nitroarene, at particular time, mol;

$N_{p(t)}$ – the amount of product, aniline, mol;

t – reaction time.

3.6.2 Hydrogenation of propene

The hydrogenation of propene was performed at atmospheric pressure using a plug-flow fix-bed vertical tubular reactor. First, catalysts (grain size of 0.35 - 0.50 mm) and SiC (20 mg, with the same grain size) were mixed and pressed into a catalytic bed. Before the reaction, the catalysts were reduced by He/H_2 gas mixture (at 32.7 and 6 mL min^{-1} flow rates) to 400 °C for 2 h with a heating rate of 5 °C min^{-1}. After cooling down to room temperature, the reaction started by adding 2 mL min^{-1} of propene to the feed ($C_3H_6/H_2/He$=5/15/80 vol. %) with a total flow rate of 40.7 mL min^{-1}. The regeneration of catalysts was performed at 500 °C for 1 h in the flow of He (flow rate of 32.7 mL min^{-1}) and O_2 (flow rate of 1.7 mL min^{-1}). The conversion and initial reaction rates were calculated as below:

The conversion was calculated as: $\text{Conversion} = \frac{N_0 - N_{r(t)}}{N_0} \cdot 100\%$ (7)

The initial reaction rate was calculated as: $\text{rate} = \frac{N_0 - N_{r(t)}}{t \cdot m_{metal}}$ (8)

N_0 – initial amount of reactant, mol;

$N_{r(t)}$ – the amount of reactant, propene, at particular time, mol;

$N_{p(t)}$ – the amount of product, propane, mol;

t – reaction time.

4 Results and discussion

4.1 Imidazolium-type ionic liquid-assisted formation of MFI zeolite loaded with metal nanoparticles for hydrogenation reactions

Co-crystallization strategy is an attractive method to encapsulate metal nanoparticles into zeolite micropores. The metal nanoparticles encapsulation process is synchronized with zeolite crystallization. However, the metal precursors are easily precipitated to bulk hydroxides in the alkaline environment, which cannot be generally synchronized with zeolite crystallization. Therefore, S- and N- containing ligands have been widely used as protective agent to stabilize metal precursors against precipitation [72,74,80,82,126]. However, S-containing ligands such as mercaptosilanes are generally complicated by poor solubility in aqueous solution, causing inhomogeneous dispersion of metal–sulfur species in synthesis gel [54]. The utilization of N-containing ligands was only successful for the synthesis of Al-rich zeolites at low temperature (T < 390 K) [54]. In this chapter, imidazolium-based ionic liquid (ImILs) was firstly used as protective agent to stabilize metal precursors in co-crystallization strategy. The positively charged imidazolium groups interact with metal precursors ($PtCl_4^{2-}$, $PdCl_4^{2-}$ *etc.*), and the alkoxysilane parts take part in **MFI** zeolite crystallization. The scheme of synthesis procedure of Pt or Pd nanoparticles in **MFI** zeolite with the assistant of ImILs is shown in Figure 4.1.1.

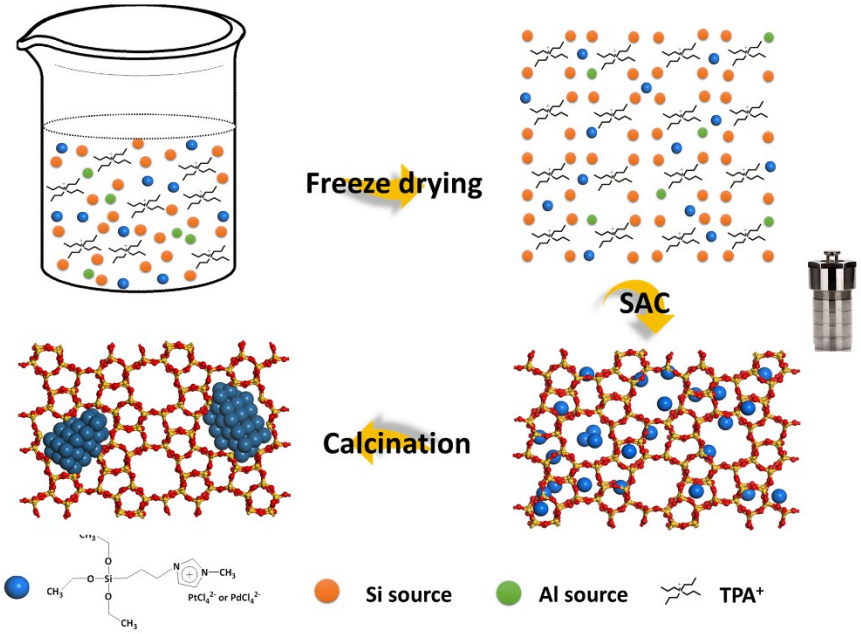

Figure 4.1.1 Schematic illustration of the encapsulation process for ImIL-assisted metal encapsulation during zeolite crystallization.

4.1.1 Characterization of metal@MFI catalysts

The XRD patterns of synthesized metal@MFI, metal@MFI_ImILs, and metal@MFI_Imp materials (metal = Pt or Pd) showed the formation of **MFI** zeolite (Figure 4.1.2). It revealed that the existence of ImILs during the hydrothermal synthesis had no apparent influence on **MFI** zeolite crystallization. Noticeably, the peaks associated with the presence of Pt (39.8° and 46.2°) [127] or Pd (39.9°, 46.4°) [128] phases were not observed in the XRD patterns, indicating the absence of large Pt and Pd nanoparticles. Solid ^{29}Si MAS NMR and ^{27}Al MAS NMR were employed to investigate the chemical state of Si and Al in Pt@MFI_ImILs and Pd@MFI_ImILs compared with the standard **MFI** samples (Figure 4.1.3). In ^{29}Si MAS NMR spectra, there was a broad resonance from the range of -106 ppm to -116 ppm. In addition, the presence of $HOSi(OSi)_3$ and/or $AlOSi(OSi)_3$ sites in **MFI** zeolite framework was confirmed by the resonance between -106 ppm and -109 ppm [129,130]. The existence of $Si(OSi)_4$ groups was demonstrated by the resonance centered at -110 ppm. In the ^{27}Al MAS NMR spectra, a resonance at 55 ppm indicated the presence of tetrahedrally coordinated Al species [131,132]. These results indicated the insignificant lattice defection after encapsulation of Pt and Pd nanoparticles into **MFI** zeolite.

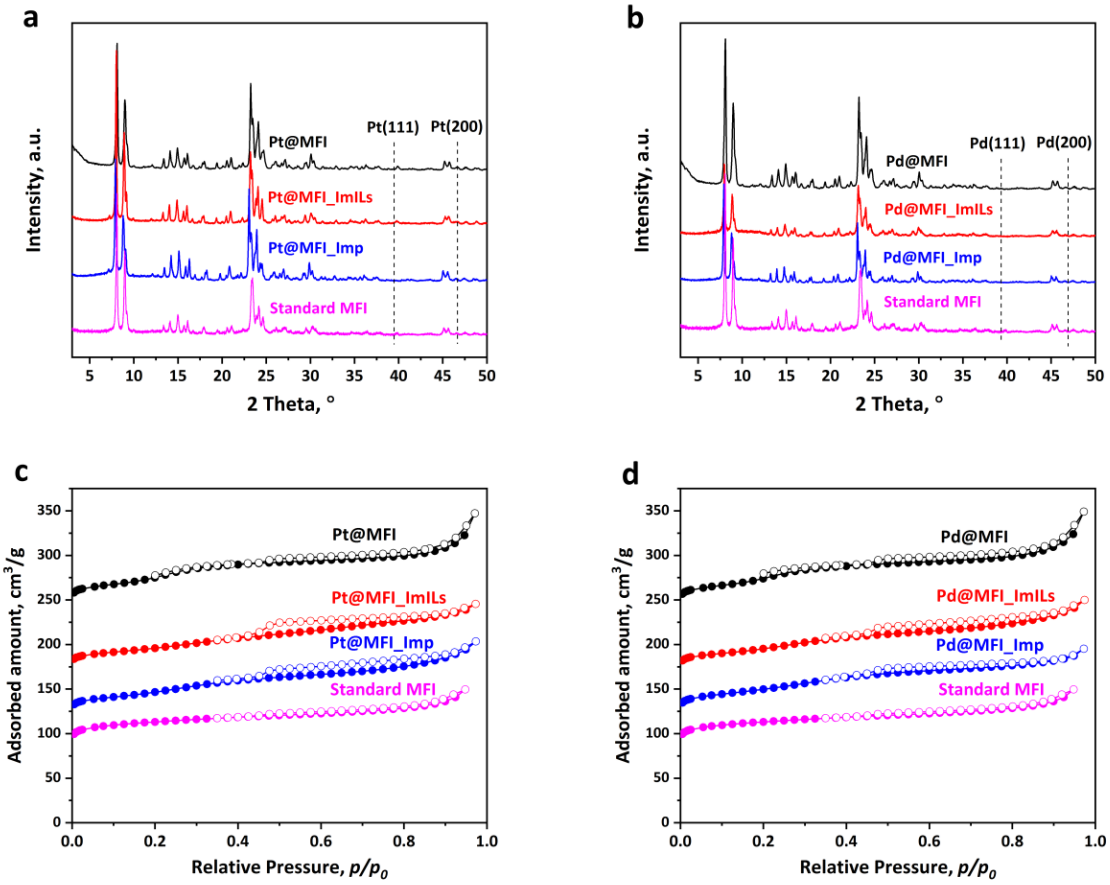

Figure 4.1.2 XRD patterns (a,b) and nitrogen adsorption (●) and desorption (○) isotherms (c, d) of MFI-supported Pt and Pd catalysts *vs.* standard **MFI**. The isotherms for metal@MFI, metal@MFI_ImILs and metal@MFI_Imp were offset vertically by 150, 100 and 50 cm^3 g^{-1} STP, respectively.

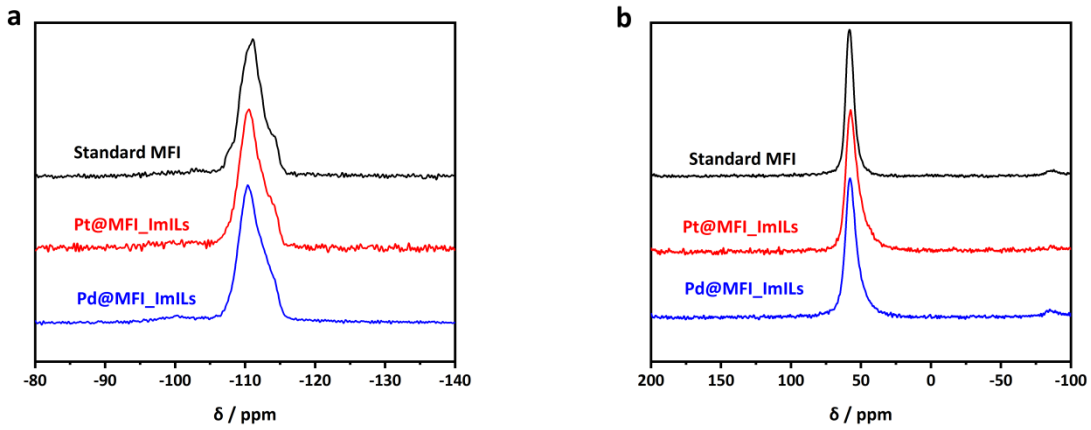

Figure 4.1.3. Solid ^{29}Si MAS NMR (a) and Solid ^{27}Al MAS NMR (b) of metal@MFI_ImILs (metal = Pt or Pd) and standard **MFI**.

The textural properties of metal@MFI, metal@MFI_ImILs, metal@MFI_Imp (metal = Pt or Pd) and standard **MFI** were measured by N_2 sorption at -196 °C (Figure 4.1.2), the textural parameters were summarized in Table 4.1.1. The **MFI** zeolite showed type I(a) isotherm characteristic of microporous solids according to IUPAC definition [133,134]. After introducing metal nanoparticles, the metal@MFI, metal@MFI_ImILs, and metal@MFI_Imp (metal = Pt or Pd) maintained the character of type I(a) isotherm and exhibited some adsorption feature in interparticle space. In addition, there was no difference observed among synthesized materials with and without adding of ImILs. The micropore volumes of metal@MFI_ImILs and metal@MFI_Imp (0.08-0.09 $cm^3\ g^{-1}$) were smaller than the standard **MFI** (0.14 $cm^3\ g^{-1}$), which can be explained due to a partial pore blocking by the metal nanoparticles. The metal contents in metal@MFI, metal@MFI_ImILs, and metal@MFI_Imp were estimated by ICP-OES measurements (Table 4.1.1). In metal@MFI_ImILs, the Pt and Pd content were 0.40 and 0.53 wt%. In metal@MFI_Imp, the Pt and Pd content were higher (0.64 wt% and 0.68 wt% for Pt and Pd, respectively).

Table 4.1.1 Textural parameters, metal loading and Si/Al ratio of the investigated samples.

Samples	S_{BET} $m^2\ g^{-1}$	V_{mic} $cm^3\ g^{-1}$	V_{tot} $cm^3\ g^{-1}$	metal loading (wt%)	Si/Al ratio
Pt@MFI	425	0.14	0.30	0.42	57
Pd@MFI	422	0.13	0.31	0.59	63
Pt@MFI_ImILs	326	0.09	0.22	0.40	66
Pd@MFI_ImILs	324	0.08	0.23	0.53	56
Pt@MFI_Imp	333	0.08	0.23	0.64	62
Pd@MFI_Imp	345	0.09	0.22	0.68	62
MFI_ImILs	383	0.14	0.20	--	58
Standard **MFI**	383	0.14	0.23	--	61

STEM measurements were employed to estimate the size of metal nanoparticles in metal@MFI, metal@MFI_ImILs and metal@MFI_Imp (metal = Pt or Pd). The sizes of Pt and Pd nanoparticles in metal@MFI samples were large with the average diameters around 4 nm and 18 nm, respectively (Figure 4.1.4e and Figure 4.1.5e). Additionally, it is clear that most of the Pt and Pd nanoparticles were located on the outer surface of **MFI** zeolite. In order to depict the protective effect of ImILs on metal precursors during hydrothermal synthesis of

MFI zeolite, the STEM images of metal@MFI_ImILs prepared with the protection of metal precursors by ImILs were shown in Figures 4.1.4a,b and 4.1.5a,b. These images showed that small metal nanoparticles (white round spots) were confined in metal@MFI_ImILs (metal = Pt or Pd). From the corresponding particle size histogram, in Pt@MFI_ImILs sample, the average d_{TEM} was around 1.0 nm, while the d_{TEM} was around 1.7 nm in Pd@MFI_ImILs sample. EDS analysis of Pt@MFI_ImILs and Pd@MFI_ImILs revealed the homogeneous distribution of Pt and Pd elements. The comparison of the diameters of metal nanoparticles in metal@MFI (metal precursors without the protection of ImILs) and metal@MFI_ImILs (metal precursors with the protection of ImILs) proved the protective effect of ImILs on metal precursors during crystallization of **MFI** zeolite. However, it is unavoidable that some metal nanoparticles were situated on **MFI** zeolite surface in metal@MFI_ImILs catalysts. Furthermore, the impregnated catalyst (metal@MFI_Imp) exhibited an uneven distributed Pt and Pd nanoparticles (Figure 4.1.4f and 4.1.5f). The sizes of Pt and Pd nanoparticles were approximately 5 nm and 6 nm for Pt and Pd nanoparticles, respectively. In addition, it is apparent that most of the metal nanoparticles were located on the external surface of **MFI** zeolite. Moreover, the imidazolium-type ionic liquid-assisted encapsulation strategy was also extended to Au nanoparticles in **MFI** zeolite. Figure 4.1.6 shows the STEM images and corresponding particle size histogram of Au@MFI_ImILs.

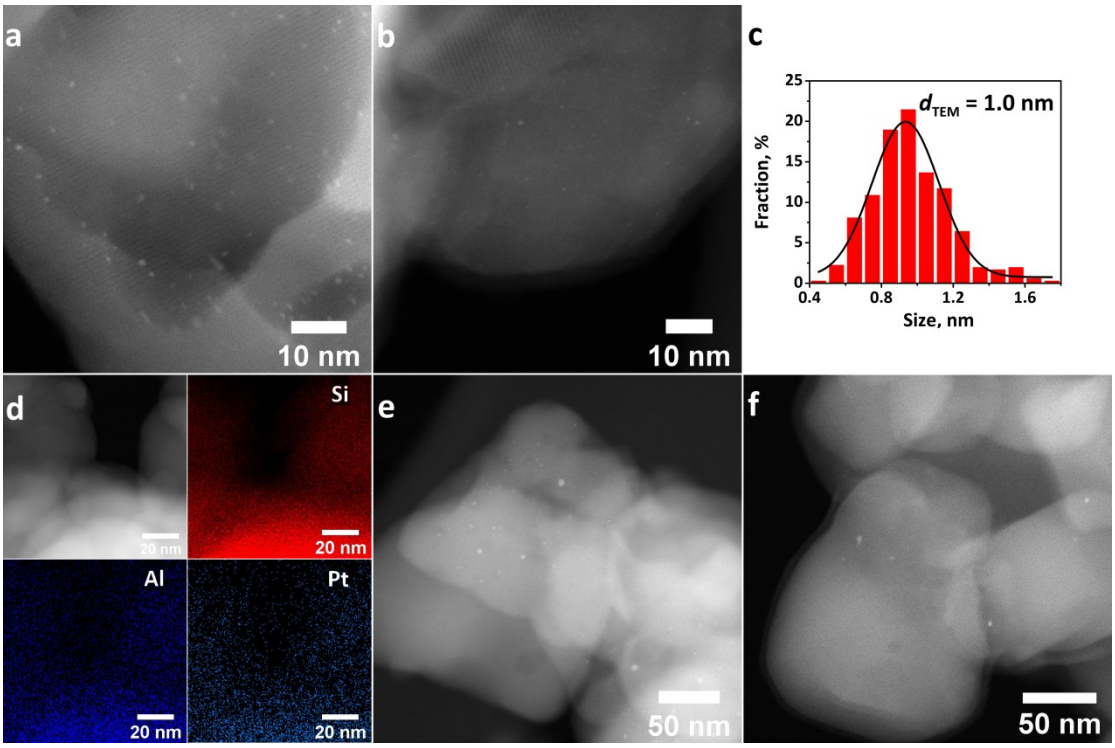

Figure 4.1.4 STEM images (a,b), corresponding particle size histogram (c), and EDS maps of Si, Al, and Pt element distribution of Pt@MFI_ImILs (d); STEM images of Pt@MFI (e) and Pt@MFI_Imp (f).

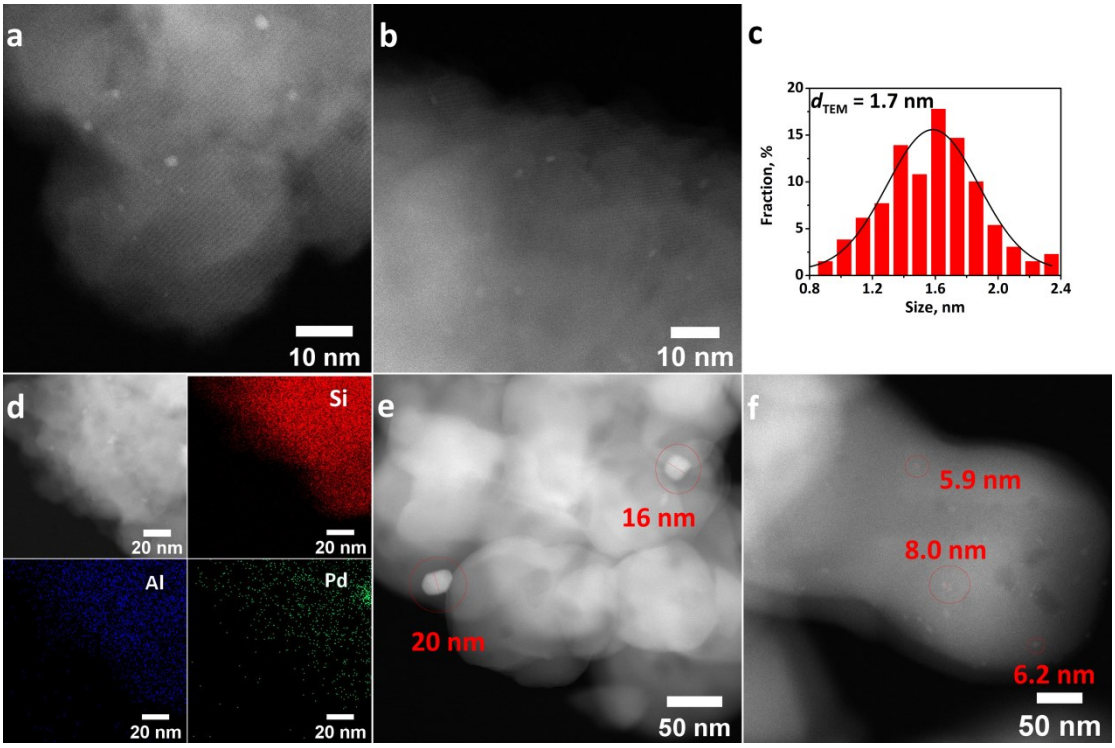

Figure 4.1.5 STEM images (a,b), corresponding particle size histogram (c), and EDS maps of Si, Al, and Pd element distribution of Pd@MFI_ImILs (d); STEM images of Pd@MFI (e) and Pd@MFI_Imp (f).

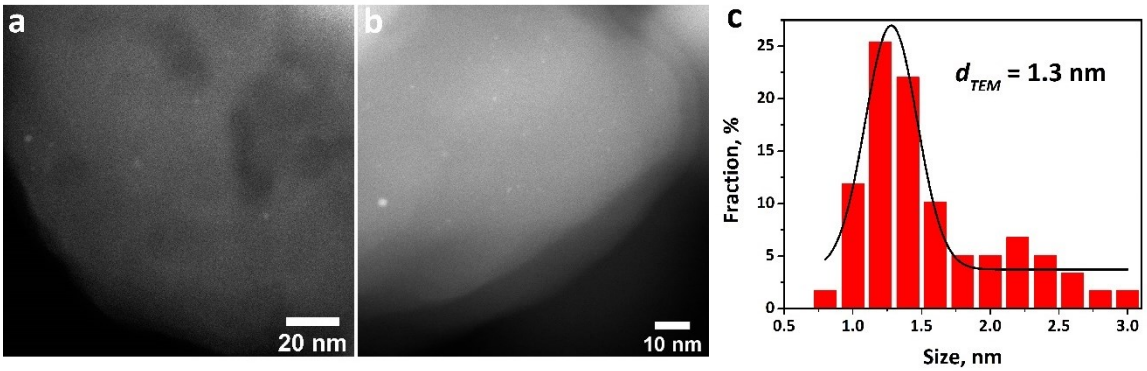

Figure 4.1.6 STEM images of Au@MFI_ImILs (a,b) and corresponding particle size histogram (c).

The **MFI** zeolite contains two intersecting channels: sinusoidal along [100] and straight parallel to [010]. According to the oxygen radii of 0.135 nm, the estimated **MFI** pore size of the channel is 0.54-0.56 nm and the size of the intersection of the MFI-structure is around 0.9 nm in diameter [135,136]. Figure 4.1.7 shows that the *d*-spacing of **MFI** zeolite is approximately 0.55 nm, which further confirms the **MFI** zeolite structure. Notably, the average size of metal nanoparticles was larger than the sinusoidal and intersectional channels of **MFI** zeolite [74]. The Pt and Pd nanoparticles were presumably located at the pores/channels and overgrown by **MFI** zeolite during the crystallization procedure (Figure 4.1.7).

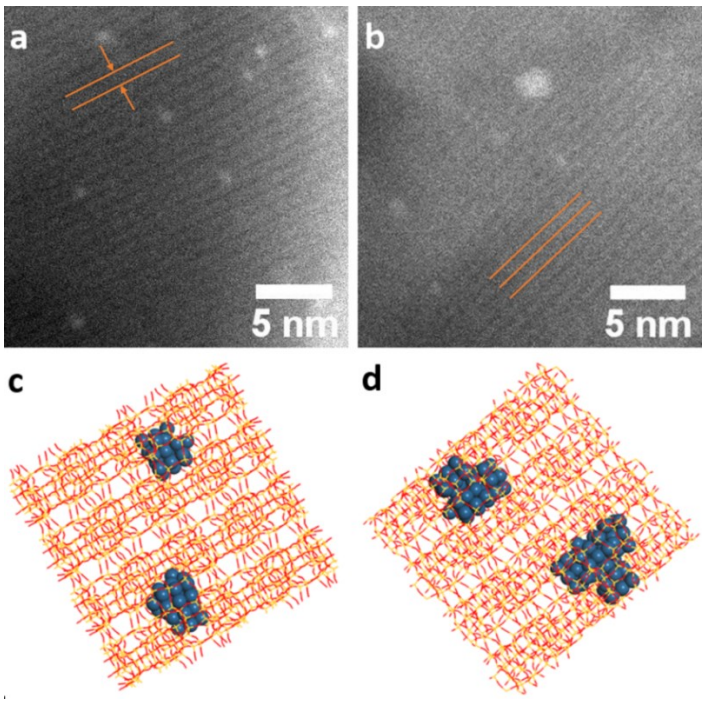

Figure 4.1.7 STEM images of Pt@MFI_ImILs (a), Pd@MFI_ImILs (b) and corresponding location of Pt nanoparticles (c) and Pd nanoparticles (d) confined in the **MFI** zeolite matrix.

4.1.2 Hydrogenation of nitroarenes over Pt@MFI_ImILs

Hydrogenation of nitroarenes is an excellent model reaction to validate encapsulation of metal nanoparticles in zeolite crystals (Pt@MFI_ImILs). The Pt@MFI_Imp was utilized for comparison. Therefore, 4-nitrotoluene (kinetic dimensions: 0.45 x 0.65 nm) and 1,3-dimethyl-5-nitrobenzene (kinetic dimensions: 0.60 x 0.65 nm) were employed to study the shape-selective hydrogenation reactions over Pt@MFI_ImILs and Pt@MFI_Imp. The diffusion of 4-nitrotoluene in **MFI** channel can proceed smoothly, thus 4-nitrotoluene can access the metal active sites on both internal and external surfaces. However, the bulky 1,3-dimethyl-5-nitrobenzene cannot diffuse into the channels of **MFI**, hence the bulky 1,3-dimethyl-5-nitrobenzene only reacts on Pt nanoparticles located on the external surface. Pt@MFI_ImILs showed shape-selectivity depending on the reagent size in hydrogenation of nitroarenes (Figure 4.1.8). 4-nitrotoluene achieved >99% conversion, while the conversion of 1,3-dimethyl-5-nitrobenzene conversion was 5.8%. The selective hydrogenation phenomenon further confirmed that most of Pt nanoparticles were encapsulated in **MFI** zeolite matrix prepared *via* ImILs-assisted crystallization. In contrast, 4-nitrotoluene and 1,3-dimethyl-5-nitrobenzene achieved >99% and 94.8% conversion over Pt@MFI_Imp catalyst. These results revealed that majority of Pt nanoparticles were situated on the outer surface of **MFI** zeolite in Pt@MFI_Imp, which allow the access of metal active sites by 4-nitrotoluene and 1,3-dimethyl-5-nitrobenzene. Moreover, the hydrogenation of 4-nitrotoluene possess a higher initial reaction rate over Pt@MFI_ImILs catalyst than Pt@MFI_Imp (14.5 *vs.* 12.3 mmol/s/g_{Me}), which indicated the smaller size of Pt nanoparticles in Pt@MFI_ImILs catalyst. The catalytic performance of 4-nitrotoluene and 1,3-dimethyl-5-nitrobenzene over Pt@MFI_ImILs and Pt@MFI_Imp were summarized in Table 4.1.2.

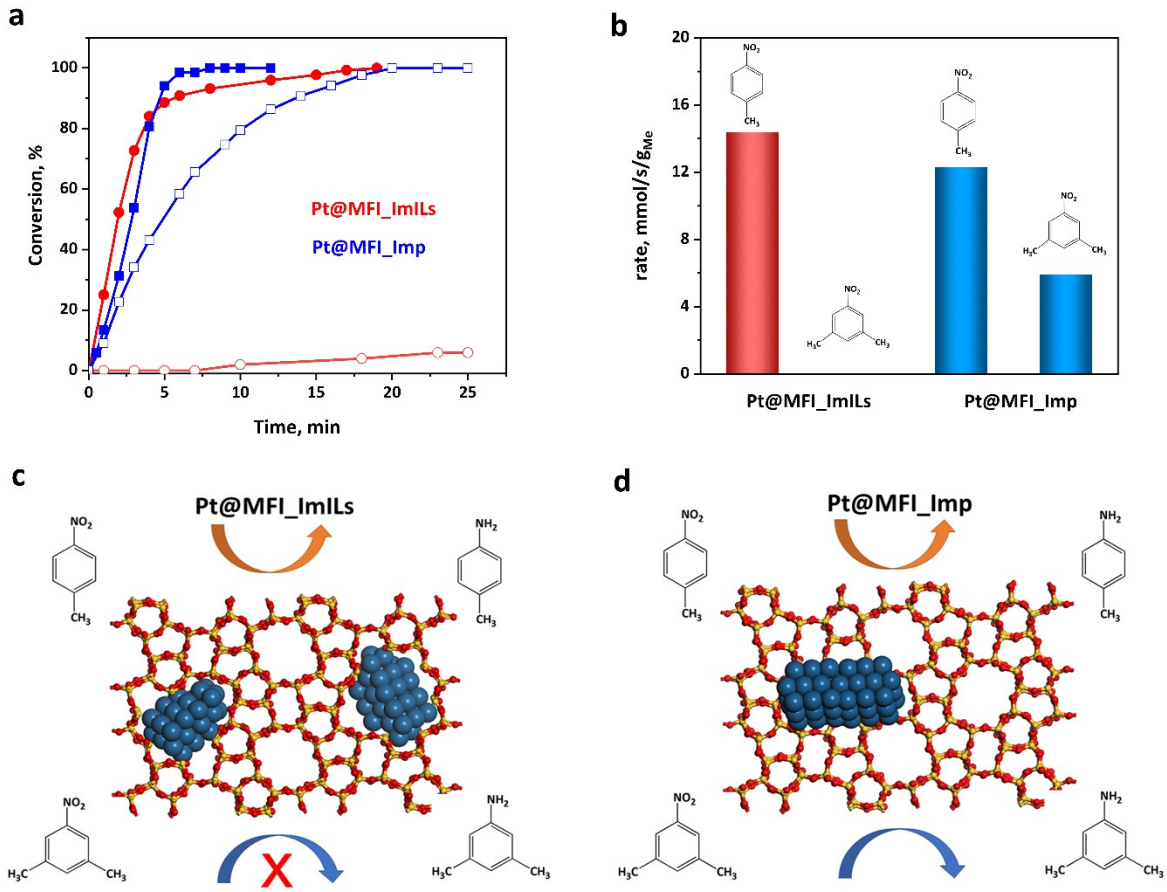

Figure 4.1.8 The hydrogenation of nitroarenes over Pt@MFI_ImILs and Pt@MFI_Imp catalysts. The solid symbols ● and ■ represent as 4-nitrotoluene while the hollow symbols ○ and □ represent as 1,3-dimethyl-5-nitrobenzene (a), the initial reaction rates (b), the schemes for the shape-selective hydrogenation of nitroarenes over Pt@MFI_ImILs (c) and Pt@MFI_Imp catalysts (d).

Table 4.1.2 Hydrogenation of nitroarenes over Pt@MFI_ImILs and Pt@MFI_Imp catalysts, reaction conditions: 100 °C temperature; 0.6 MPa hydrogen pressure; ~50 mg catalyst, 1.5 mmol nitroarenes, 5 mL *n*-octane.

Entry	Substrates	Products	Catalysts	Time [a] (min)	Max. Conversion (%)	Selectivity [b] (%)
1	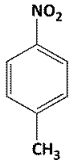		Pt@MFI_ImILs	2	>99	>99

2	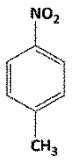	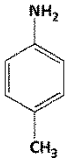	Pt@MFI_Imp	3	>99	>99
3	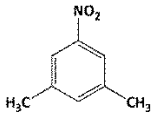	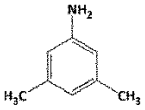	Pt@MFI_ImILs	18	5.8	>99
4	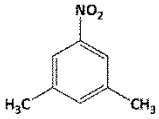	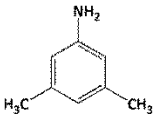	Pt@MFI_Imp	6	94.8	>99

[a] Time to reach 50% conversion;

[b] Selectivity at max conversion (%);

A series of consecutive 4-nitrotoluene hydrogenation cycles enabled to study the reusability of the Pt@MFI_ImILs catalyst (Figure 4.1.9). At the first and second cycles, the conversion and selectivity of 4-nitrotoluene hydrogenation were maintained at >99%. The conversion decreased slightly to 95% at the third cycle. In the following cycle, the conversion of 4-nitrotoluene decreased to 16.9%, and the reaction rate reduced to 0.2 mmol/s/g_{Me}. After four cycles, the Pt@MFI_ImILs catalyst washed with cyclopentyl methyl ether overnight, the conversion and reaction rate recovered to 80.4 and 7.7 mmol/s/g_{Me}, respectively. From the STEM images and size distribution of spent catalyst after the 4-fold recycled and subsequently regenerated Pt@MFI_ImILs catalyst, the average diameter of Pt nanoparticles increased from approximately 1.0 nm (fresh catalyst) to 1.1 nm (spent catalyst), as shown in Figure 4.1.10. The deactivation of Pt@MFI_ImILs catalyst was probably caused by the polymeric or condensation by-products, which cannot be washed completely with cyclopentyl methyl ether.

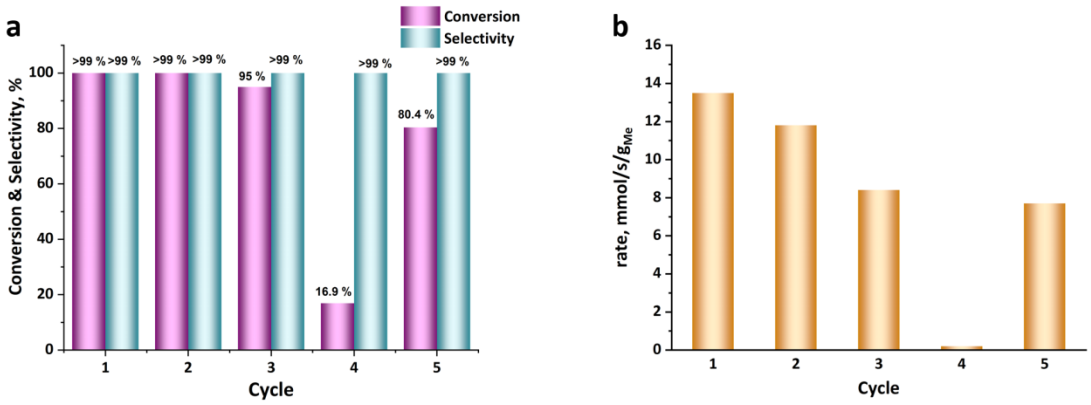

Figure 4.1.9 The reusability investigation of Pt@MFI_ImILs in hydrogenation of 4-nitrotoluene. Conversion and selectivity (a), the corresponding initial reaction rate (b).

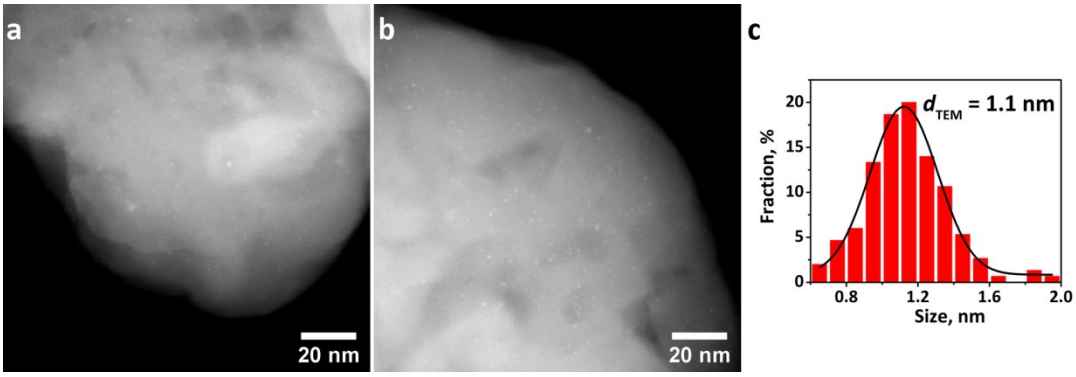

Figure 4.1.10 STEM images of the 4-fold recycled and subsequently regenerated catalyst (a-b), and corresponding particle size histogram (c).

4.1.3 Hydrogenation of propene over Pd@MFI_ImILs

The catalytic performance of Pd@MFI_ImILs catalyst was evaluated by propene hydrogenation and compared with Pd@MFI_Imp under the same reaction conditions (C_3H_6/H_2/He=5/15/80 vol. %; total flow rate: 40.7 mL min^{-1}, room temperature, atmospheric pressure). According to GC measurement, propane was the only product. Undoubtedly, the propene (kinetic diameter: 0.42 × 0.32 nm) and propane (kinetic diameter: 0.46 × 0.30 nm) molecules can diffuse into the channels of **MFI** zeolite and interact with Pd nanoparticles. The time-on-stream plots of the propene conversion over Pd@MFI_ImILs and Pd@MFI_Imp in three cycles are showed in Figure 4.1.11. For Pd@MFI_ImILs catalyst, the conversion of propene achieved around 96%, followed by minor deactivation (at TOS = 105 min, 88%). The regeneration of spent catalysts proceeded under the flow of 5 vol. % of oxygen in He for 1 h at 500 °C. In the following cycles, the conversion of propene maintained approximately 80% over Pd@MFI_ImILs. The conversion of propene over Pd@MFI_Imp was lower and remained

at around 40% for three cycles. In propene hydrogenation, the initial reaction rate as a function of TOS showed similar trend as propene conversion over the Pd@MFI_ImILs and Pd@MFI_Imp catalysts (Figure 4.1.11). For Pd@MFI_ImILs catalyst, the reaction rate was about 30 mmol/s/g_{Me} at TOS = 105 min in the first cycle. In the subsequent cycles, the reaction rate remained at about 25 mmol/s/g_{Me}. For Pd@MFI_Imp, the conversion of propene was lower than Pd@MFI_ImILs and remained at around 9 mmol/s/g_{Me} for three cycles.

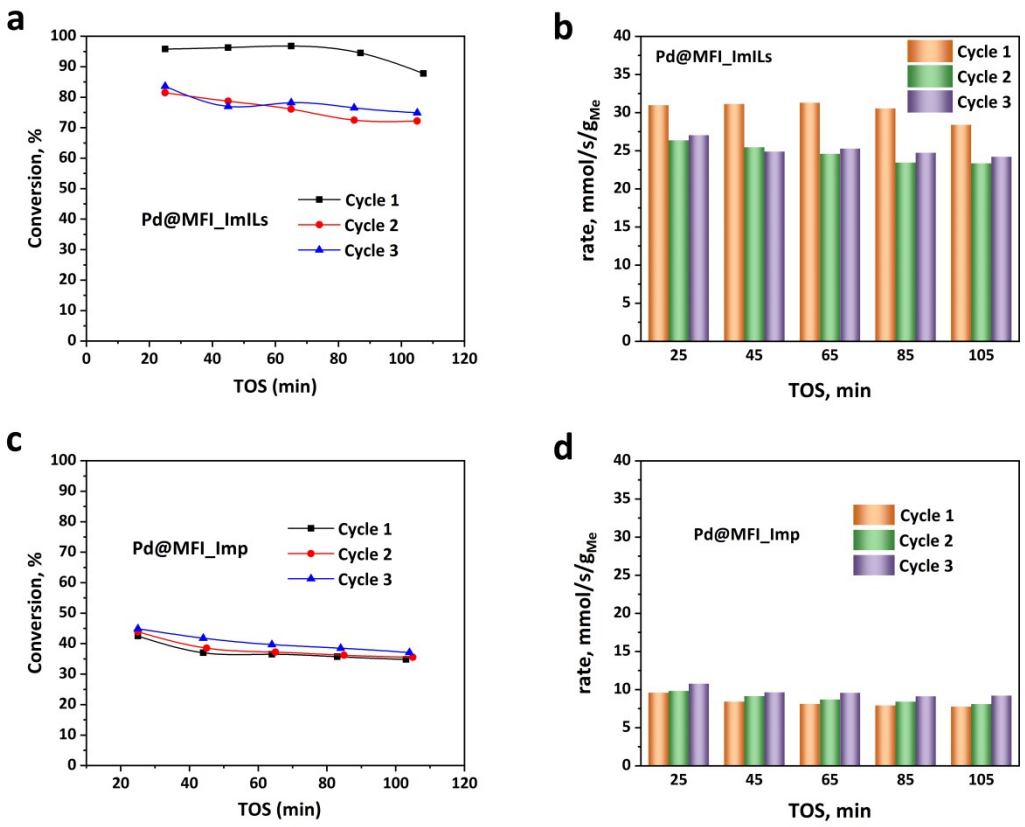

Figure 4.1.11 Hydrogenation of propene over Pd@MFI_ImILs and Pd@MFI_Imp catalysts. TOS *vs.* propene conversion in three cycles over Pd@MFI_ImILs (a) and Pd@MFI_Imp (c), TOS *vs.* propene hydrogenation initial reaction rate over Pd@MFI_ImILs (b) and Pd@MFI_Imp (d).

For metal-based catalysts, the size and dispersion of metal nanoparticles play an important role in the catalytic activity [137]. The catalytic active sites related to various hydrogenation reactions are considered as the low-coordinated metal atoms. The specific activity per metal atom for a certain reaction generally growths with reducing the size of metal nanoparticles [93]. In propene hydrogenation, higher catalytic activity of Pd@MFI_ImILs than Pd@MFI_Imp were supposedly caused by small Pd nanoparticles encapsulated in the **MFI** zeolite (Figure

4.1.5). In addition, the propene conversion over Pd@MFI_ImILs and Pd@MFI_Imp catalysts showed slightly decreasing at TOS, which could be explained by the formed propane or some carbon deposit adsorbed on the Pd nanoparticles. Notably, the deactivation over Pd@MFI_ImILs catalyst after the first cycle was probably caused by a slight aggregation of Pd nanoparticles, which was induced by the regeneration at high temperature before next catalytic test. In the second and third cycles, the propane conversions were similar, which indicated that the Pd nanoparticles maintained their size at approximately 2 nm (Figure 4.1.12).

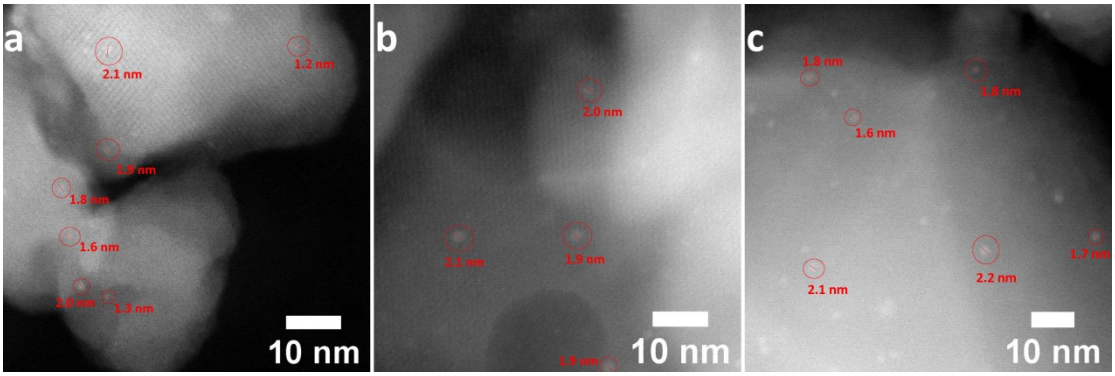

Figure 4.1.12 STEM images of spent Pd@MFI_ImILs after 1st cycle (a), 2nd cycle (b) 3rd cycle (c) of hydrogenation of propene.

In conclusion, a new synthetic method was proposed to encapsulate metal nanoparticles into **MFI** zeolite during the hydrothermal crystallization process. The catalysts synthesized by the ImILs-assisted method possess small and well-dispersed metal nanoparticles. The utilization of ImILs has two important advantages:

- ImILs protect the metal by electrostatic interactions;
- ImILs participate in crystallization of **MFI** zeolite;

The resulting metal@MFI_ImILs (metal = Pt, Pd) have the properties below:

- Most of Pt and Pd nanoparticles were confined within **MFI** zeolite;
- The average diameters of Pt and Pd nanoparticles were approximately 1.0 nm and 1.7 nm, respectively;
- Pt@MFI_ImILs catalyst showed outstanding shape-selectivity in hydrogenation of nitroarenes;
- Pd@MFI_ImILs catalyst showed higher activity in hydrogenation of propene

compared to the impregnated samples;

- The recycle studies in hydrogenation of 4-nitrotoluene and propene revealed that Pt and Pd nanoparticles encapsulated in **MFI** zeolite possess attractive stability.

4.2 Encapsulation of metal nanoparticles by 2D to 3D zeolite transformation approach

Layered zeolite precursors contain zeolite sheets which are kept by relatively weak and easily breakable non-covalent forces [16,19]. About 20 zeolite topologies have layered representatives, such as, MCM-22P, IPC-1P, PreFER, RUB-36, layered MFI, PLS-1, NU-6(1), EU-19, ERB-1 *etc* [7]. Due to the flexible structure, layered zeolites have more possibilities to be modified by post-synthetic strategy than 3D zeolites. Introduction of metal precursors during the layered zeolite transformation process can place metal species into the interlayer space. Subsequently, the calcination can condense the layers into 3D zeolites and confine the metal nanoparticles into the internal pores. Corma et al. [59] firstly reported this strategy to encapsulate Pt nanoparticles into MCM-22 zeolite by this 2D to 3D zeolite transformation process. However, they limited the investigation only to Pt species and the hexadecyltrimethylammonium hydroxide as swelling agent. For this new encapsulation strategy, there still exist some details which need to be investigated. In this chapter, we firstly investigated the effect of the length of swelling agents on the size of Pt nanoparticles in MCM-22 zeolite. Pt nanoparticles were introduced during the swelling using different alkyl chain lengths of surfactants followed by calcination. Then, we chose different metal sources to exhibit the versatility of this method. Pd nanoparticles were encapsulated into MCM-22 zeolite during the swelling process in the presence of $Pd(en)_2(ac)_2$ at room temperature, followed by calcination to condense the layers and encapsulate Pd nanoparticles into MCM-22. Last but not least, this 2D to 3D zeolite transformation approach was expanded to another layered precursor - IPC-1P. Combining the 2D to 3D zeolite transformation and ADOR procedure, metal@IPC-2 and metal@IPC-4 (metal = Pt, Pd) catalysts were successful synthesized.

4.2.1 Synthesis of Pt@MCM-22 with tunable nanoparticle size

4.2.1.1 Characterization of MCM-22P and MCM-22

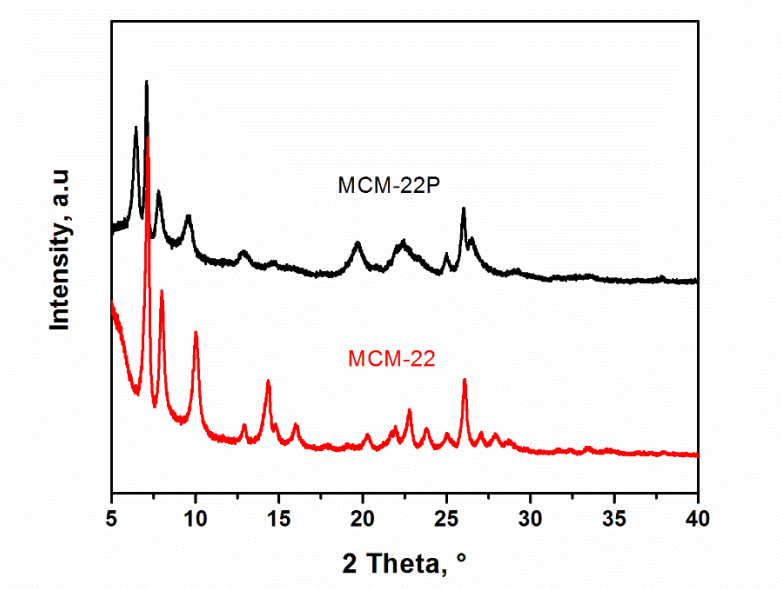

Figure 4.2.1 XRD patterns of MCM-22P and MCM-22.

XRD patterns of MCM-22P and MCM-22 exhibited high crystallinity (Figure 4.2.1). The characteristic Bragg reflections and relative intensities are in a good agreement with the previous reports [138-141]. For MCM-22P, reflection peak at 2θ = 6.5° referred to the interlayer reflection (002), which indicated the layered structure along *c* direction [138-140]. This result demonstrated that the thickness of each individual layer is approximately 2.5 nm. After calcination, the MCM-22P was transformed into three-dimensional MCM-22 because of the condensation of interlayered silanol groups [142,143]. The interlayer reflection (002) shifted and overlapped with the intra-layer reflection (100). From the SEM images of MCM-22P and MCM-22 (Figure 4.2.2), MCM-22P precursors contained thin and oriented platelets with size around 1.60 µm. These platelets were aggregated randomly. After calcination, MCM-22 sample exhibited similar morphology compared to MCM-22P precursor.

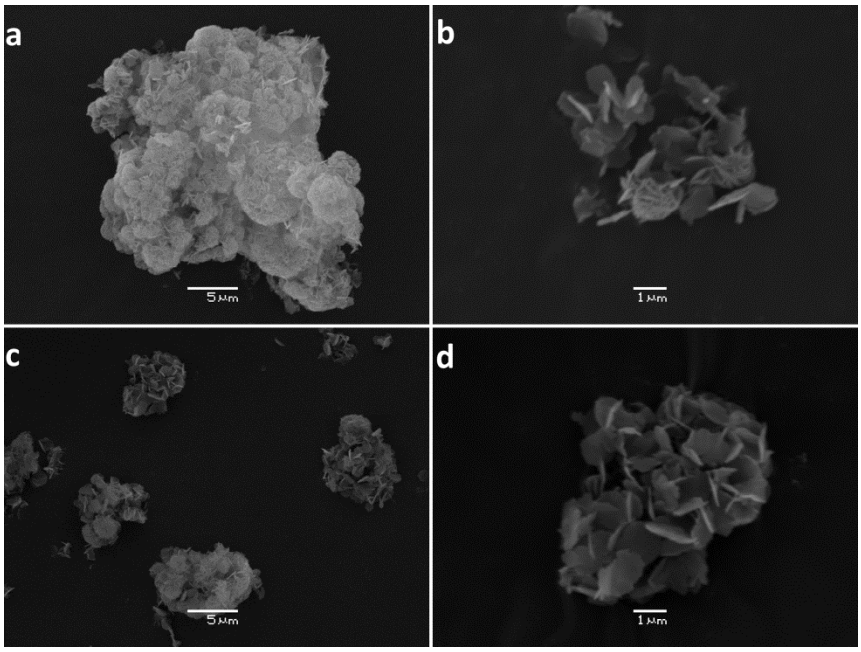

Figure 4.2.2 SEM images of MCM-22P (a,b) and MCM-22(c,d).

4.2.1.2 Swelling MCM-22P with various surfactants

After the swelling process of MCM-22P with surfactants of different lengths ($C_{12}OH$, $C_{14}OH$, $C_{16}OH$ and $C_{18}OH$), all the XRD patterns (Figure 4.2.3a) of swollen samples exhibited a low angle in the range of $2\theta = 1^{\circ}- 3^{\circ}$, which indicated the surfactants were located between the **MWW** layers. Moreover, a broad band in the range of $2\theta = 8^{\circ}$-10° appeared by the overlapping reflection peak (101) and (102). These results confirmed the swelling of MCM-22P with different surfactants was successful.

For the swollen sample MCM-22P-$C_{12}OH$, the reflection peak (001) was located at $2\theta = 2.41^{\circ}$, indicating the *d*-spacing was 3.66 nm. After subtracting 2.5 nm (the thickness of **MWW** layer), the interlayer expansion was 1.16 nm. Compared with the theoretical length of $C_{12}OH$ (1.53 nm), the $C_{12}OH$ surfactant were probably oriented diagonally, or the tails of surfactant were tangled between the layers (Figure 4.2.3b). For the swollen sample MCM-22P-$C_{14}OH$, the *d*-spacing was 4.22 nm calculated by a (001) reflection at 2.09°. The interlayer expansion (1.72 nm) was relatively equal to the diameter of $C_{14}OH$ molecule (1.75 nm). As shown in Figure 4.2.3b, the surfactant molecules were presumably oriented vertically situated in **MWW** layers. Swollen sample MCM-22P-$C_{16}OH$ possessed 5.11 nm of *d*-spacing, thus, the **MWW** layers were expanded to 2.61 nm. In the case of MCM-22P-$C_{18}OH$, the *d*-spacing was 5.55 nm and interlayer distance was 3.05 nm. The lengths of $C_{16}OH$ and $C_{18}OH$ molecules

were around 2.06 nm and 2.25 nm, which was shorter than the interlayer's expansion. In the case of longer alkyl chain swollen agents, one possible explanation was a larger number of surfactant molecules intercalated into the interlayer, causing larger interlayer expansion than the length of surfactants. Figure 4.2.3b shows the possible direction of surfactants between the layers. Table 4.2.1 summarizes the *d*-spacings and interlayer distances of MCM-22P-C_nOH swollen samples. The controllable interlayer expansions were achieved by the adjustment of dimensions of swelling agents. After calcination, the organic species in the MCM-22P-C_nOH (n=12, 14, 16, 18) swollen samples were removed and MCM-22-C_nOH (n=12, 14, 16, 18) samples with **MWW** topology were formed (Figure 4.2.4).

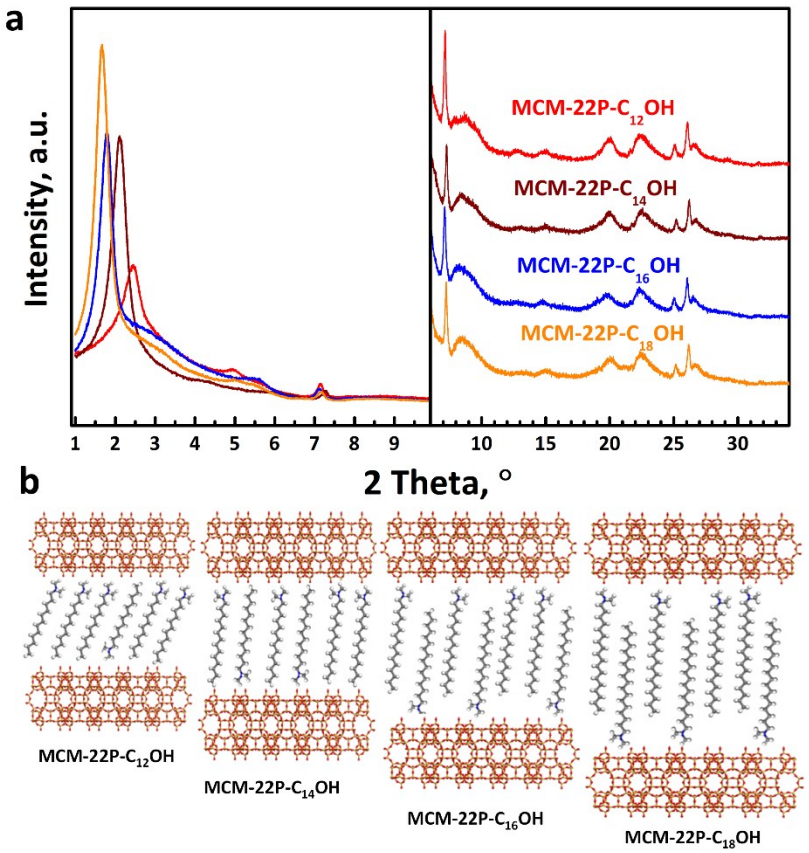

Figure 4.2.3 XRD patterns of MCM-22P-C_nOH (n = 12, 14, 16, 18) swollen samples (a), the schematic diagram of swollen samples with different surfactants (b).

Table 4.2.1 The *d*-spacings and interlayer distances of MCM-22P-C_nOH samples.

	n = 12	n = 14	n = 16	n = 18
2θ	2.41°	2.09°	1.73°	1.59°
d-spacing	3.66 nm	4.22 nm	5.11 nm	5.55 nm
interlayer distance	1.16 nm	1.72 nm	2.61 nm	3.05 nm

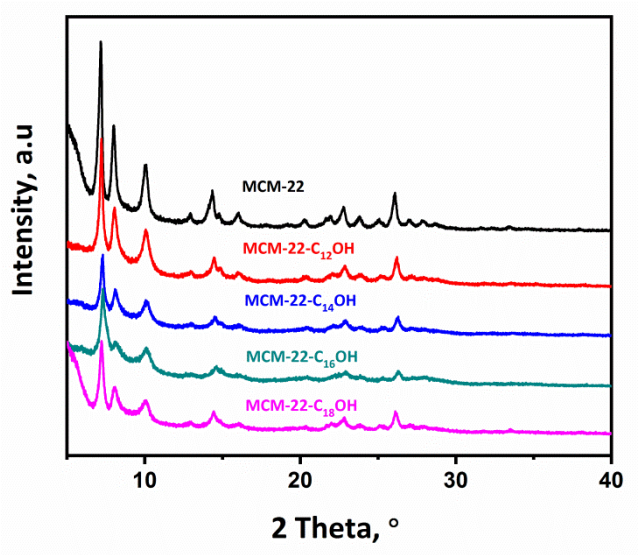

Figure 4.2.4 XRD patterns of MCM-22 and the calcined materials MCM-22-C_nOH (n = 12, 14, 16, 18).

4.2.1.3 Swelling MCM-22P with various surfactants by adding of Pt-DMF

The XRD patterns of swollen samples after the introduction of Pt-DMF (MCM-22P-C_nOH-Pt-DMF) showed the similar characteristic diffraction peaks as the MCM-22P-C_nOH swollen samples (Figure 4.2.5a). The XRD patterns of all MCM-22P-C_nOH-Pt-DMF exhibited a low angle reflection peak in the range of 1° to 3°. In contrast to MCM-22P, the reflection peak (002) at 2θ = 6.5° disappeared. Moreover, these XRD patterns also exhibited the broad peak in the range of 8° and 10° range. The *d*-spacings and interlayer expansions of MCM-22P-C_nOH-Pt-DMF were slightly less than MCM-22P-C_nOH samples (Table 4.2.2). These results indicated that the surfactants solutions were diluted by the addition of Pt-DMF solution, causing smaller expansion compared to pure surfactant solution.

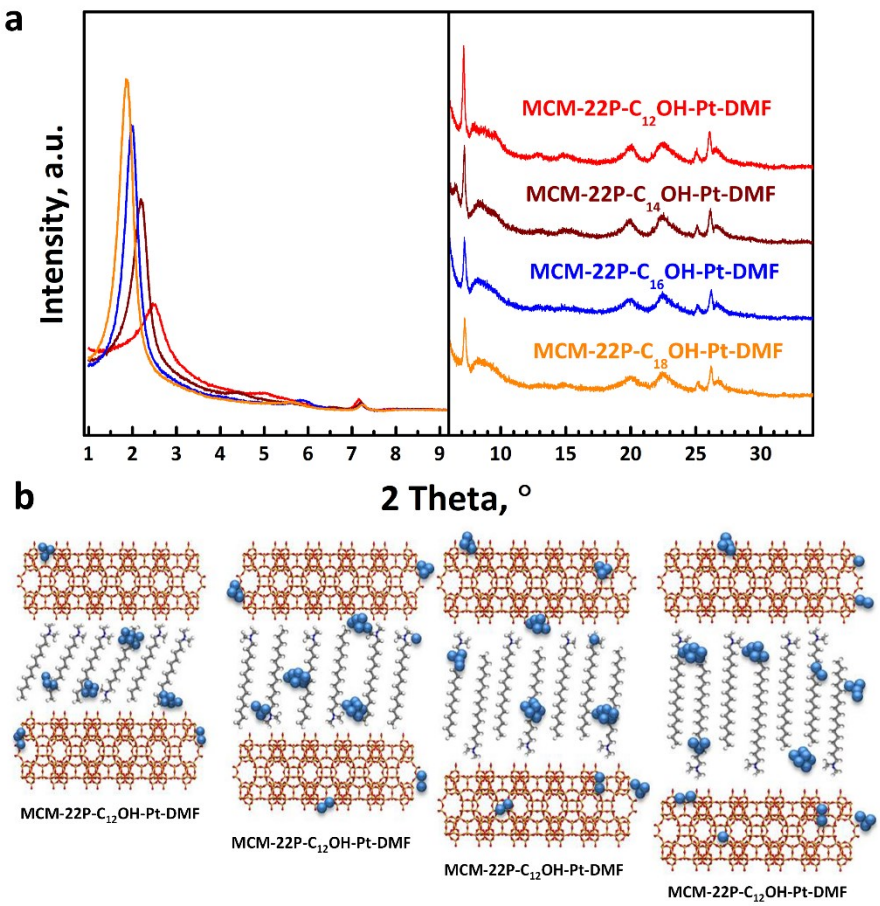

Figure 4.2.5 XRD patterns of the swollen samples MCM-22P-C_nOH-Pt-DMF (n = 12, 14, 16, 18) (a), the schematic diagram of swollen samples with different surfactants by adding Pt-DMF solution (b).

Table 4.2.2 The *d*-spacings and interlayer distances of MCM-22P-C_nOH-Pt-DMF samples.

	n=12	n=14	n=16	n=18
2θ	2.47°	2.16°	1.73°	1.63°
d-spacing	3.56 nm	4.06 nm	5.09 nm	5.39 nm
interlayer distance	1.06 nm	1.56 nm	2.59 nm	2.89 nm

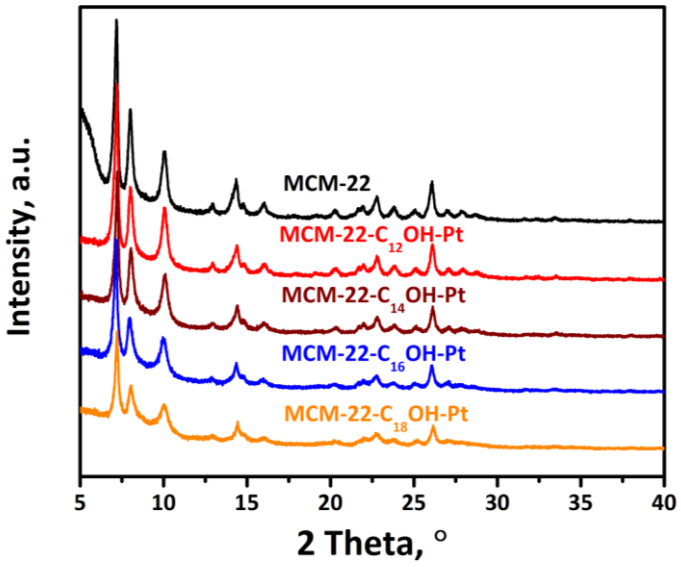

Figure 4.2.6 XRD patterns of MCM-22 and the calcined samples MCM-22-C_nOH-Pt (n = 12, 14, 16, 18).

The swelling process expands the interlayer distance, which is sufficient to insert Pt precursors. Pt-DMF solution can be intercalated into the interlayer distance during the swelling process using C_nOH. Swollen materials MCM-22P-C_nOH-Pt-DMF were calcined to remove organic molecules (surfactants, DMF) and form Pt nanoparticles, which merged in MCM-22 zeolite (MCM-22-C_nOH-Pt). The textural properties of MCM-22-C_nOH (n = 12, 14, 16, 18) were obtained by nitrogen sorption measurement (Figure 4.2.7). All four isotherms exhibited type I isotherm characteristic for microporous samples according to IUPAC [133]. Table 4.2.3 summarizes the textural parameters of four MCM-22-C_nOH-Pt samples. MCM-22-C_nOH-Pt samples possessed BET areas in the range 460 - 530 $m^2\ g^{-1}$ and micropores volumes 0.16 - 0.19 $cm^3\ g^{-1}$. The Pt loading in MCM-22P-C_nOH-Pt samples was measured by ICP-OES (Table 4.2.3). MCM-22-C_{12}OH-Pt, MCM-22-C_{14}OH-Pt, MCM-22-C_{16}OH-Pt, and MCM-22-C_{18}OH-Pt showed similar Pt contents (0.24 wt%, 0.25 wt%, 0.25 wt%, and 0.26 wt%, respectively), indicating the negligible influence of initial *d*-spacing and interlayer expansion on the Pt loading.

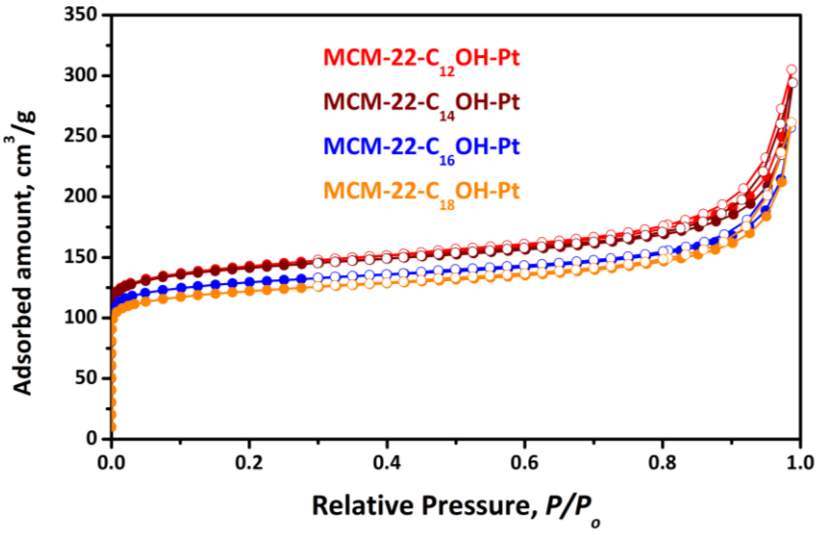

Figure 4.2.7 Nitrogen adsorption (●) and desorption (○) isotherms of MCM-22-C_nOH-Pt samples.

Table 4.2.3 Textural parameters and Pt loading of MCM-22-C_nOH-Pt samples.

Sample	S_{BET} $m^2 g^{-1}$	S_{ext} $m^2 g^{-1}$	V_{mic} $cm^3 g^{-1}$	V_{tot} $cm^3 g^{-1}$	Pt content wt%
MCM-22-C_{12}OH-Pt	508	75	0.19	0.47	0.24
MCM-22-C_{14}OH-Pt	531	69	0.19	0.45	0.25
MCM-22-C_{16}OH-Pt	490	58	0.17	0.40	0.25
MCM-22-C_{18}OH-Pt	459	58	0.16	0.40	0.26

The size and distribution of Pt nanoparticles in MCM-22-C_nOH-Pt (n = 12, 14, 16, 18) were investigated using STEM microscopy. All samples (Figure 4.2.8) exhibited the homogeneous distribution of Pt nanoparticles. The sizes of Pt nanoparticles changed with variation of surfactants. From the Pt nanoparticles size distribution (Figure 4.2.9), the average diameter increased with the length of surfactants (C_{12}OH, C_{14}OH, C_{16}OH, C_{18}OH). When C_{12}OH was used as swelling agent, the interlayer expansion was 1.03 nm. After condensation, the average size of Pt nanoparticles in MCM-22-C_{12}OH-Pt was 0.85 nm. For MCM-22-C_{14}OH-Pt (interlayer expansion of 1.56 nm in swollen samples), the average diameter of Pt nanoparticles increased to 1.00 nm. When the swelling process using C_{16}OH and C_{18}OH surfactants, the interlayer expansions grown to 2.59 and 3.05 nm. And the average sizes of Pt nanoparticles increased to 1.55 and 2.04 nm, respectively. The results evidenced that the average diameters of Pt nanoparticles depend on the interlayer expansion of swollen

samples. Pt nanoparticles were inserted into the interlayer space during the swelling process. Subsequent calcination step removed organics and formed the Pt nanoparticles. The sizes of Pt nanoparticles probably relied on the amount of locally neighboring Pt nanoparticles that were feasible to aggregate, which were controlled by the length of swelling agent.

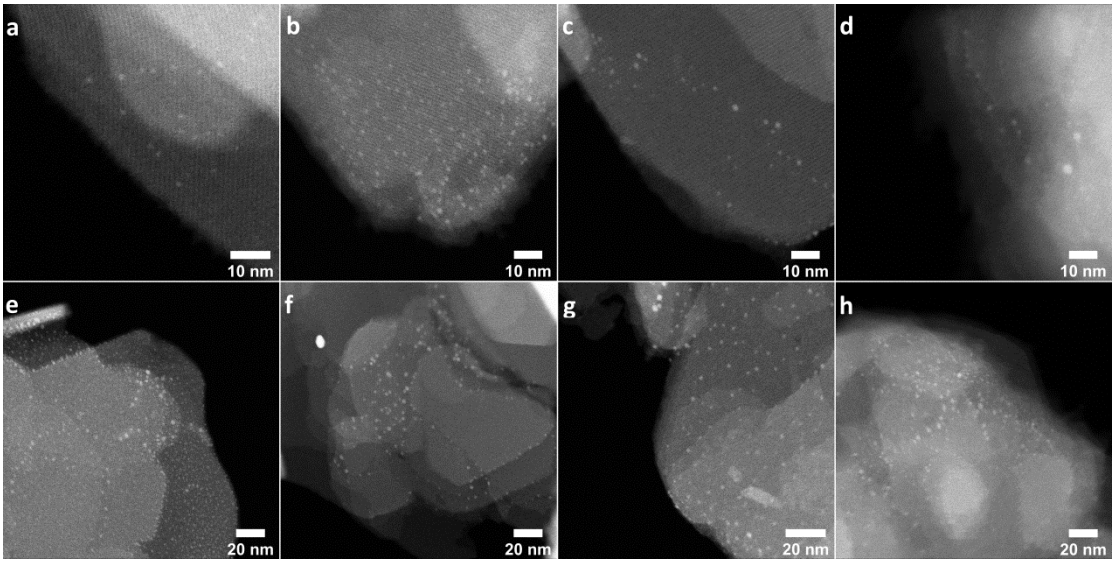

Figure 4.2.8 STEM images of MCM-22-C_nOH-Pt: n = 12 (a,e), n = 14 (b,f), n = 16 (c,g), n = 18 (d,h).

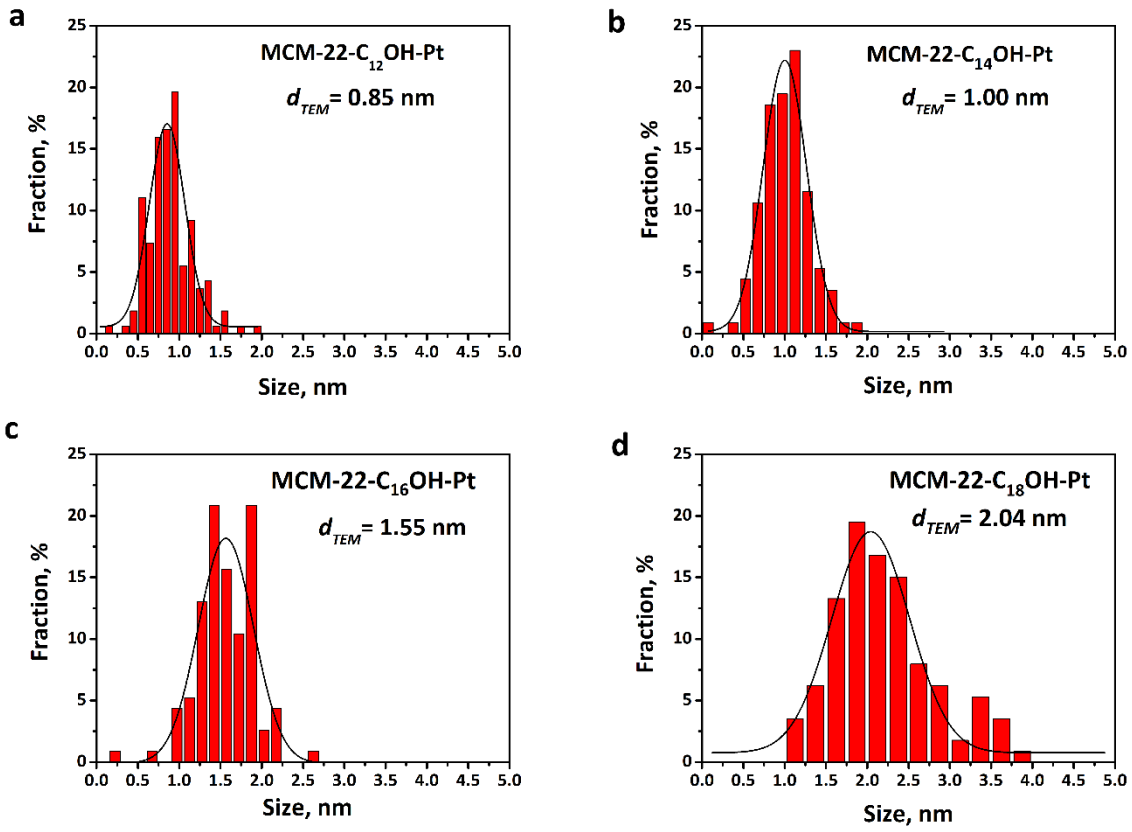

Figure 4.2.9 Particle size distributions of MCM-22-C_nOH-Pt (n = 12, 14, 16, 18).

The pore diameter of 10-ring in MCM-22 is 0.41 × 0.51 nm and the size of internal cavities of is 1.82 × 0.71 × 0.71 nm [25]. In some cases, the diameter of the Pt nanoparticles was smaller than micropore size, revealing that the Pt nanoparticles were confined into MCM-22 zeolite. In other cases, the size of Pt nanoparticles was larger than the micropore size, which can be interpreted that Pt nanoparticles were located at the defective sites in MCM-22 zeolite framework. STEM images (Figure 4.2.10) further showed the large size of Pt nanoparticles merged into MCM-22. Clearly, due to the Pt nanoparticles stuck between the layers of MCM-22, the layers were not fully connected.

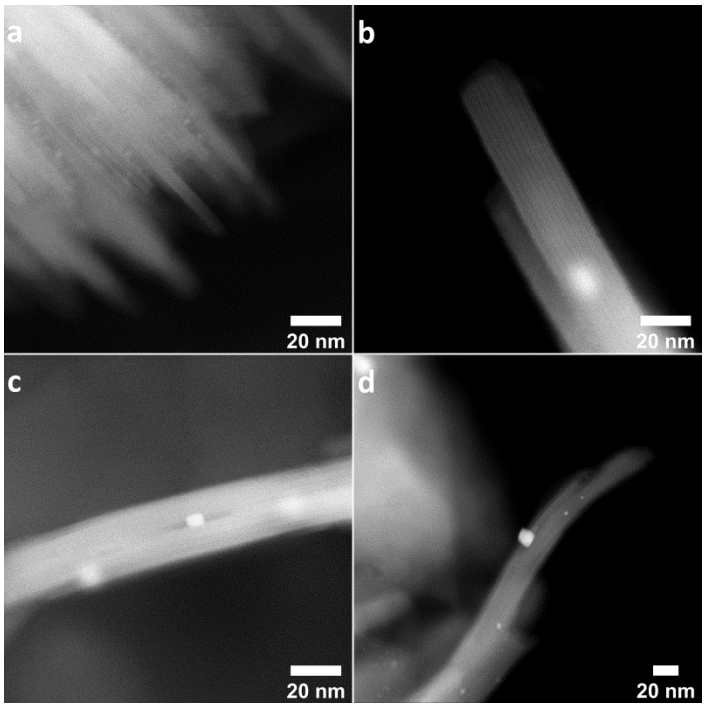

Figure 4.2.10 STEM images of MCM-22P-C_nOH: n = 12 (a), n = 14 (b), n = 16 (c), n = 18 (d).

In conclusion, Pt@MCM-22 samples with tunable Pt nanoparticles size were synthesized using different length of surfactants for swelling of layered MCM-22P with the addition of Pt species. The interlayer distance of swollen samples expanded with the length of surfactants from 1.06 nm (C_{12}OH), 1.56 nm (C_{14}OH), 2.59 nm (C_{16}OH) to 2.89 nm (C_{18}OH). Subsequent calcination of MCM-22-C_nOH-Pt (n = 12, 14, 16, 18) provided samples with similar textural properties and Pt loading despite the initial interlayer distances. The difference of synthesized samples was the size of Pt nanoparticles. The average size of Pt nanoparticles varied from 0.85 nm in MCM-22-C_{12}OH-Pt, 1.00 nm in MCM-22-C_{14}OH-Pt, 1.55 nm in MCM-

22-C_{16}OH-Pt to 2.04 nm in MCM-22-C_{16}OH-Pt. The average diameter of Pt nanoparticles was related to the dimension of surfactants used for the swelling process.

4.2.2 Encapsulation of Pd nanoparticles into MCM-22 by 2D to 3D zeolite transformation approach

4.2.2.1 Synthesis and characterization of Pd@MCM-22

Encapsulation of Pd nanoparticles into the pore systems of zeolite can be achieved by 2D to 3D zeolite transformation approach, which has been described for Pt nanoparticles [59,85,144]. For Pd nanoparticles in MCM-22 zeolite, we chose $Pd(en)_2(Ac)_2$ as the metal precursor. In this chapter, Pd nanoparticles were encapsulated into MCM-22 zeolite during the swelling process in the presence of $Pd(en)_2(Ac)_2$, followed by aggregating Pd nanoparticles during the condensation process, as shown in Figure 4.2.11.

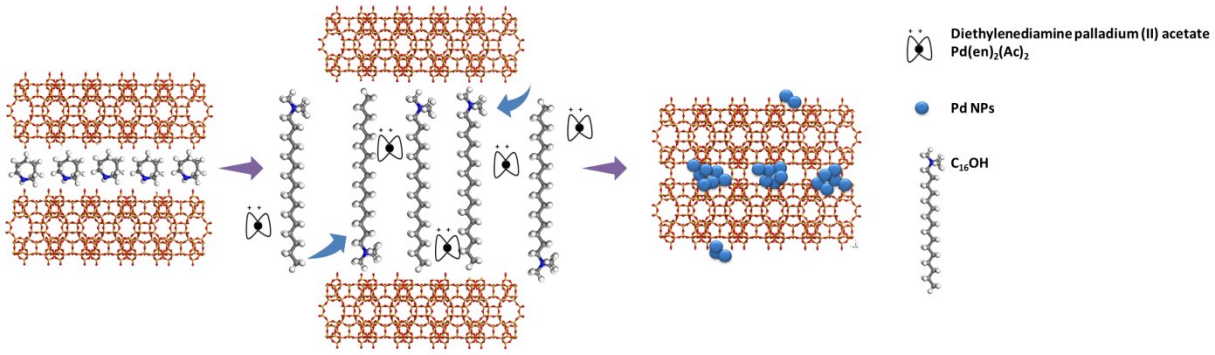

Figure 4.2.11 The synthesis procedure of Pd@MCM-22. During the swelling process of MCM-22P, a solution containing $Pd(en)_2(Ac)_2$ were added. The layers were expanded by the surfactant (C_{16}OH) and $Pd(en)_2(Ac)_2$ were also incorporated into the interlayer space. Removing the organic species caused the formation of Pd@MCM-22.

Figure 4.2.12 shows the XRD patterns of the MCM-22P precursor, MCM-22, Pd@MCM-22PSW and Pd@MCM-22. Swelling treatment with MCM-22P by addition of C_{16}OH and $Pd(en)_2(Ac)_2$ caused the change of interlayer (002) peak to low angle (2θ = 1.8°), the overlapping of (101) and (102) reflection peaks, as well as creating a broad band between 8 and 10° [24,145,146]. These results indicated the presence of C_{16}OH between individual **MWW** layers. After calcination and reduction, the C_{16}OH, SDA (HMI), and $NH_2CH_2CH_2NH_2$ were removed, while the Pd species formed stable nanoparticles encapsulated in MCM-22 zeolite. The intensity of the XRD pattern of Pd@MCM-22 decreased compared to MCM-22, probably caused by the limited dissolution of zeolite precursor under alkaline conditions and not full

condensation of silanols groups due to the formation of large Pd nanoparticles. Figure 4.2.13 shows the SEM images of MCM-22P, MCM-22, Pd@MCM-22PSW and Pd@MCM-22. MCM-22P and MCM-22 samples possess a similar morphology. However, some parts of the Pd@MCM-22PSW and Pd@MCM-22 displayed the aggregation of crystals, probably caused by the basic treatment in the swelling process. Moreover, the EDS spectrum (Figure 4.2.13f) of Pd@MCM-22 confirmed the presence of Pd element in the sample.

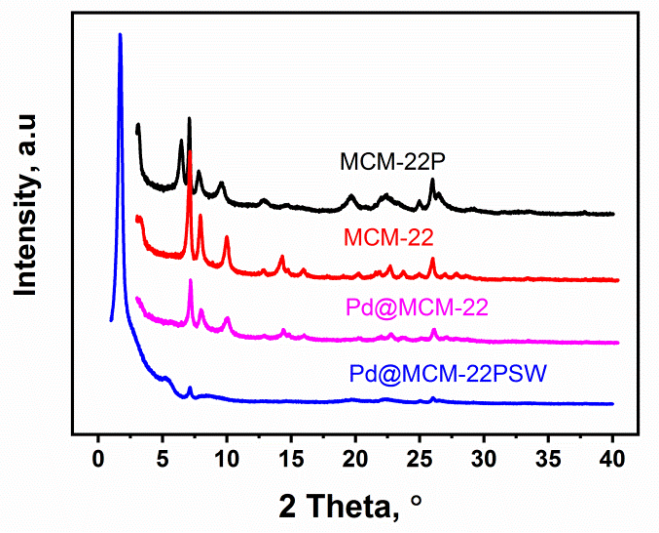

Figure 4.2.12 XRD patterns of MCM-22P, MCM-22, Pd@MCM-22PSW, and Pd@MCM-22.

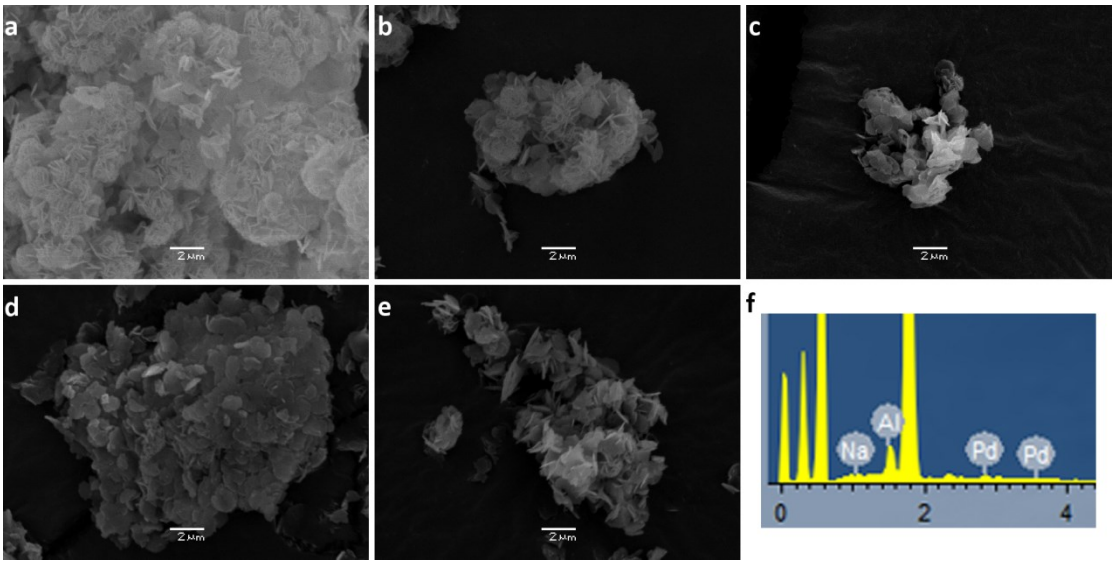

Figure 4.2.13 SEM images of MCM-22P (a), MCM-22 (b), Pd@MCM-22PSW (c), and Pd@MCM-22 (d,e), EDS spectrum of Pd@MCM-22 (f).

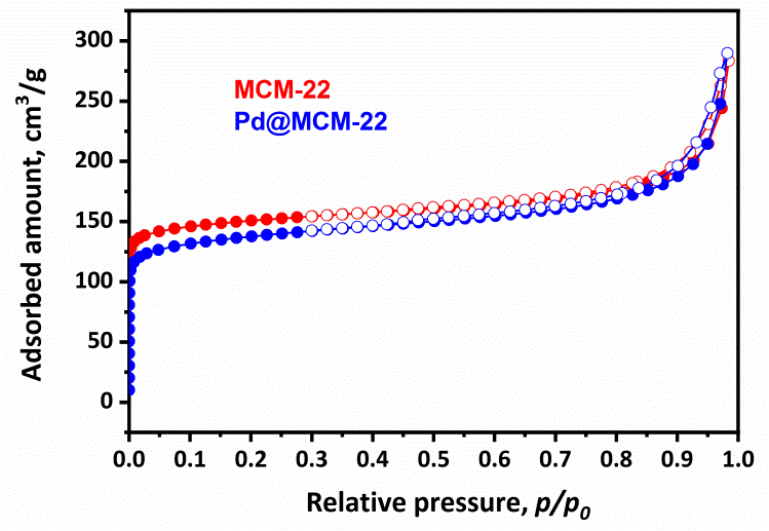

Figure 4.2.14 Nitrogen adsorption (●) and desorption (○) isotherms of MCM-22 and Pd@MCM-22.

Table 4.2.4 Textural parameters, Pd content of MCM-22 and Pd@MCM-22.

	S_{BET} $m^2 g^{-1}$	S_{ext} $m^2 g^{-1}$	V_{mic} $cm^3 g^{-1}$	V_{tot} $cm^3 g^{-1}$	Pd content wt%
MCM-22	536	63	0.21	0.44	0
Pd@MCM-22	490	78	0.18	0.45	0.79

MCM-22 and Pd@MCM-22 exhibited similar textural properties based on the N_2 sorption isotherms (Figure 4.2.14). According to the IUPAC classification, MCM-22 and Pd@MCM-22 showed type I(a) isotherms characteristic of microporous solids [133]. The textural parameters of MCM-22 and Pd@MCM-22 were summarized in Table 4.2.4. Both samples possessed nearly the same BET area (536 and 490 $m^2 g^{-1}$) and micropore volume (0.21 and 0.18 $cm^3 g^{-1}$). Slightly lower micropore volume of Pd@MCM-22 is probably caused by the Pd nanoparticles located in zeolite pores and channels. The palladium content of the Pd@MCM-22 catalyst was measured by ICP-OES with 0.79 wt%.

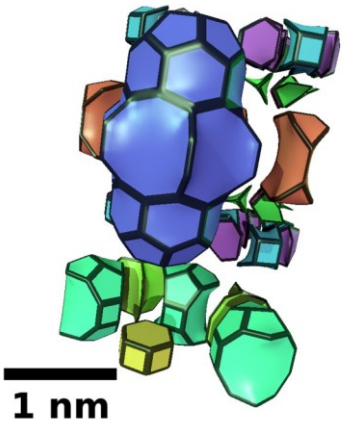

Figure 4.2.15 **MWW** zeolite natural tiles (NBUs).

The size of Pd nanoparticles was determined by the TEM and STEM measurements. The black round spots were Pd nanoparticles in TEM images (Figure 4.2.16), while the white spots were Pd nanoparticles in STEM images (Figure 4.2.17). The TEM and STEM images showed the well-dispersed and uniformly distributed Pd nanoparticles on MCM-22 zeolite crystals. The average diameter of Pd nanoparticles confined in MCM-22 zeolite was ~ 1.8 nm, which was larger than the internal cavities and pore diameter of MCM-22. The natural tiling of **MWW** presents the size of building units (NBUs) with a scale bar can be utilized for size indication, as shown in Figure 4.2.15. The Pd nanoparticles with 1.8 nm size can be located at the defective cavities caused by the insufficient condensation of MCM-22P layers.

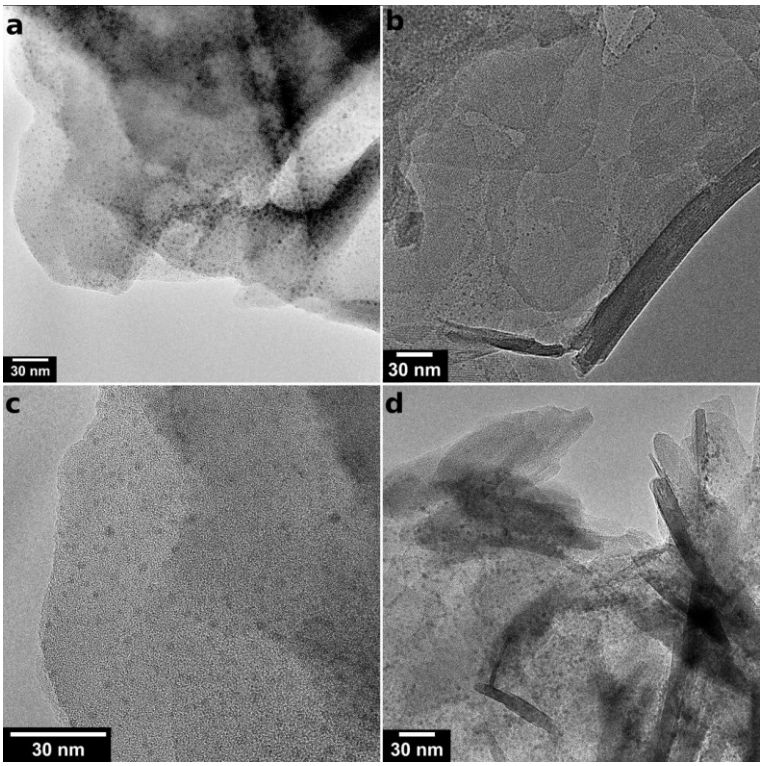

Figure 4.2.16 TEM images of Pd@MCM-22.

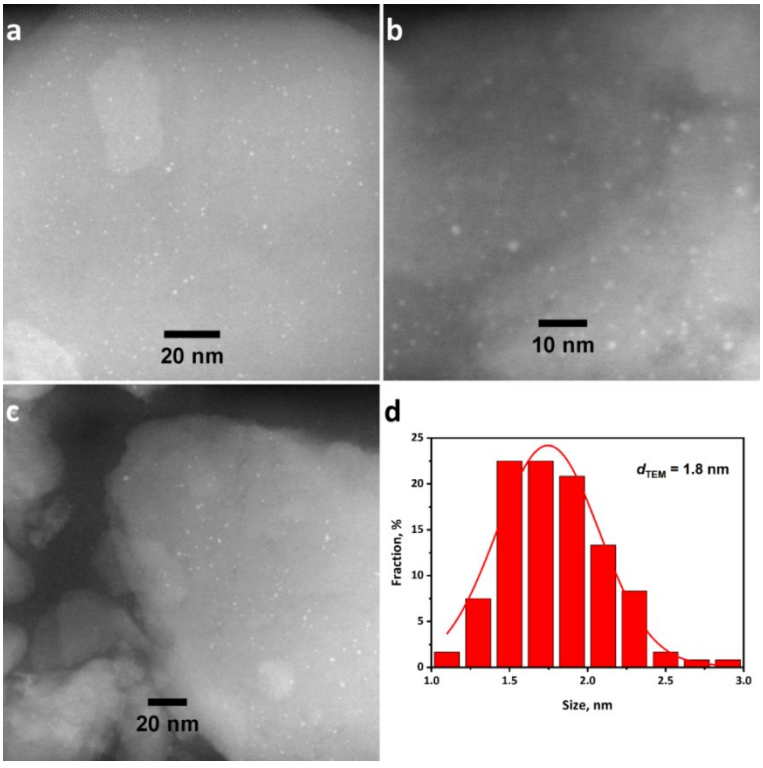

Figure 4.2.17 STEM images (a-c) and Pd nanoparticles size distribution (d) of Pd@MCM-22.

The investigation of the surface hydroxyl groups in MCM-22 and Pd@MCM-22 by FTIR measurement also confirmed the incomplete condensation of silanol groups in the presence

of the Pd nanoparticles (Figure 4.2.18). In the 3800-3200 cm^{-1} region, MCM-22 and Pd@MCM-22 showed the absorption bands of bridging ≡Si-(OH)-Al≡ (3625 cm^{-1}) and external silanol (3651 cm^{-1}) [147,148]. Moreover, Pd@MCM-22 showed an extra absorption peak at a lower frequency (3735 cm^{-1}) than that of free silanols, which was probably assigned to the feature of the defective structure [149,150].

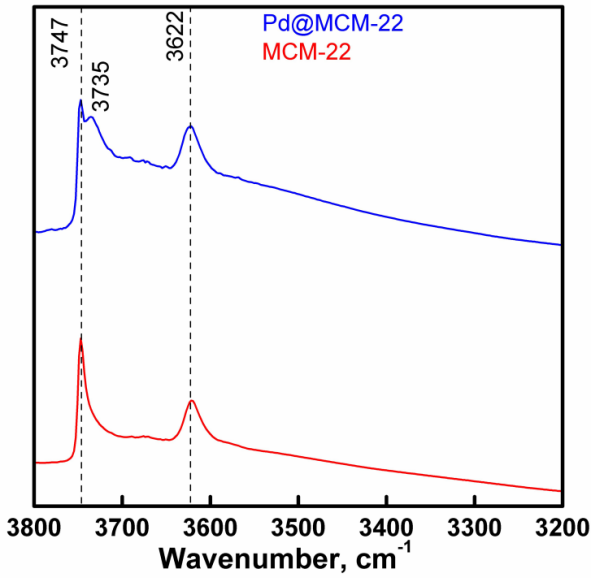

Figure 4.2.18 FTIR spectra of MCM-22 and Pd@MCM-22 in the region of hydroxyl vibrations.

The chemical state of Pd nanoparticles in Pd@MCM-22 was examined using FTIR spectroscopy of adsorbed CO. CO adsorption on unreduced Pd@MCM-22 and reduced Pd@MCM-22 induced various bands in the region of 2300–2000 cm^{-1} (Figure 4.2.19). Both spectra exhibited a band at ~2140 cm^{-1}, which can be ascribed as physical adsorption of CO [151]. The adsorption of CO on Lewis acid sites resulted in a band at 2225 cm^{-1}. The FTIR spectra exhibited bands at 2180, 2160, 2138, 2124 cm^{-1} on both unreduced and reduced Pd@MCM-22, which can be attributed to surface carbonyls of oxidized Pd^{n+} [151]. The band in the region of 2000 – 2120 cm^{-1} indicated the presence of linear Pd^{0}(CO) carbonyls. The bands at 2180 and 2160 cm^{-1} were referred as linear Pd^{2+}-CO complexes, which were easily removed upon outgassing at T < 150 °C. Linear Pd^{+}-CO carbonyls were identified by bands at 2138 and 2124 cm^{-1}, which were maintained upon outgassing at T = 150 °C. These results confirmed that the linear Pd^{+}-CO carbonyls were more stable than the carbonyls of Pd^{2+} due to the synergetic effect of its δ and π components [151]. CO adsorption on unreduced Pd@MCM-22 sample was always followed by the reduction of Pd^{n+} to Pd^{0}, which can be

confirmed by the presence of bands lower 2100 cm^{-1}. Moreover, the FTIR spectrum of CO adsorption of reduced Pd@MCM-22 catalyst displayed a higher absorbance compared with unreduced Pd@MCM-22, indicating the improved accessibility of Pd nanoparticles. Furthermore, the FTIR spectrum of reduced Pd@MCM-22 exhibit a supplementary band at 2076 cm^{-1}, indicating that the reduction under hydrogen form the Pd^0 sites.

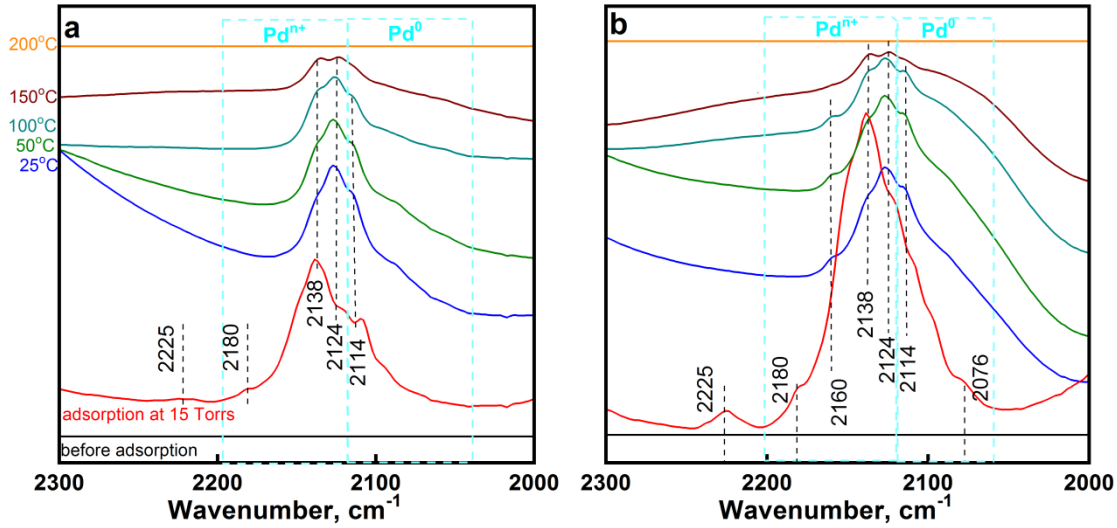

Figure 4.2.19 FTIR spectra of CO adsorbed on unreduced Pd@MCM-22 (a) and reduced Pd@MCM-22 (b).

4.2.2.2 Hydrogenation of nitroarenes over Pd@MCM-22

Aromatic amines are valuable intermediates in the synthesis of fine chemicals, which can be synthesized by reducing nitro group [152-156]. Hydrogenation of nitroarenes is an essential process due to the atomic efficiency and environmental friendliness. Based on this, nitroarenes hydrogenation was chosen as a model reaction to study the catalytic activity of Pd@MCM-22. In Pd@MCM-22 catalyst, most of Pd nanoparticles were encapsulated in zeolite. Thus, the shape-selectivity of MCM-22 can be referred to the characteristics of Pd@MCM-22 catalyst [25]. Therefore, nitroarenes with different size were chosen as reactants to investigate the shape-selective hydrogenation property.

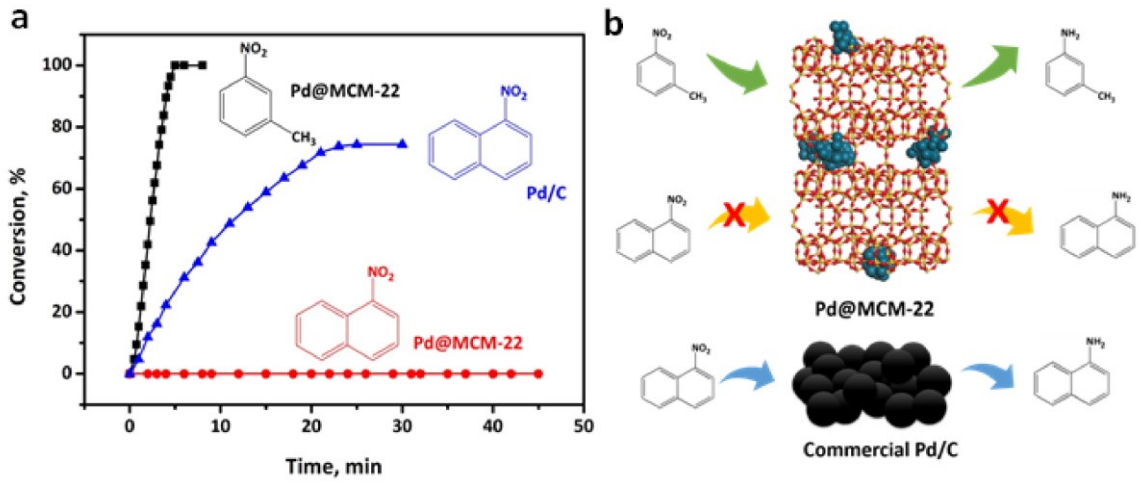

Figure 4.2.20 Hydrogenation of 3-nitrotoluene and 1-nitronaphthalene over Pd@MCM-22 and commercial Pd/C (a), the scheme of the shape-selectivity over Pd@MCM-22 and commercial Pd/C catalysts (b).

3-nitrotoluene (kinetic diameter 0.62 × 0.54 nm) can diffuse in MCM-22 zeolite and be hydrogenated to *m*-toluidine over encapsulated Pd nanoparticles. Hence, the Pd@MCM-22 catalyst exhibited near 100% conversion (Figure 4.2.20). Under the reaction conditions, the TOF over Pd@MCM-22 reached to 5760 h^{-1}. In contrast, the size of 1-nitronaphthalene (0.73 × 0.66 nm) is larger than the pore size of MCM-22 zeolite, thus this bulky molecule cannot diffuse into zeolite framework to interact with Pd nanoparticles. As a result, there was no conversion of 1-nitronaphthalene on Pd@MCM-22 catalyst (Figure 4.2.20). In contrast, the conversion of 1-nitronaphthalene over commercial Pd/C catalyst reached 74.4% conversion. The Pd nanoparticles were located on the surface in Pd/C catalyst, thus 1-nitronaphthalene can easily reach the Pd active sites. The summary of hydrogenation of 3-nitrotoluene and 1-nitronaphthalene over Pd@MCM-22 and commercial Pd/C catalysts were listed in Table 4.2.5. These results further confirmed majority of Pd nanoparticles were confined in MCM-22 zeolite. Moreover, after 3-nitrotoluene hydrogenation, the size of Pd nanoparticles in spent catalyst was maintained (Figure 4.2.21), which additionally proved that Pd nanoparticles confined within MCM-22 zeolite possessed high stability.

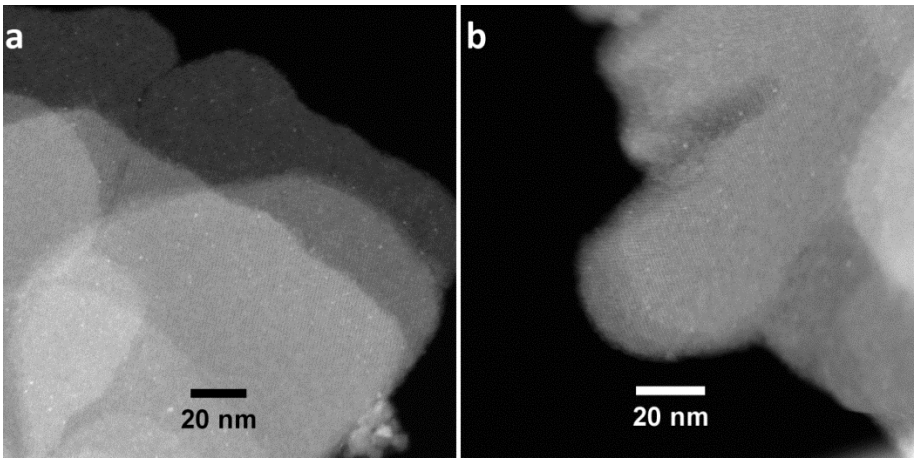

Figure 4.2.21 STEM images of the spent Pd@MCM-22catalyst.

Table 4.2.5 Hydrogenation of 3-nitrotoluene and 1-nitronaphthalene over Pd@MCM-22 and commercial Pd/C with Pd loading at 10 wt%, reaction conditions: T = 100 °C; 0.3 MPa hydrogen pressure; 5 mL of *n*-octane; 1.5 mmol of nitroarenes.

Substrates	Catalysts	Max Conversion (%)	Yield (%)	Selectivity (%)
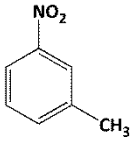	Pd@MCM-22 (50 mg)[1]	>99 (5 min)[2]	>99	>99
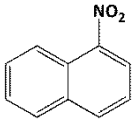	Pd@MCM-22 (50 mg)[1]	0	--	--
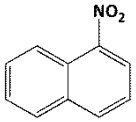	Pd/C (5 mg)[1]	74.4 (25 min)[2]	74	>99

[1] mass of the catalysts;
[2] times after maximum conversion was reached;

In conclusion, Pd@MCM-22 catalyst was synthesized through a 2D to 3D zeolite transformation approach. The $Pd(en)_2(Ac)_2$ were placed into the zeolite interlayer distance when the interlayer was expanded by surfactant ($C_{16}OH$). Consecutively, Pd nanoparticles were encapsulated into MCM-22 zeolite when silanol groups condensed during the calcination process. The average size of Pd nanoparticles is approximately 1.8 nm in the final product. The Pd@MCM-22 exhibited attractive shape-selective hydrogenation of nitroarenes.

4.2.3 Encapsulation of Pt and Pd nanoparticles into IPC zeolites by means of 2D to 3D zeolite transformation strategy and ADOR approach

4.2.3.1 ADOR

The synthesis of 3D germanosilicate **UTL** zeolite is the first step of the ADOR approach. The parent **UTL** zeolite can be converted to lamellar precursor IPC-1P *via* hydrolysis in neutral or acid medium. Modification of IPC-1P layers can produce new 3D zeolites, *e.g.,* IPC-2 (**OKO** topology) and IPC-4 (**PCR** topology) [38]. The stabilization of IPC-1P with diethoxydimethylsilane led to IPC-2. The silanol groups on the layers surface react with the silane, thus condense into new single-four-rings (S4Rs) [38]. Then, the intercalation of various amines or ammonium salts between the layers facilitates the organization of the IPC-1P layers in the most suitable position. The subsequent calcination step condenses the layers, leading to IPC-4 [38]. Encapsulation of metal nanoparticles into zeolite by the 2D to 3D zeolite transformation method can be expanded to IPC-1P layered precursor.

4.2.3.2 Characterization of parent UTL and IPC-1P

The XRD patterns of parent **UTL** and IPC-1P samples (Figure 4.2.22) indicated a high phase purity and crystallinity. XRD pattern of **UTL** has the most intensive (200) reflection at ∼6.2° 2θ, indicating the *d*-spacing of the layers ∼1.42 nm [43]. The stability of Ge-O bond is lower than Si-O bond. After hydrolysis of parent **UTL** in 0.1 M HCl at 95 °C, 2D zeolite precursor - IPC-1P was obtained. The transformation process of parent **UTL** to IPC-1P was proved by the XRD patterns. After removal of the D4R units from parent **UTL**, most of the diffraction lines vanished. The most intensive peak was ascribed to the interlayer diffraction. From the transformation of parent **UTL** to IPC-1P, the dominant peak shifted to 2θ = 8.3°, indicating the *d*-spacing of the layers ∼1.06 nm. The interlayer diffraction changed from lower angle to higher angle, which demonstrated the decreasing of interlayer distance [37]. The **UTL** zeolite showed a rectangular morphology with plate-like crystals in the range of 20 to 60 μm in size, as shown in SEM images (Figure 4.2.23). After hydrolysis of parent **UTL** to IPC-1P, no obviously changes were observed.

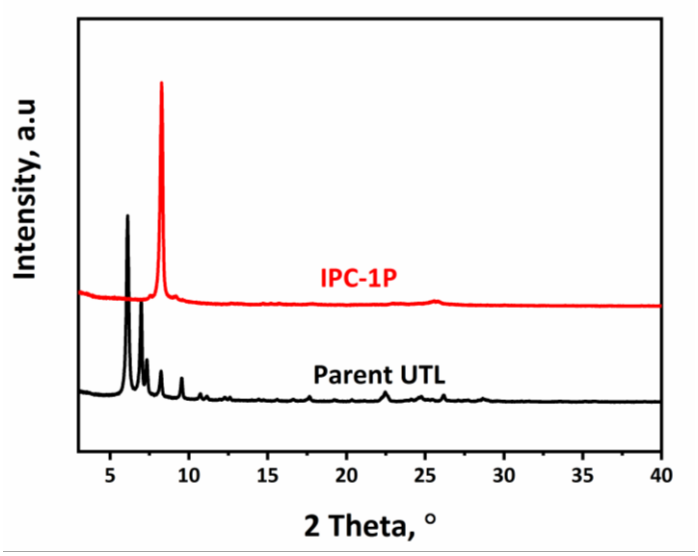

Figure 4.2.22 The XRD patterns of Parent UTL and IPC-1P.

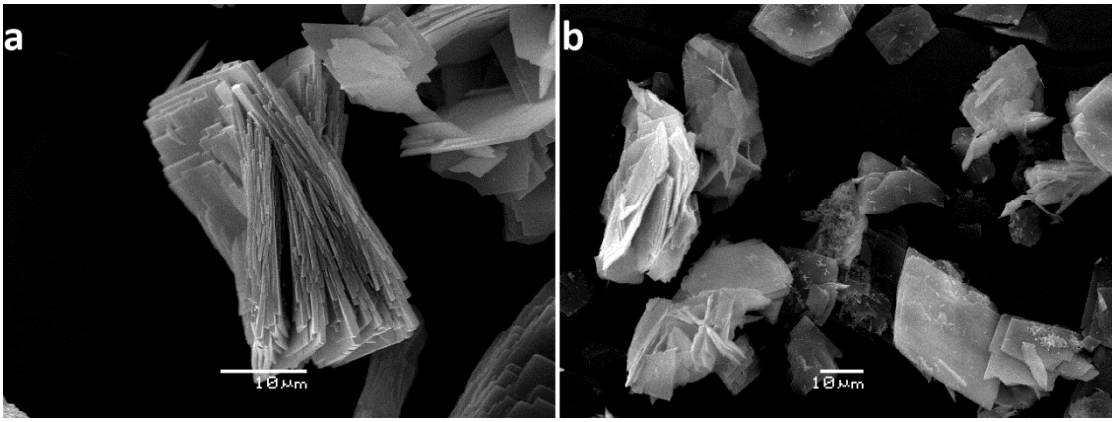

Figure 4.2.23 SEM images of parent **UTL** (a) and IPC-1P (b).

4.2.3.3 Synthesis and characterization of metal@IPC (metal = Pt or Pd)

Introduction of metal species into IPC zeolites started from the 2D lamellar precursor - IPC-1P. For Pt@IPC-2, siloxane complexed with Pt precursors (platinum(0)-2,4,6,8-tetramethyl-2,4,6,8-tetravinylcyclotetrasiloxane) were added during the stabilization procedure, then calcination procedure removed the organics and formed Pt nanoparticles. Synthesis of Pt@IPC-4 was achieved by swelling of IPC-1P with $C_{12}OH$ swelling agent and Pt-DMF solution. The condensation of silanols and elimination of organics were attained by calcination, which also encapsulated Pt nanoparticles into IPC-4 zeolite. The synthesis of Pt@IPC-4 was based on the same procedure as for Pt@MCM-22. In order to decrease the interlayer space and make sure the proper condensation of silanols groups, $C_{12}OH$ surfactant was employed. Pd@IPC-4 catalyst was synthesized by substituting the organization agent - octylamine to

$Pd(en)_2(Ac)_2$ followed by calcination in air to remove the organics and condensation the silanol groups. After introduction of $Pd(en)_2(Ac)_2$ into IPC-1P, stabilization with $Si(CH_3)_2(OCH_2CH_3)_2$ was utilized to form IPC-2 structure with Pd nanoparticles.

Figure 4.2.24 shows the XRD patterns of IPC-2, IPC-4 and metal@IPC-2, metal@IPC-4 (metal = Pt or Pd). The XRD patterns of metal@IPC-2 and metal@IPC-4 matched well with the XRD pattern of IPC-2 and IPC-4, which confirmed that both structures kept the integrity after introducing metal. The dominant peak (200) exhibited high relative intensity, caused by the preferred orientation of crystals [37]. For IPC-2 and metal@IPC-2 samples, the interlayer reflection peak was shifted to higher angle ~7.6° 2θ compared with parent **UTL** (~6.2° 2θ). The D4R units in UTL are replaced by single-four ring (S4R) units in IPC-2. The siloxane reagent condensed between the silica layers and formed the S4R units, while the metal sources inserted into the interlayers and formed the metal nanoparticles. The reflection peak (200) located at 9.7° 2θ was the characteristic of IPC-4 material. The intensity of XRD patterns of Pt@IPC-4 and Pd@IPC-4 were slightly decreased compared with IPC-4, which probably caused by the basic treatment of $C_{12}OH$ surfactant solution and $Pd(en)_2(Ac)_2$ agent during the preparation process.

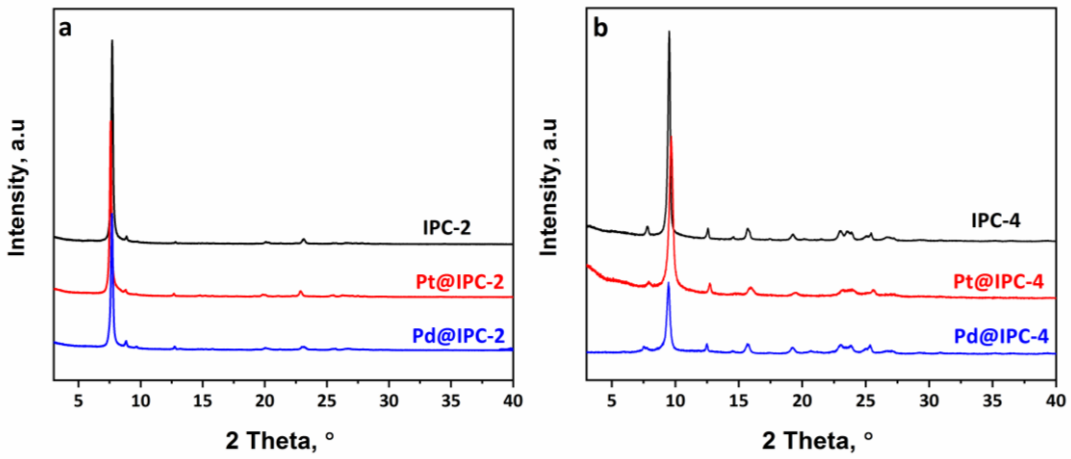

Figure 4.2.24 The XRD patterns of IPC-2, metal@IPC-2 (a) and IPC-4, metal@IPC-4 (b).

The textural parameters of IPC and metal@IPC materials are shown in Table 4.2.6. All the samples showed type I isotherm typically for microporous materials according to IUPAC classification [133]. The differences in the BET areas and micropore volumes agree with different channel systems in IPC-2 and IPC-4 zeolites [157,158]. The BET areas of IPC-2 and metal@IPC-2 are ~350 $m^2 g^{-1}$ and micropore volumes are 0.12~0.15 $cm^3 g^{-1}$, while the BET

area of IPC-4 and metal@IPC-4 are ~240 $m^2 g^{-1}$ and micropore volumes are 0.08~0.11 $cm^3 g^{-1}$. As a result, the confinement of metal nanoparticles (metal = Pt or Pd) into IPC-2 and IPC-4 framework has no significant effect on the textural properties.

Table 4.2.6 Textural parameters and the metal loading of metal@IPC samples.

	S_{BET} $m^2 g^{-1}$	V_{mic} $cm^3 g^{-1}$	V_{tot} $cm^3 g^{-1}$	Pt/Pd loading wt%
Pt@IPC-2	374	0.15	0.23	0.34
Pt@IPC-4	259	0.11	0.14	0.32
Pd@IPC-2	319	0.12	0.19	0.61
Pd@IPC-4	190	0.08	0.11	0.63
IPC-2	334	0.15	0.20	0
IPC-4	236	0.11	0.12	0

The content of Pt was 0.34 wt% in Pt@IPC-2 sample (Table 4.2.6). Moreover, the Pt@IPC-2 maintained the crystal shape and size without significant changes, as shown in the SEM image (Figure 4.2.25a). The ICP-OES analysis showed the Pt loading in Pt@IPC-4 was 0.32 wt%. The SEM image of Pt@IPC-4 exhibited small aggregates probably caused by the basic condition treatment during the swelling process (Figure 4.2.26a). The integrity of Pt@IPC-4 was slightly decreased, which also confirmed by the slightly less intense and wider peaks in the XRD pattern compared with IPC-4.

STEM images of Pt@IPC-2 and Pt@IPC-4 (Figure 4.2.25 and 4.2.26) showed the homogeneously dispersed Pt nanoparticles on IPC-2 and IPC-4 zeolite matrixes. The small size of Pt nanoparticles can be observed in the pore systems of IPC-2 and IPC-4 zeolites as well as on the external surface of crystals. The size distribution of Pt nanoparticles in Pt@IPC-2 and Pt@IPC-4 was assessed by STEM measurement. The average diameters of Pt nanoparticles in Pt@IPC-2 and Pt@IPC-4 samples were around 0.98 nm and 0.96 nm, respectively. The pore sizes of IPC-2 and IPC-4 zeolites are 0.70 × 0.56 nm, 0.61 × 0.47 nm and 0.61 × 0.51 nm, 0.47 × 0.35 nm, respectively. Clearly, the average diameters of Pt nanoparticles were larger the pore sizes of IPC-2 and IPC-4 zeolites. Pt nanoparticles probably created some defects in both Pt@IPC-2 and Pt@IPC-4 samples. In Pt@IPC-2, Pt nanoparticles probably were placed in the interlayer space, which prevented the formation

of S4R units in their close vicinity. Moreover, the particle size distribution exhibited a significant difference for Pt@IPC-2 and Pt@IPC-4 samples. Figure 4.2.25 shows a broad maximum in particle sizes between 0.8-1.2 nm, which can be presumably attributed to the larger pores of IPC-2 (12-10 rings). For Pt@IPC-4 with smaller pore size, this maximum was much sharper with lower distribution of Pt nanoparticles in the range of 0.8-0.9 and 1.0-1.2 nm.

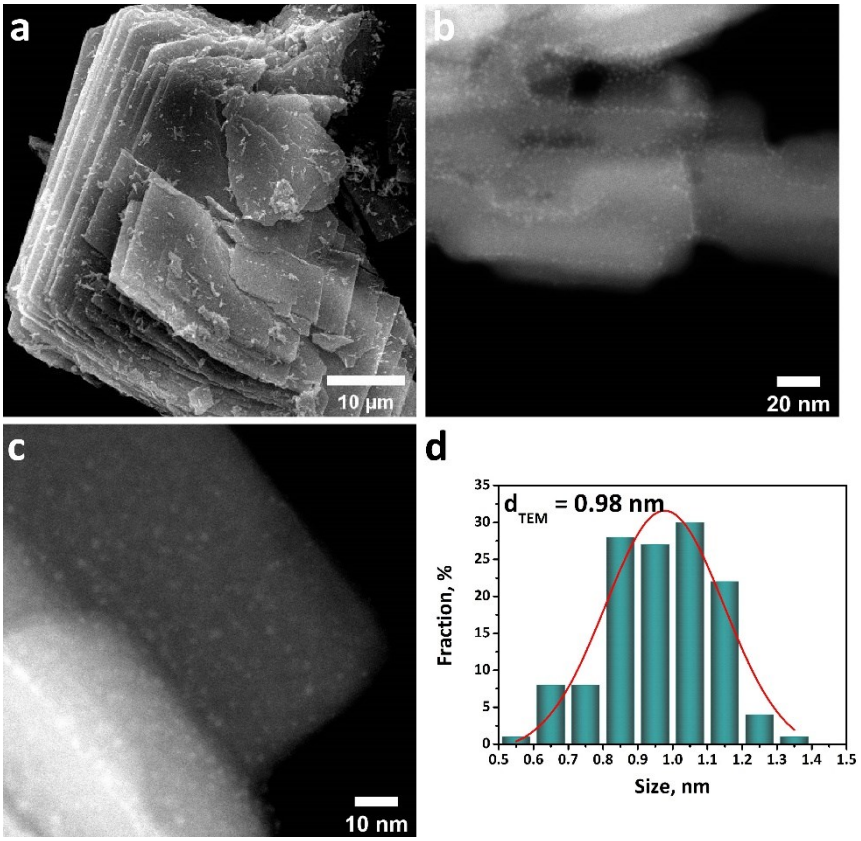

Figure 4.2.25 SEM image (a), STEM images (b-c) and particle size distribution (d) of Pt@IPC-2.

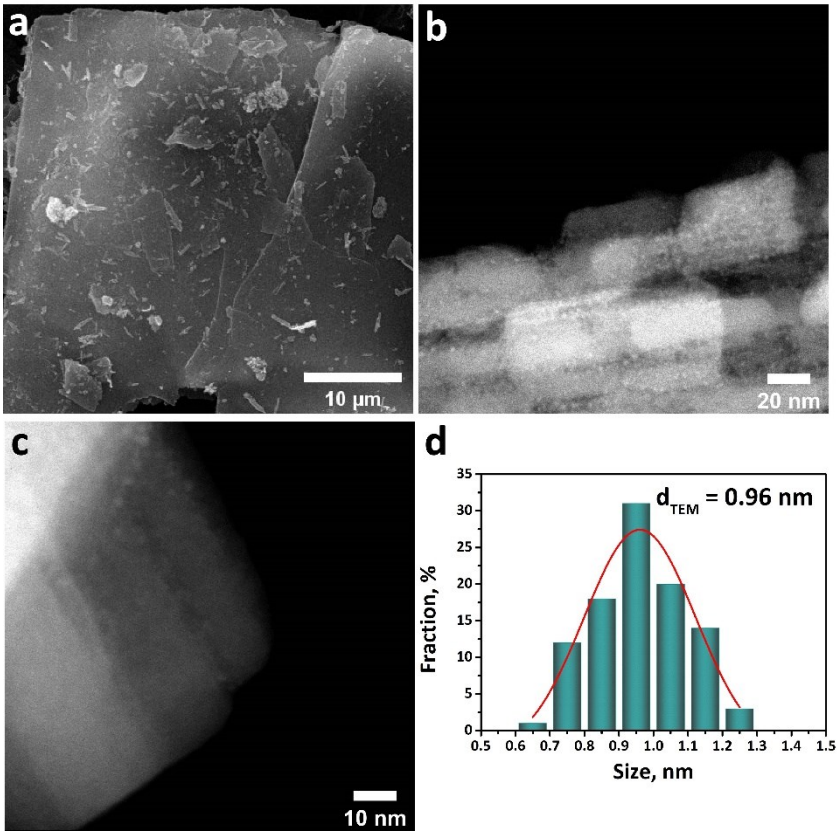

Figure 4.2.26 SEM image (a), STEM images (b-c) and particle size distribution (d) of Pt@IPC-4.

In the case of Pd@IPC-2 and Pd@IPC-4, as shown in EDS maps, Pd nanoparticles were also distributed on the whole zeolite crystals (Figures 4.2.27 and 4.2.28). However, the average diameters of Pd nanoparticles were larger than Pt@IPC samples. The average diameters of Pd nanoparticles in Pd@IPC-2 and Pd@IPC-4 catalysts were centered on 2.4 nm (Pd@IPC-2) and 1.7 nm (Pd@IPC-4), respectively. In general, Pd nanoparticles were confined in zeolite IPC-2 and IPC-4 zeolites causing some defects, as well as some of the Pd nanoparticles were situated on the outer surface of IPC zeolite crystals.

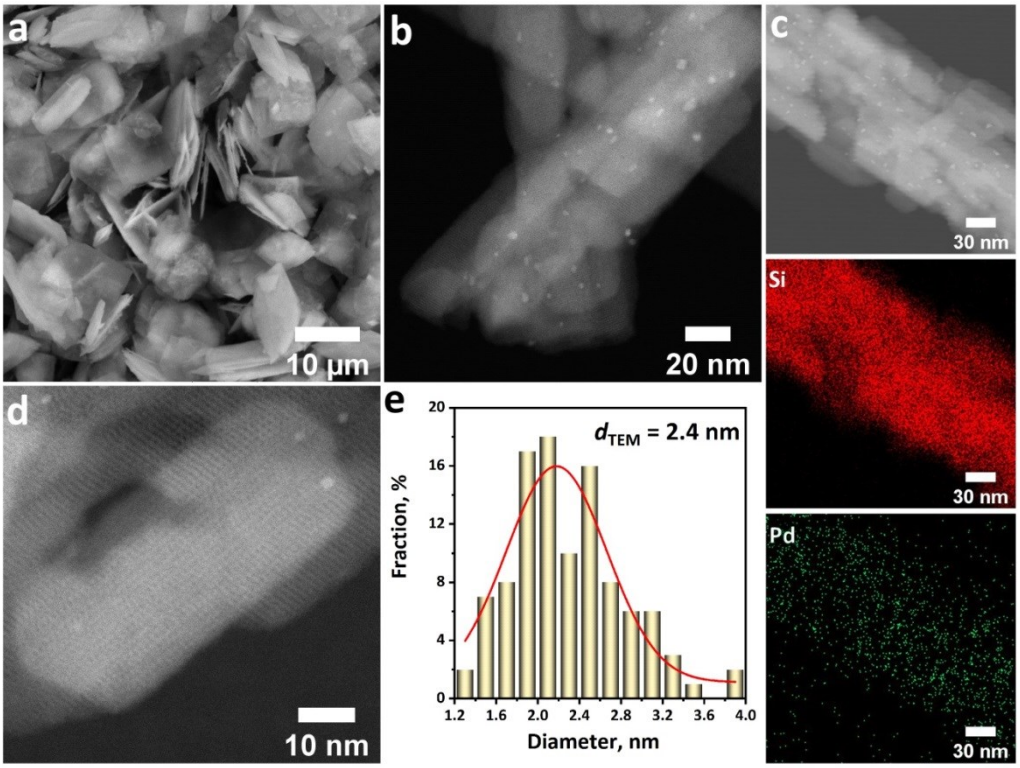

Figure 4.2.27 SEM image (a), STEM images (b,d), size distribution (e) and EDS maps of Si, Pd elements (c) of Pd@IPC-2.

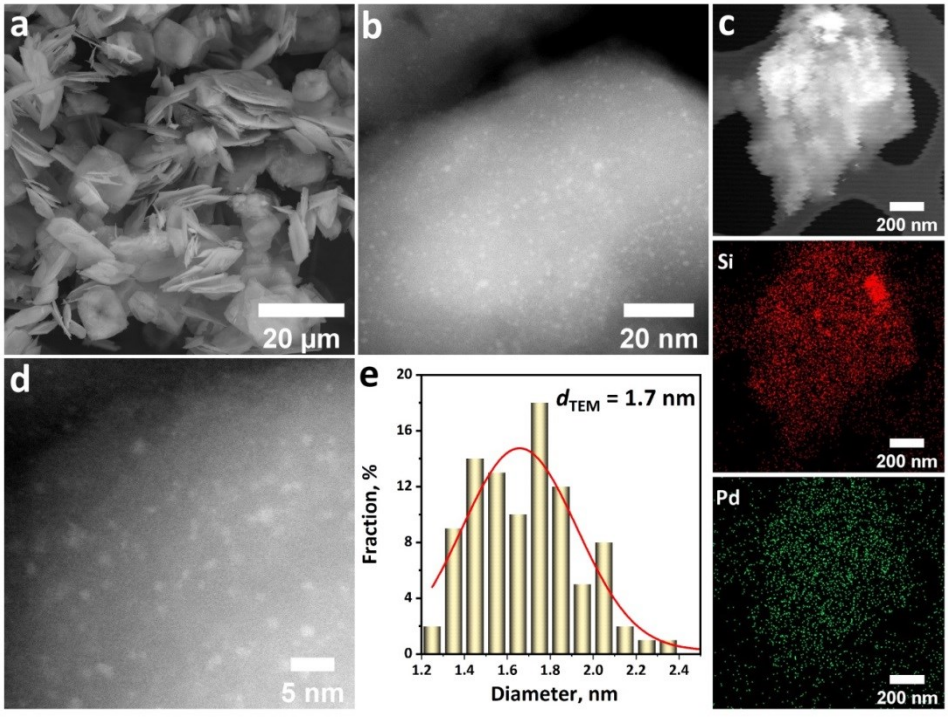

Figure 4.2.28 SEM image (a), STEM images (b,d), size distribution (e) and EDS maps of Si, Pd elements (c) of Pd@IPC-4.

4.2.3.4 The catalytic performance of Pd@IPC catalysts

Gas-phase hydrogenation of propene was selected as a reaction to evaluate the catalytic performance of Pd@IPC catalysts under mild condition ($C_3H_6/H_2/He$=5/15/80 vol. %; total flow rate: 40.7 mL min^{-1}, atmospheric pressure, room temperature). The diffusion of the reactant propene with a kinetic diameter 0.42 × 0.32 nm and propane with kinetic diameter 0.46 × 0.30 nm should not be significantly restricted in the channels of IPC-2. The hydrogenation of propene to propane (Figure 4.2.29) exhibited the initial reaction rate 6.17 mmol/s/g_{Me}. However, the pore size of IPC-4 (0.47 × 0.35 nm) is comparable with the kinetic diameter of propene and propane. The diffusion of reactant to the metal active sites over Pd@IPC-4 is hindered, exhibiting poor hydrogenating activity at TOS = 25 min (Table 4.2.7). This shape-selectivity phenomenon was further confirmed that most of Pd nanoparticles were confined in IPC-4 zeolite.

Table 4.2.7 Conversion and reaction rate of propene hydrogenation over Pd@IPC-2 and Pd@IPC-4 catalysts.

Catalyst	X*(C_3H_6) (%)	Rate (mmol/s/g_{Me})
Pd@IPC-2	25.3	6.17
Pd@IPC-4	0.0	0.00

* Conversion at TOS = 25 min;

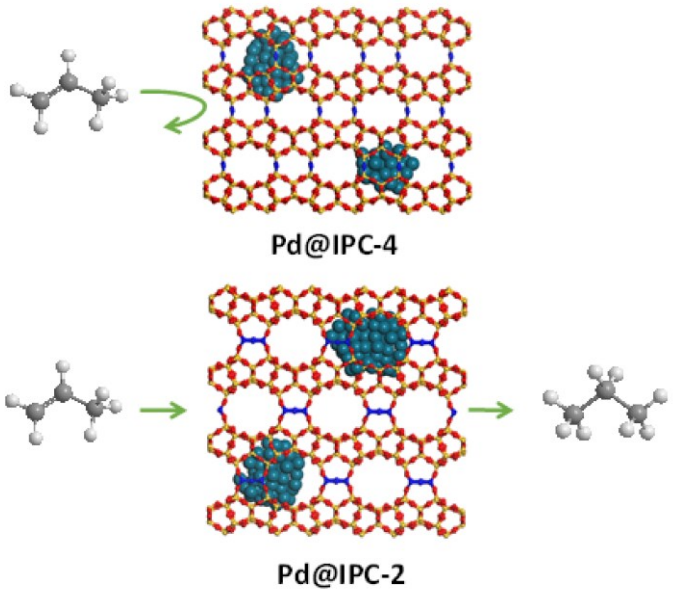

Figure 4.2.29 The model of hydrogenation of propene over Pd@IPC-2 and Pd@IPC-4 catalysts.

In summary, IPC zeolites with tunable textural properties due to the changing of pore structure can be prepared by ADOR strategy. Functionalization of IPC zeolites with Pt and Pd nanoparticles results metal@zeolite catalysts with designable textural properties. The metal@IPC materials (metal = Pt or Pd) exhibited similar textual properties compared with the parent IPC zeolites. The sizes of metal nanoparticles in metal@IPC materials were investigated by STEM measurement. The average sizes of Pt nanoparticles in Pt@IPC-2 and Pt@IPC-4 were 0.98 and 0.96 nm, while the average diameters of Pd nanoparticles were 2.4 and 1.7 nm in Pd@IPC-2 and Pd@IPC-4 samples, respectively. The shape-selective hydrogenation of propene over Pd@IPC-2 and Pd@IPC-4 further confirmed that most of Pd nanoparticles were located in IPC zeolite frameworks. The 2D to 3D zeolite transformation strategy to encapsulate metal nanoparticles into zeolites was successfully expanded to IPC-1P layered precursor. After combination with ADOR approach, metal@IPC-2 and metal@IPC-4 (metal = Pt, Pd) can be prepared.

5. Conclusions and perspectives

Metal nanoparticles encapsulated in zeolite micropores represent an important type of functional materials, which combined the advantages of the metal catalyst itself with those of stable zeolite supports. This thesis was focused on encapsulation of metal nanoparticles into zeolites by co-crystallization strategy and 2D to 3D zeolite transformation approach.

Pt and Pd nanoparticles were encapsulated into **MFI** zeolites by co-crystallization strategy in the presence of imidazolium-type ionic liquid (ImILs). The ImILs can protect the metal precursors against precipitation *via* electrostatic interactions and participate in **MFI** zeolite crystallization. The XRD patterns revealed that the presence of ImILs had no influence on the crystallization of **MFI** zeolite. Moreover, the textural properties of metal@MFI_ImILs maintained the microporous materials character. STEM measurement showed the homogeneous distribution of Pt or Pd nanoparticles on **MFI** zeolite and the average diameters of Pt and Pd nanoparticles were 1.0 and 1.8 nm, respectively. Furthermore, this imidazolium-type ionic liquid-assisted strategy was also successfully in encapsulation of Au nanoparticles with average diameter 1.3 nm into **MFI** zeolite. In addition, the resulting Pt@MFI_ImILs exhibited excellent shape-selectivity in hydrogenation of different size of nitroarenes. 4-nitrotoluene can be hydrogenated effectively, while the bulky 1,3-dimethyl-5-nitrobenzene only showed 5.8% conversion. Pd@MFI_ImILs showed higher activity than the impregnated sample in propene hydrogenation due to the small Pd nanoparticles in **MFI z**eolite. However, this imidazolium-type ionic liquid-assisted formation of metal nanoparticles in zeolite strategy should be expanded to different metals and zeolites to verify the feasibility. Moreover, the application of these catalysts is limited in metal catalysis, metal-acid synergistic catalysis should be employed to investigate the metal/acid distribution.

For the encapsulation strategy *via* 2D to 3D zeolite transformation, the influence of the swelling agents was investigated for the first time. After condensation of the layers, the average sizes of Pt nanoparticles were tuned from 0.85 nm, 1.00 nm, 1.55 nm to 2.04 nm. Subsequently, Pd@MCM-22 catalyst was prepared by using the $Pd(en)_2(Ac)_2$ as metal precursor during the swelling process of MCM-22P. The following calcination procedure condenses the layers and encapsulates Pd nanoparticles into MCM-22 zeolite. Afterwards,

Pd nanoparticles were uniformly distributed on MCM-22 with the average diameter approximately 1.8 nm. The shape-selective hydrogenation of nitroarenes with different sizes further confirmed that most of Pd nanoparticles were trapped in MCM-22 zeolite. Lastly, the 2D to 3D zeolite transformation approach was extended from MCM-22P to IPC-1P precursor. After combining with ADOR approach, metal@IPC-2 and metal@IPC-4 (metal = Pt, Pd) with uniform distribution of metal nanoparticles were synthesized. However, for this new 2D to 3D zeolite transformation strategy, deeply investigation should be performed using more layered representatives and different metal precursors.

My Ph.D studies have mainly focused on the encapsulation of noble metal nanoparticles such as Pt, Pd into conventional zeolites. Compared with noble metals, the non-noble metals are less expensive and exhibit good catalytic activities in some industrial reactions. Some effort needs to put on encapsulation of non-noble nanoparticles into zeolites. In addition, owing to the individual and isolated metal active centers of single metal atom, encapsulation of single metal atoms into zeolites offers a great potential in constructing of cost-effective catalysts. Last but not least, due to the diffusion limitation owing to the existence of zeolite micropores, only the metal active sites on zeolite surface are participated in the reaction, which cause the low catalytic efficiency of encapsulating metal in zeolite catalysts. In order to solve this limitation and expand their utilization, encapsulation of metal species into hierarchical zeolites should be a promising way.

6. References

(1) Čejka, J.; Corma, A.; Zones, S. *Zeolites and Catalysis*; Wiley-VCH, 2010.
(2) Karge, H. G.; Weitkamp, J. *Adsorption and Diffusion*; Springer, 2008.
(3) R. Hull; C. Jagadis; R.M. Osgood; Jr. J. Parisi; Z.Wang; H.Warlimont *Characterization and Design of Zeolite Catalysts*; Springer, 2010.
(4) Smith, J. V. Topochemistry of zeolites and related materials. 1. Topology and geometry. *Chem. Rev.* **1988,** *88*, 149.
(5) Chester, A. W.; Derouane, E. G. *Zeolite Chemistry and Catalysis*; Springer 2009.
(6) Li, Y.; Yu, J. New stories of zeolite structures: their descriptions, determinations, predictions, and evaluations. *Chem. Rev.* **2014,** *114*, 7268.
(7) Roth, W. J.; Nachtigall, P.; Morris, R. E.; Cejka, J. Two-dimensional zeolites: current status and perspectives. *Chem. Rev.* **2014,** *114*, 4807.
(8) Csicsery, S. M. Shape-selective catalysis in zeolites. *Zeolites* **1984,** *4*, 202.
(9) Teketel, S.; Westgård Erichsen, M.; Lønstad Bleken, F.; Svelle, S.; Petter Lillerud, K.; Olsbye, U. *Chapter 6. Shape selectivity in zeolite catalysis. The Methanol to Hydrocarbons (MTH) reaction*; Royal Society of Chemistry, 2014; Vol. 26.
(10) Smit, B.; Maesen, T. L. Towards a molecular understanding of shape selectivity. *Nature* **2008,** *451*, 671.
(11) Csicsery, S. M. Catalysis by shape selective zeolites-science and technology. *Pure Appl. Chem.* **1986,** *58*, 841.
(12) Dusselier, M.; Davis, M. E. Small-Pore Zeolites: Synthesis and Catalysis. *Chem. Rev.* **2018,** *118*, 5265.
(13) Li, J.; Corma, A.; Yu, J. Synthesis of new zeolite structures. *Chem. Soc. Rev.* **2015,** *44*, 7112.
(14) Meng, X.; Xiao, F. S. Green routes for synthesis of zeolites. *Chem. Rev.* **2014,** *114*, 1521.
(15) Cundy, C. S.; Cox, P. A. The hydrothermal synthesis of zeolites: history and development from the earliest days to the present time. *Chem. Rev.* **2003,** *103*, 663.
(16) Prech, J.; Pizarro, P.; Serrano, D. P.; Cejka, J. From 3D to 2D zeolite catalytic materials. *Chem. Soc. Rev.* **2018,** *47*, 8263.
(17) Roth, W. J.; Gil, B.; Makowski, W.; Marszalek, B.; Eliasova, P. Layer like porous materials with hierarchical structure. *Chem. Soc. Rev.* **2016,** *45*, 3400.
(18) Opanasenko, M. V.; Roth, W. J.; Čejka, J. Two-dimensional zeolites in catalysis: current status and perspectives. *Catal. Sci. Technol.* **2016,** *6*, 2467.
(19) Roth, W. J.; Čejka, J. Two-dimensional zeolites: dream or reality? *Catal. Sci. Technol.* **2011,** *1*, 43.
(20) Čejka, J.; Centi, G.; Perez-Pariente, J.; Roth, W. J. Zeolite-based materials for novel catalytic applications: Opportunities, perspectives and open problems. *Catal. Today* **2012,** *179*, 2.
(21) Opanasenko, M.; Parker, W. O., Jr.; Shamzhy, M.; Montanari, E.; Bellettato, M.; Mazur, M.; Millini, R.; Cejka, J. Hierarchical hybrid organic-inorganic materials with tunable textural properties obtained using zeolitic-layered precursor. *J. Am. Chem. Soc.* **2014,** *136*, 2511.
(22) Schwanke, A. J.; Pergher, S.; Díaz, U.; Corma, A. The influence of swelling agents molecular dimensions on lamellar morphology of MWW-type zeolites active for fructose conversion. *Microporous Mesoporous Mater.* **2017,** *254*, 17.
(23) Mazur, M.; Chlubná-Eliášová, P.; Roth, W. J.; Čejka, J. Intercalation chemistry of layered zeolite precursor IPC-1P. *Catal. Today* **2014,** *227*, 37.
(24) Roth, W. J.; Čejka, J.; Millini, R.; Montanari, E.; Gil, B.; Kubu, M. Swelling and Interlayer Chemistry of Layered MWW Zeolites MCM-22 and MCM-56 with High Al Content. *Chem. Mater.* **2015,** *27*, 4620.
(25) Leonowicz, M. E.; Lawton, J. A.; Lawton, S. L.; Rubin, M. K. MCM-22: A Molecular Sieve with Two Independent Multidimensional Channel Systems. *Science* **1994,** *264*, 1910.

(26) Bennett, J. M.; Chang, C. D.; Lawton, S. L.; Leonowicz, M. E.; Lissy, D. N.; Rubin, M. K. Synthetic porous crystalline mcm-49, its synthesis and use. *Mobil Oil Corp.* **1992**.
(27) Roth, W. J. *MCM-22 zeolite family and the delaminated zeolite MCM-56 obtained in one-step synthesis*; Elsevier 2005; Vol. 158.
(28) Roth, W. J.; Kresge, C. T.; Vartuli, J. C.; Leonowicz, M. E.; Fung, A. S.; McCullen, S. B. *MCM-36: The first pillared molecular sieve with zeoliteproperties*; Elsevier, 1995; Vol. 94.
(29) Kubu, M.; Roth, W. J.; Greer, H. F.; Zhou, W.; Morris, R. E.; Prech, J.; Cejka, J. A new family of two-dimensional zeolites prepared from the intermediate layered precursor IPC-3P obtained during the synthesis of TUN zeolite. *Chem. Eur. J.* **2013,** *19*, 13937.
(30) Corma, A.; Fornes, V.; Pergher, S. B.; Maesen, T. L. M.; Buglass, J. G. Delaminated zeolite precursors as selective acidic catalysts. *Nature* **1998,** *396*, 353.
(31) Choi, M.; Na, K.; Kim, J.; Sakamoto, Y.; Terasaki, O.; Ryoo, R. Stable single-unit-cell nanosheets of zeolite MFI as active and long-lived catalysts. *Nature* **2009,** *461*, 246.
(32) Na, K.; Jo, C.; Kim, J.; Cho, K.; Jung, J.; Seo, Y.; Messinger, R. J.; Chmelka, B. F.; Ryoo, R. Directing zeolite structures into hierarchically nanoporous architectures. *Science* **2011,** *333*, 328.
(33) Na, K.; Choi, M.; Park, W.; Sakamoto, Y.; Terasaki, O.; Ryoo, R. Pillared MFI zeolite nanosheets of a single-unit-cell thickness. *J. Am. Chem. Soc.* **2010,** *132*, 4169.
(34) Jung, J.; Jo, C.; Cho, K.; Ryoo, R. Zeolite nanosheet of a single-pore thickness generated by a zeolite-structure-directing surfactant. *J. Mater. Chem.* **2012,** *22*, 4367.
(35) Park, W.; Yu, D.; Na, K.; Jelfs, K. E.; Slater, B.; Sakamoto, Y.; Ryoo, R. Hierarchically Structure-Directing Effect of Multi-Ammonium Surfactants for the Generation of MFI Zeolite Nanosheets. *Chem. Mater.* **2011,** *23*, 5131.
(36) Eliasova, P.; Opanasenko, M.; Wheatley, P. S.; Shamzhy, M.; Mazur, M.; Nachtigall, P.; Roth, W. J.; Morris, R. E.; Cejka, J. The ADOR mechanism for the synthesis of new zeolites. *Chem. Soc. Rev.* **2015,** *44*, 7177.
(37) Roth, W. J.; Shvets, O. V.; Shamzhy, M.; Chlubna, P.; Kubu, M.; Nachtigall, P.; Cejka, J. Postsynthesis transformation of three-dimensional framework into a lamellar zeolite with modifiable architecture. *J. Am. Chem. Soc.* **2011,** *133*, 6130.
(38) Roth, W. J.; Nachtigall, P.; Morris, R. E.; Wheatley, P. S.; Seymour, V. R.; Ashbrook, S. E.; Chlubna, P.; Grajciar, L.; Polozij, M.; Zukal, A.et al. A family of zeolites with controlled pore size prepared using a top-down method. *Nat. Chem.* **2013,** *5*, 628.
(39) Mazur, M.; Wheatley, P. S.; Navarro, M.; Roth, W. J.; Polozij, M.; Mayoral, A.; Eliasova, P.; Nachtigall, P.; Cejka, J.; Morris, R. E. Synthesis of 'unfeasible' zeolites. *Nat. Chem.* **2016,** *8*, 58.
(40) Wheatley, P. S.; Chlubna-Eliasova, P.; Greer, H.; Zhou, W.; Seymour, V. R.; Dawson, D. M.; Ashbrook, S. E.; Pinar, A. B.; McCusker, L. B.; Opanasenko, M.et al. Zeolites with continuously tuneable porosity. *Angew. Chem. Int. Ed.* **2014,** *53*, 13210.
(41) Shvets, O. V.; Zukal, A.; Kasian, N.; Zilkova, N.; Cejka, J. The role of crystallization parameters for the synthesis of germanosilicate with UTL topology. *Chem. Eur. J.* **2008,** *14*, 10134.
(42) Shvets, O. V.; Kasian, N.; Zukal, A. t.; Pinkas, J. i.; Čejka, J. i. The Role of Template Structure and Synergism between Inorganic and Organic Structure Directing Agents in the Synthesis of UTL Zeolite. *Chem. Mater.* **2010,** *22*, 3482.
(43) Shvets, O. V.; Nachtigall, P.; Roth, W. J.; Čejka, J. UTL zeolite and the way beyond. *Microporous Mesoporous Mater.* **2013,** *182*, 229.
(44) Chlubná, P.; Roth, W. J.; Greer, H. F.; Zhou, W.; Shvets, O.; Zukal, A.; Čejka, J.; Morris, R. E. 3D to 2D Routes to Ultrathin and Expanded Zeolitic Materials. *Chem. Mater.* **2013,** *25*, 542.
(45) Zukal, A.; Shamzhy, M.; Kubů, M.; Čejka, J. The effect of pore size dimensions in isoreticular zeolites on carbon dioxide adsorption heats. *J. CO2 Util.* **2018,** *24*, 157.
(46) Mazur, M.; Kubů, M.; Wheatley, P. S.; Eliášová, P. Germanosilicate UTL and its rich chemistry of solid-state transformations towards IPC-2 (OKO) zeolite. *Catal. Today* **2015,** *243*, 23.

(47) Mazur, M.; Arévalo-López, Angel M.; Wheatley, P. S.; Bignami, G. P. M.; Ashbrook, S. E.; Morales-García, Á.; Nachtigall, P.; Attfield, J. P.; Čejka, J.; Morris, R. E. Pressure-induced chemistry for the 2D to 3D transformation of zeolites. *J. Mater. Chem. A* **2018,** *6*, 5255.
(48) Shamzhy, M.; Mazur, M.; Opanasenko, M.; Roth, W. J.; Cejka, J. Swelling and pillaring of the layered precursor IPC-1P: tiny details determine everything. *Dalton Trans.* **2014,** *43*, 10548.
(49) Wu, S. M.; Yang, X. Y.; Janiak, C. Confinement Effects in Zeolite-Confined Noble Metals. *Angew. Chem. Int. Ed.* **2019,** *58*, 12340.
(50) Wang, N.; Sun, Q.; Yu, J. Ultrasmall Metal Nanoparticles Confined within Crystalline Nanoporous Materials: A Fascinating Class of Nanocatalysts. *Adv. Mater.* **2019,** *31*, 1803966.
(51) Wang, L.; Xu, S.; He, S.; Xiao, F.-S. Rational construction of metal nanoparticles fixed in zeolite crystals as highly efficient heterogeneous catalysts. *Nano Today* **2018,** *20*, 74.
(52) Kosinov, N.; Liu, C.; Hensen, E. J. M.; Pidko, E. A. Engineering of Transition Metal Catalysts Confined in Zeolites. *Chem. Mater.* **2018,** *30*, 3177.
(53) Farrusseng, D.; Tuel, A. *Zeolite-Encapsulated Catalysts*; Elsevier, 2017; Vol. 11.
(54) Chai, Y.; Shang, W.; Li, W.; Wu, G.; Dai, W.; Guan, N.; Li, L. Noble Metal Particles Confined in Zeolites: Synthesis, Characterization, and Applications. *Adv. Sci.* **2019,** *6*, 1900299.
(55) Xu, D.; Lv, H.; Liu, B. Encapsulation of Metal Nanoparticle Catalysts Within Mesoporous Zeolites and Their Enhanced Catalytic Performances: A Review. *Front. Chem.* **2018,** *6*, 550.
(56) Farrusseng, D.; Tuel, A. Perspectives on zeolite-encapsulated metal nanoparticles and their applications in catalysis. *New J. Chem* **2016,** *40*, 3933.
(57) Gallezot, P. *Preparation of Metal Clusters in Zeolites*; Springer, 2002; Vol. 3.
(58) Shamzhy, M.; Opanasenko, M.; Concepcion, P.; Martinez, A. New trends in tailoring active sites in zeolite-based catalysts. *Chem. Soc. Rev.* **2019,** *48*, 1095.
(59) Liu, L.; Diaz, U.; Arenal, R.; Agostini, G.; Concepcion, P.; Corma, A. Generation of subnanometric platinum with high stability during transformation of a 2D zeolite into 3D. *Nat. Mater.* **2017,** *16*, 132.
(60) Pala Rosas, I.; Contreras, J.; Salmones, J.; Tapia, C.; Zeifert, B.; Navarrete, J.; Vázquez, T.; García, D. Catalytic Dehydration of Glycerol to Acrolein over a Catalyst of Pd/LaY Zeolite and Comparison with the Chemical Equilibrium. *Catalysts* **2017,** *7*, 73.
(61) Lee, J.; Ryou, Y.; Hwang, S.; Kim, Y.; Cho, S. J.; Lee, H.; Kim, C. H.; Kim, D. H. Comparative study of the mobility of Pd species in SSZ-13 and ZSM-5, and its implication for their activity as passive NOx adsorbers (PNAs) after hydro-thermal aging. *Catal. Sci. Technol.* **2019,** *9*, 163.
(62) Iida, T.; Zanchet, D.; Ohara, K.; Wakihara, T.; Roman-Leshkov, Y. Concerted Bimetallic Nanocluster Synthesis and Encapsulation via Induced Zeolite Framework Demetallation for Shape and Substrate Selective Heterogeneous Catalysis. *Angew. Chem. Int. Ed.* **2018,** *57*, 6454.
(63) Townsend, R. P.; Coker, E. N. *Ion exchange in zeolites*; Elsevier 2001; Vol. 137.
(64) Ryou, Y.; Lee, J.; Lee, H.; Kim, C. H.; Kim, D. H. Effect of various activation conditions on the low temperature NO adsorption performance of Pd/SSZ-13 passive NOx adsorber. *Catal. Today* **2019,** *320*, 175.
(65) Hamid, S.; Kumar, M. A.; Lee, W. Highly reactive and selective Sn-Pd bimetallic catalyst supported by nanocrystalline ZSM-5 for aqueous nitrate reduction. *Appl. Catal. B* **2016,** *187*, 37.
(66) Blomsma, E.; Martens, J. A.; Jacobs, P. A. Mechanisms of Heptane Isomerization on Bifunctional Pd/H-Beta Zeolites. *J. Catal* **1996,** *159*, 323.
(67) Sun, Q.; Wang, N.; Bai, R.; Hui, Y.; Zhang, T.; Do, D. A.; Zhang, P.; Song, L.; Miao, S.; Yu, J. Synergetic Effect of Ultrasmall Metal Clusters and Zeolites Promoting Hydrogen Generation. *Adv. Sci.* **2019,** *6*, 1802350.
(68) Mendes, P. S. F.; Mota, F. M.; Silva, J. M.; Ribeiro, M. F.; Daudin, A.; Bouchy, C. A systematic study on mixtures of Pt/zeolite as hydroisomerization catalysts. *Catal. Sci. Technol.* **2017,** *7*, 1095.

(69) Shan, J.; Li, M.; Allard, L. F.; Lee, S.; Flytzani-Stephanopoulos, M. Mild oxidation of methane to methanol or acetic acid on supported isolated rhodium catalysts. *Nature* **2017,** *551*, 605.
(70) Kato, H.; Minami, T.; Kanazawa, T.; Sasaki, Y. Mesopores created by platinum nanoparticles in zeolite crystals. *Angew. Chem. Int. Ed.* **2004,** *43*, 1251.
(71) Besoukhanova, C.; Guidot, J.; Barthomeuf, D.; Breysse, M.; Bernard, J. R. Platinum–zeolite interactions in alkaline L zeolites. Correlations between catalytic activity and platinum state. *J. Chem. Soc. Faraday Trans.* **1981,** *77*, 1595.
(72) Choi, M.; Wu, Z.; Iglesia, E. Mercaptosilane-assisted synthesis of metal clusters within zeolites and catalytic consequences of encapsulation. *J. Am. Chem. Soc.* **2010,** *132*, 9129.
(73) Goel, S.; Wu, Z.; Zones, S. I.; Iglesia, E. Synthesis and catalytic properties of metal clusters encapsulated within small-pore (SOD, GIS, ANA) zeolites. *J. Am. Chem. Soc.* **2012,** *134*, 17688.
(74) Wang, N.; Sun, Q.; Bai, R.; Li, X.; Guo, G.; Yu, J. In Situ Confinement of Ultrasmall Pd Clusters within Nanosized Silicalite-1 Zeolite for Highly Efficient Catalysis of Hydrogen Generation. *J. Am. Chem. Soc.* **2016,** *138*, 7484.
(75) Gao, D.; Zheng, A.; Zhang, X.; Sun, H.; Dai, X.; Yang, Y.; Wang, H.; Qin, Y.; Xu, S.; Duan, A. Mercaptosilane-assisted synthesis of sub-nanosized Pt particles within hierarchically porous ZSM-5/SBA-15 materials and their enhanced hydrogenation properties. *Nanoscale* **2015,** *7*, 10918.
(76) Im, J.; Shin, H.; Jang, H.; Kim, H.; Choi, M. Maximizing the catalytic function of hydrogen spillover in platinum-encapsulated aluminosilicates with controlled nanostructures. *Nat. Commun.* **2014,** *5*, 3370.
(77) Moliner, M.; Gabay, J. E.; Kliewer, C. E.; Carr, R. T.; Guzman, J.; Casty, G. L.; Serna, P.; Corma, A. Reversible Transformation of Pt Nanoparticles into Single Atoms inside High-Silica Chabazite Zeolite. *J. Am. Chem. Soc.* **2016,** *138*, 15743.
(78) Zhang, J.; Wang, L.; Shao, Y.; Wang, Y.; Gates, B. C.; Xiao, F. S. A Pd@Zeolite Catalyst for Nitroarene Hydrogenation with High Product Selectivity by Sterically Controlled Adsorption in the Zeolite Micropores. *Angew. Chem. Int. Ed.* **2017,** *56*, 9747.
(79) Wang, C.; Wang, L.; Zhang, J.; Wang, H.; Lewis, J. P.; Xiao, F. S. Product Selectivity Controlled by Zeolite Crystals in Biomass Hydrogenation over a Palladium Catalyst. *J. Am. Chem. Soc.* **2016,** *138*, 7880.
(80) Zhang, J.; Wang, L.; Zhang, B.; Zhao, H.; Kolb, U.; Zhu, Y.; Liu, L.; Han, Y.; Wang, G.; Wang, C.et al. Sinter-resistant metal nanoparticle catalysts achieved by immobilization within zeolite crystals via seed-directed growth. *Nat. Catal.* **2018,** *1*, 540.
(81) Hirai, H.; Yakura, N. Protecting Polymers in Suspension of Metal Nanoparticles. *Polym. Adv. Technol.* **2001,** *12*, 724.
(82) Cui, T. L.; Ke, W. Y.; Zhang, W. B.; Wang, H. H.; Li, X. H.; Chen, J. S. Encapsulating Palladium Nanoparticles Inside Mesoporous MFI Zeolite Nanocrystals for Shape-Selective Catalysis. *Angew. Chem. Int. Ed.* **2016,** *55*, 9178.
(83) Liu, L.; Zakharov, D. N.; Arenal, R.; Concepcion, P.; Stach, E. A.; Corma, A. Evolution and stabilization of subnanometric metal species in confined space by in situ TEM. *Nat. Commun.* **2018,** *9*, 574.
(84) Zhang, Y.; Kubů, M.; Mazur, M.; Čejka, J. Encapsulation of Pt nanoparticles into IPC-2 and IPC-4 zeolites using the ADOR approach. *Microporous Mesoporous Mater.* **2019,** *279*, 364.
(85) Zhao, Z.; Li, Y.; Feyen, M.; McGuire, R.; Müller, U.; Zhang, W. Pd Nanoparticles Encapsulated in FER Zeolite through a Layer Reassembling Strategy as Shape-selective Hydrogenation Catalyst. *ChemCatChem* **2018,** *10*, 2254.
(86) Tuel, A.; Farrusseng, D. Hollow Zeolite Single Crystals: Synthesis Routes and Functionalization Methods. *Small Methods* **2018,** *2*, 1800197.
(87) Wang, H.; Wang, L.; Xiao, F. S. Metal@Zeolite Hybrid Materials for Catalysis. *ACS. Cent. Sci.* **2020,** *6*, 1685.
(88) Berlier, G.; Crocellà, V.; Signorile, M.; Borfecchia, E.; Bonino, F.; Bordiga, S. *Characterization of Metal Centers in Zeolites for Partial Oxidation Reactions*; Springer, 2018; Vol. 178.

(89) Gao, C.; Lyu, F.; Yin, Y. Encapsulated Metal Nanoparticles for Catalysis. *Chem. Rev.* **2020,** *121*, 834.
(90) Zhang, L.; Zhou, M.; Wang, A.; Zhang, T. Selective Hydrogenation over Supported Metal Catalysts: From Nanoparticles to Single Atoms. *Chem. Rev.* **2020,** *120*, 683.
(91) Su, J.; Chen, J.-S. Synthetic porous materials applied in hydrogenation reactions. *Microporous Mesoporous Mater.* **2017,** *237*, 246.
(92) Liu, L.; Corma, A. Metal Catalysts for Heterogeneous Catalysis: From Single Atoms to Nanoclusters and Nanoparticles. *Chem. Rev.* **2018,** *118*, 4981.
(93) Yang, X. F.; Wang, A.; Qiao, B.; Li, J.; Liu, J.; Zhang, T. Single-atom catalysts: a new frontier in heterogeneous catalysis. *Acc. Chem. Res.* **2013,** *46*, 1740.
(94) Thomas, J. M.; Raja, R.; Lewis, D. W. Single-site heterogeneous catalysts. *Angew. Chem. Int. Ed.* **2005,** *44*, 6456.
(95) MÉRiaudeau, P.; Naccache, C. Dehydrocyclization of Alkanes Over Zeolite-Supported Metal Catalysts: Monofunctional or Bifunctional Route. *Catal. Rev. Sci. Eng.* **1997,** *39*, 5.
(96) Li, Y.; Li, L.; Yu, J. Applications of Zeolites in Sustainable Chemistry. *Chem* **2017,** *3*, 928.
(97) Liang, J.; Liang, Z.; Zou, R.; Zhao, Y. Heterogeneous Catalysis in Zeolites, Mesoporous Silica, and Metal-Organic Frameworks. *Adv. Mater.* **2017,** *29*.
(98) Shi, Y.; Xing, E.; Wu, K.; Wang, J.; Yang, M.; Wu, Y. Recent progress on upgrading of bio-oil to hydrocarbons over metal/zeolite bifunctional catalysts. *Catal. Sci. Technol.* **2017,** *7*, 2385.
(99) Kim, J.; Kim, W.; Seo, Y.; Kim, J.-C.; Ryoo, R. n-Heptane hydroisomerization over Pt/MFI zeolite nanosheets: Effects of zeolite crystal thickness and platinum location. *J. Catal* **2013,** *301*, 187.
(100) Zhang, M.; Chen, Y.; Wang, L.; Zhang, Q.; Tsang, C.-W.; Liang, C. Shape Selectivity in Hydroisomerization of Hexadecane over Pt Supported on 10-Ring Zeolites: ZSM-22, ZSM-23, ZSM-35, and ZSM-48. *Ind. Eng. Chem. Res.* **2016,** *55*, 6069.
(101) Lanzafame, P.; Perathoner, S.; Centi, G.; Heracleous, E.; Iliopoulou, E. F.; Triantafyllidis, K. S.; Lappas, A. A. Effect of the Structure and Mesoporosity in Ni/Zeolite Catalysts for n‐Hexadecane Hydroisomerisation and Hydrocracking. *ChemCatChem* **2017,** *9*, 1632.
(102) Wang, W.; Liu, C.-J.; Wu, W. Bifunctional catalysts for the hydroisomerization of n-alkanes: the effects of metal–acid balance and textural structure. *Catal. Sci. Technol.* **2019,** *9*, 4162.
(103) Robinson, A. M.; Hensley, J. E.; Medlin, J. W. Bifunctional Catalysts for Upgrading of Biomass-Derived Oxygenates: A Review. *ACS Catal.* **2016,** *6*, 5026.
(104) Batalha, N.; Pinard, L.; Pouilloux, Y.; Guisnet, M. Bifunctional Hydrogenating/Acid Catalysis: Quantification of the Intimacy Criterion. *Catal. Lett.* **2013,** *143*, 587.
(105) Guisnet, M. "Ideal" bifunctional catalysis over Pt-acid zeolites. *Catal. Today* **2013,** *218-219*, 123.
(106) Limlamthong, M.; Yip, A. C. K. Recent advances in zeolite-encapsulated metal catalysts: A suitable catalyst design for catalytic biomass conversion. *Bioresour. Technol.* **2020,** *297*, 122488.
(107) Babucci, M.; Guntida, A.; Gates, B. C. Atomically Dispersed Metals on Well-Defined Supports including Zeolites and Metal-Organic Frameworks: Structure, Bonding, Reactivity, and Catalysis. *Chem. Rev.* **2020,** *120*, 11956.
(108) Luo, W.; Cao, W.; Bruijnincx, P. C. A.; Lin, L.; Wang, A.; Zhang, T. Zeolite-supported metal catalysts for selective hydrodeoxygenation of biomass-derived platform molecules. *Green Chem.* **2019,** *21*, 3744.
(109) Ennaert, T.; Feys, S.; Hendrikx, D.; Jacobs, P. A.; Sels, B. F. Reductive splitting of hemicellulose with stable ruthenium-loaded USY zeolites. *Green Chem.* **2016,** *18*, 5295.
(110) Ennaert, T.; Op de Beeck, B.; Vanneste, J.; Smit, A. T.; Huijgen, W. J. J.; Vanhulsel, A.; Jacobs, P. A.; Sels, B. F. The importance of pretreatment and feedstock purity in the reductive splitting of (ligno)cellulose by metal supported USY zeolite. *Green Chem.* **2016,** *18*, 2095.
(111) Chio, C.; Sain, M.; Qin, W. Lignin utilization: A review of lignin depolymerization from various aspects. *Renew. Sust. Energ. Rev.* **2019,** *107*, 232.

(112) Kamimura, N.; Sakamoto, S.; Mitsuda, N.; Masai, E.; Kajita, S. Advances in microbial lignin degradation and its applications. *Curr. Opin. Biotechnol.* **2019,** *56*, 179.
(113) Kumar, A.; Anushree; Kumar, J.; Bhaskar, T. Utilization of lignin: A sustainable and eco-friendly approach. *J. Energy Inst.* **2020,** *93*, 235.
(114) Li, X.; Chen, G.; Liu, C.; Ma, W.; Yan, B.; Zhang, J. Hydrodeoxygenation of lignin-derived bio-oil using molecular sieves supported metal catalysts: A critical review. *Renew. Sust. Energ. Rev.* **2017,** *71*, 296.
(115) Guadix-Montero, S.; Sankar, M. Review on Catalytic Cleavage of C–C Inter-unit Linkages in Lignin Model Compounds: Towards Lignin Depolymerisation. *Top Catal.* **2018,** *61*, 183.
(116) Wong, S. S.; Shu, R.; Zhang, J.; Liu, H.; Yan, N. Downstream processing of lignin derived feedstock into end products. *Chem. Soc. Rev.* **2020,** *49*, 5510.
(117) Kasakov, S.; Shi, H.; Camaioni, D. M.; Zhao, C.; Baráth, E.; Jentys, A.; Lercher, J. A. Reductive deconstruction of organosolv lignin catalyzed by zeolite supported nickel nanoparticles. *Green Chem.* **2015,** *17*, 5079.
(118) Wang, H.; Male, J.; Wang, Y. Recent Advances in Hydrotreating of Pyrolysis Bio-Oil and Its Oxygen-Containing Model Compounds. *ACS Catal.* **2013,** *3*, 1047.
(119) Hong, D. Y.; Miller, S. J.; Agrawal, P. K.; Jones, C. W. Hydrodeoxygenation and coupling of aqueous phenolics over bifunctional zeolite-supported metal catalysts. *Chem. Commun.* **2010,** *46*, 1038.
(120) Sasaki, T.; Zhong, C.; Tada, M.; Iwasawa, Y. Immobilized metal ion-containing ionic liquids: preparation, structure and catalytic performance in Kharasch addition reaction. *Chem. Commun.* **2005**, 2506.
(121) Dou, Q.; Liu, L.; Yang, B.; Lang, J.; Yan, X. Silica-grafted ionic liquids for revealing the respective charging behaviors of cations and anions in supercapacitors. *Nat. Commun.* **2017,** *8*, 2188.
(122) Corma, A.; Corell, C.; Pérez-Pariente, J. Synthesis and characterization of the MCM-22 zeolite. *Zeolites* **1995,** *15*, 2.
(123) Pastoriza-Santos, I.; Liz-Marzán, L. M. Formation and Stabilization of Silver Nanoparticles through Reduction byN,N-Dimethylformamide. *Langmuir* **1999,** *15*, 948.
(124) Pastoriza-Santos, I.; Liz-Marzán, L. M. N,N-Dimethylformamide as a Reaction Medium for Metal Nanoparticle Synthesis. *Adv. Funct. Mater.* **2009,** *19*, 679.
(125) Shvets, O. V.; Shamzhy, M. V.; Yaremov, P. S.; Musilová, Z.; Procházková, D.; Čejka, J. i. Isomorphous Introduction of Boron in Germanosilicate Zeolites with UTL Topology. *Chem. Mater.* **2011,** *23*, 2573.
(126) Sun, Q.; Wang, N.; Zhang, T.; Bai, R.; Mayoral, A.; Zhang, P.; Zhang, Q.; Terasaki, O.; Yu, J. Zeolite-Encaged Single-Atom Rhodium Catalysts: Highly-Efficient Hydrogen Generation and Shape-Selective Tandem Hydrogenation of Nitroarenes. *Angew. Chem. Int. Ed.* **2019,** *58*, 18570.
(127) Xia, B. Y.; Wu, H. B.; Chen, J. S.; Wang, Z.; Wang, X.; Lou, X. W. Formation of Pt-TiO2-rGO 3-phase junctions with significantly enhanced electro-activity for methanol oxidation. *Phys. Chem. Chem. Phys.* **2012,** *14*, 473.
(128) Sun, L.; Zhang, S.; Bao, W.; He, W. Catalytic properties of Pd nanoparticles supported on Cu2O microspheres for hydrogen peroxide electroreduction. *RSC Adv.* **2015,** *5*, 53320.
(129) Yokoi, T.; Mochizuki, H.; Namba, S.; Kondo, J. N.; Tatsumi, T. Control of the Al Distribution in the Framework of ZSM-5 Zeolite and Its Evaluation by Solid-State NMR Technique and Catalytic Properties. *J. Phys. Chem. C* **2015,** *119*, 15303.
(130) Jacobsen, C. J. H.; Madsen, C.; Janssens, T. V. W.; Jakobsen, H. J.; Skibsted, J. Zeolites by confined space synthesis – characterization of the acid sites in nanosized ZSM-5 by ammonia desorption and 27Al/29Si-MAS NMR spectroscopy. *Microporous Mesoporous Mater.* **2000,** *39*, 393.
(131) Klinowski, J.; Carpenter, T. A.; Gladden, L. F. High-resolution solid-state n.m.r. studies of temperature-induced phase transitions in silicalite (zeolite ZSM—5). *Zeolites* **1987,** *7*, 73.

(132) Sazama, P.; Wichterlova, B.; Dedecek, J.; Tvaruzkova, Z.; Musilova, Z.; Palumbo, L.; Sklenak, S.; Gonsiorova, O. FTIR and 27Al MAS NMR analysis of the effect of framework Al- and Si-defects in micro- and micro-mesoporous H-ZSM-5 on conversion of methanol to hydrocarbons. *Microporous Mesoporous Mater.* **2011,** *143*, 87.
(133) Thommes, M.; Kaneko, K.; Neimark, A. V.; Olivier, J. P.; Rodriguez-Reinoso, F.; Rouquerol, J.; Sing, K. S. W. Physisorption of gases, with special reference to the evaluation of surface area and pore size distribution (IUPAC Technical Report). *Pure Appl. Chem.* **2015,** *87*, 1051.
(134) Thommes, M. Physical Adsorption Characterization of Nanoporous Materials. *Chem. Ing. Tech.* **2010,** *82*, 1059.
(135) Kokotailo, G. T.; Lawton, S. L.; Olson, D. H.; Meier, W. M. Structure of synthetic zeolite ZSM-5. *Nature* **1978,** *272*, 437.
(136) Olson, D. H.; Kokotailo, G. T.; Lawton, S. L.; Meier, W. M. Crystal structure and structure-related properties of ZSM-5. *J. Phys. Chem. A* **1981,** *85*, 2238.
(137) Lockwood, D. J. *Noble Metal Nanoparticles*; Springer 2017.
(138) Camblor, M. A.; Corma, A.; Díaz-Cabañas, M.-J.; Baerlocher, C. Synthesis and Structural Characterization of MWW Type Zeolite ITQ-1, the Pure Silica Analog of MCM-22 and SSZ-25. *J. Phys. Chem. B* **1998,** *102*, 44.
(139) Roth, W. J.; Dorset, D. L.; Kennedy, G. J. Discovery of new MWW family zeolite EMM-10: Identification of EMM-10P as the missing MWW precursor with disordered layers. *Microporous Mesoporous Mater.* **2011,** *142*, 168.
(140) Roth, W. J.; Chlubná, P.; Kubů, M.; Vitvarová, D. Swelling of MCM-56 and MCM-22P with a new medium — surfactant–tetramethylammonium hydroxide mixtures. *Catal. Today* **2013,** *204*, 8.
(141) Polozij, M.; Thang, H. V.; Rubes, M.; Eliasova, P.; Cejka, J.; Nachtigall, P. Theoretical investigation of layered zeolites with MWW topology: MCM-22P vs. MCM-56. *Dalton Trans.* **2014,** *43*, 10443.
(142) Xing, E.; Shi, Y.; Xie, W.; Zhang, F.; Mu, X.; Shu, X. Synthesis, characterization and application of MCM-22 zeolites via a conventional HMI route and temperature-controlled phase transfer hydrothermal synthesis. *RSC Adv.* **2015,** *5*, 8514.
(143) Roth, W. J.; Gil, B.; Makowski, W.; Sławek, A.; Korzeniowska, A.; Grzybek, J.; Siwek, M.; Michorczyk, P. Framework-substituted cerium MCM-22 zeolite and its interlayer expanded derivative MWW-IEZ. *Catal. Sci. Technol.* **2016,** *6*, 2742.
(144) Liu, L.; Arenal, R.; Meira, D. M.; Corma, A. Generation of gold nanoclusters encapsulated in an MCM-22 zeolite for the aerobic oxidation of cyclohexane. *Chem. Commun.* **2019,** *55*, 1607.
(145) Roth, W. J.; Gil, B.; Marszalek, B. Comprehensive system integrating 3D and 2D zeolite structures with recent new types of layered geometries. *Catal. Today* **2014,** *227*, 9.
(146) Schwanke, A. J.; Díaz, U.; Corma, A.; Pergher, S. Recyclable swelling solutions for friendly preparation of pillared MWW-type zeolites. *Microporous Mesoporous Mater.* **2017,** *253*, 91.
(147) Knözinger, H.; Huber, S. IR spectroscopy of small and weakly interacting molecular probes for acidic and basic zeolites. *J. Chem. Soc. Faraday Trans.* **1998,** *94*, 2047.
(148) Zecchina, A.; Bordiga, S.; Spoto, G.; Scarano, D.; Petrini, G.; Leofanti, G.; Padovan, M.; Areàn, C. O. Low-temperature Fourier-transform infrared investigation of the interaction of CO with nanosized ZSM5 and silicalite. *J. Chem. Soc. Faraday Trans.* **1992,** *88*, 2959.
(149) Holm, M. S.; Svelle, S.; Joensen, F.; Beato, P.; Christensen, C. H.; Bordiga, S.; Bjørgen, M. Assessing the acid properties of desilicated ZSM-5 by FTIR using CO and 2,4,6-trimethylpyridine (collidine) as molecular probes. *Appl Catal. A* **2009,** *356*, 23.
(150) Hadjiivanov, K. *Identification and Characterization of Surface Hydroxyl Groups by Infrared Spectroscopy*; Elsevier, 2014; Vol. 57.
(151) Hadjiivanov, K. I.; Vayssilov, G. N. *Characterization of oxide surfaces and zeolites by carbon monoxide as an IR probe molecule*; Elsevier, 2002; Vol. 47.
(152) Sorribes, I.; Liu, L.; Corma, A. Nanolayered Co–Mo–S Catalysts for the Chemoselective Hydrogenation of Nitroarenes. *ACS Catal.* **2017,** *7*, 2698.

(153) Gao, R.; Pan, L.; Wang, H.; Zhang, X.; Wang, L.; Zou, J.-J. Ultradispersed Nickel Phosphide on Phosphorus-Doped Carbon with Tailored d-Band Center for Efficient and Chemoselective Hydrogenation of Nitroarenes. *ACS Catal.* **2018,** *8*, 8420.
(154) Lei, L.; Wu, Z.; Liu, H.; Qin, Z.; Chen, C.; Luo, L.; Wang, G.; Fan, W.; Wang, J. A facile method for the synthesis of graphene-like 2D metal oxides and their excellent catalytic application in the hydrogenation of nitroarenes. *J. Mater. Chem. A* **2018,** *6*, 9948.
(155) She, W.; Qi, T.; Cui, M.; Yan, P.; Ng, S. W.; Li, W.; Li, G. High Catalytic Performance of a CeO2-Supported Ni Catalyst for Hydrogenation of Nitroarenes, Fabricated via Coordination-Assisted Strategy. *ACS Appl. Mater. Interfaces* **2018,** *10*, 14698.
(156) Sun, X.; Olivos-Suarez, A. I.; Osadchii, D.; Romero, M. J. V.; Kapteijn, F.; Gascon, J. Single cobalt sites in mesoporous N-doped carbon matrix for selective catalytic hydrogenation of nitroarenes. *J. Catal* **2018,** *357*, 20.
(157) Brunauer, S.; Emmett, P. H.; Teller, E. Adsorption of Gases in Multimolecular Layers. *J. Am. Chem. Soc.* **1938,** *60*, 309.
(158) Sing, K. S. W. Reporting physisorption data for gas/solid systems with special reference to the determination of surface area and porosity (Provisional). *Pure Appl. Chem.* **1982,** *54*, 2201.

7. Enclosures

1. **Yuyan Zhang**, Ang Li, Mehran Sajad, Katarína Fulajtárová, Michal Mazur, Martin Kubů, Mariya Shamzhy, Milan Hronec, Roman Bulánek, and Jiří Čejka *. Imidazolium-type ionic liquid-assisted formation of the MFI zeolite loaded with metal nanoparticles for hydrogenation reactions*, Chem. Eng. J.*, **2021**, 412, 128599.

2. **Yuyan Zhang**, Martin Kubů *, Michal Mazur, Jiří Čejka. Synthesis of Pt-MWW with Controllable Nanoparticle Size, *Catal. Today*, **2019**, 324,135.

3. **Yuyan Zhang**, Katarína Fulajtárová, Martin Kubů, Michal Mazur *, Mariya Shamzhy, Milan Hronec, and Jiří Čejka *. Controlling dispersion and accessibility of Pd nanoparticles via 2D-to-3D zeolite transformation for shape-selective catalysis: Pd@MWW case, *Materials Today Nano*, **2019**, 8, 100056.

4. **Yuyan Zhang**, Martin Kubů *, Michal Mazur, Jiří Čejka. Encapsulation of Pt nanoparticles into IPC-2 and IPC-4 zeolites using the ADOR approach, *Microporous Mesoporous Mater*., **2019**, 279, 364.

5. **Yuyan Zhang**, Katarína Fulajtárová, Martin Kubů, Michal Mazur *, Milan Hronec, Jiří Čejka. Electronic/steric effects in hydrogenation of nitroarenes over the heterogeneous Pd@BEA and Pd@MWW catalysts, *Catal. Today*, **2020**, 345, 39.